Comparative dosimetric evaluation of voxel and mesh ICRP reference phantoms in a medical linear accelerator environment

by

Ashleigh K. Mauler

B.S., Kansas State University, 2025

A THESIS

submitted in partial fulfillment of the
requirements for the degree

MASTER OF SCIENCE

Department of Mechanical and Nuclear Engineering
Carl R. Ice College of Engineering

KANSAS STATE UNIVERSITY
Manhattan, Kansas

2026

Approved by:

Major Professor
Amir A. Bahadori

Copyright

Abstract

To more accurately represent complex anatomical structures, adult mesh computational phantoms were introduced by the ICRP in Publication 145 in 2020. These phantoms were derived from the voxel computational phantoms presented in Publication 110 in 2009. The new mesh phantoms are composed of tetrahedrons, allowing smooth surfaces and fine structures to be represented and addressing the limitations of voxels, which may result in inaccurate organ dose estimates in certain exposure scenarios. This study compares simulated doses to various organs caused by radiation from a medical linear accelerator (LINAC). A Monte Carlo radiation transport code, Particle and Heavy Ion Transport code System (PHITS), was employed for these simulations. Discrepancies in organ doses were observed between the ICRP phantoms, resulting from the mesh model's more detailed anatomical structures and the inclusion of smaller organs.

After establishing that differences exist between the ICRP mesh and voxel phantoms when simulating doses from a medical LINAC, experimental validation utilizing thermoluminescent dosimeters (TLDs) was pursued. TLDs are widely used in personal dosimetry due to their sensitivity and reliability. For these experiments, TLDs were strategically placed throughout an anthropomorphic torso phantom (ATP) to measure the absorbed dose at various anatomical locations. To enable direct comparison between experimental and simulated results, the ATP was CT scanned, segmented, and implemented into PHITS as well as the Varian Eclipse anisotropic analytical algorithm (AAA) calculation. By comparing the experimental dose measurements from the TLDs to the simulated doses within the segmented ATP, the accuracy of the simulations may be assessed. The results indicated that the Monte Carlo PHITS simulation provided greater accuracy than the AAA model. Because of this, the PHITS simulations are used as a reference to evaluate how well the ICRP voxel and mesh phantoms replicate realistic dose distributions, ultimately determining that the added

complexity of the mesh phantoms is justified for this exposure scenario. While target doses remained within 3% among the ATP, male voxel, and male mesh phantoms, the female mesh phantom showed a dose discrepancy of approximately 10%. Another significant point of divergence was observed in the breast tissue, where anatomical differences between the sexes resulted in a decreased mean organ dose for the female mesh relative to the male mesh. Ultimately, the mesh phantoms provided critical insights into organs at risk (OARs) and sensitive tissue layers that both the voxel and ATP models failed to capture.

Table of Contents

List of Figures

List of Tables

Acknowledgments

There are many people who have supported me throughout the completion of this thesis, and while this list is not exhaustive, I want to recognize those who were instrumental to this journey.

Foremost, I would like to express my deepest gratitude to my major professor, Dr. Amir A. Bahadori. His constant encouragement to persevere through challenges and his guidance have consistently led me in the right direction. I also want to thank my committee members, Dr. Jeremy Roberts and Dr. Chieko Azuma, for their invaluable support and for being available whenever I needed guidance.

Much of this work would not have been possible without the support of the Kansas State University College of Veterinary Medicine, specifically the Radiology Department. I am particularly grateful to Kodi Ginavan, whose collaboration and assistance were instrumental to the final completion of this project.

I also want to thank the individuals I share my home with in Ward Hall. Showing up each day is a genuine pleasure because of the people I am able to collaborate and grow with. Finally, to my friends and family: thank you for always encouraging me to think outside the box. You are the reason I am in the position I am today, and I am forever grateful for your love and support.

This work was supported by U.S. Nuclear Regulatory Commission (NRC) Grant No. 31310021M0030. Computational support was provided by Beocat, the high-performance computing system at Kansas State University. Any opinions, findings, and conclusions or recommendations expressed in this material are those of the author and do not necessarily reflect the views of the sponsoring organizations.

Chapter 1

Introduction

1.1 Evolution of Computational Phantoms

The use of computational phantoms, which are mathematical representations of the human body, is a central practice in modern human dosimetry. These models are essential for calculating organ-specific energy deposition from radiation, which in turn informs our understanding of biological effects and guides the establishment of safety regulations. This approach originated in the 1960s at Oak Ridge National Laboratory, where the first stylized phantoms were created by the committee on Medical Internal Radiation Dose (MIRD) of the Society of Nuclear Medicine.[1] By representing the human anatomy with simple 2D and 3D shapes like spheres and cylinders, the MIRD phantoms pioneered a method that would evolve significantly over the next six decades, laying the groundwork for all future computational dosimetry. However, the primary limitation of these early models was their lack of anatomical accuracy, a challenge that directly motivated the development of more sophisticated phantoms.

In 1974, the International Commission on Radiological Protection (ICRP) established a task group to develop the "Reference Man," a standardized model created to ensure consistency in radiation dose estimations.[2] This model provides a common baseline for scientists, eliminating many contrasting assumptions and reducing discrepancies between different re-

search efforts. Although real individuals vary significantly in biology, the Reference Man offers a framework for dose assessment. The model specifies numerous parameters such as the mass, dimensions, and elemental composition of all major organs and tissues. The comprehensive findings of the task group were compiled and published in ICRP Publication 23 in 1975.[2] The reference anatomical and physiological values were updated in 2002 with ICRP Publication 89 which expanded the biological data including age, gender, race, and other factors.[3]

The 2007 release of ICRP Publication 103, "The 2007 Recommendations of the International Commission on Radiological Protection," called for the development of more realistic computational models based on computed tomography (CT) or magnetic resonance imaging (MRI) scans to ensure dose estimates would better reflect true human anatomy.[4] In response to this recommendation, in 2009 the ICRP released Publication 110, "Adult Reference Computational Phantoms." This publication synthesized data from several foundational ICRP and ICRU documents to create a single, harmonized computational phantom.[5] The process of incorporating data from these past publications is detailed in Figure 1.1. For instance, ICRP Publication 89 provided the anatomical framework, including reference values for body height, total body mass, and the specific masses of nearly every organ. ICRP Publication 103 defined the key radiological protection principles and identified the radiosensitive tissues requiring segmentation, assigning them tissue weighting factors (w_T). Detailed data on the composition and distribution of bone and active marrow was drawn from ICRP Publication 70[6], while ICRU Report 46[7] supplied the essential physical data, such as tissue densities and elemental compositions, required for accurately simulating radiation interactions within the body.

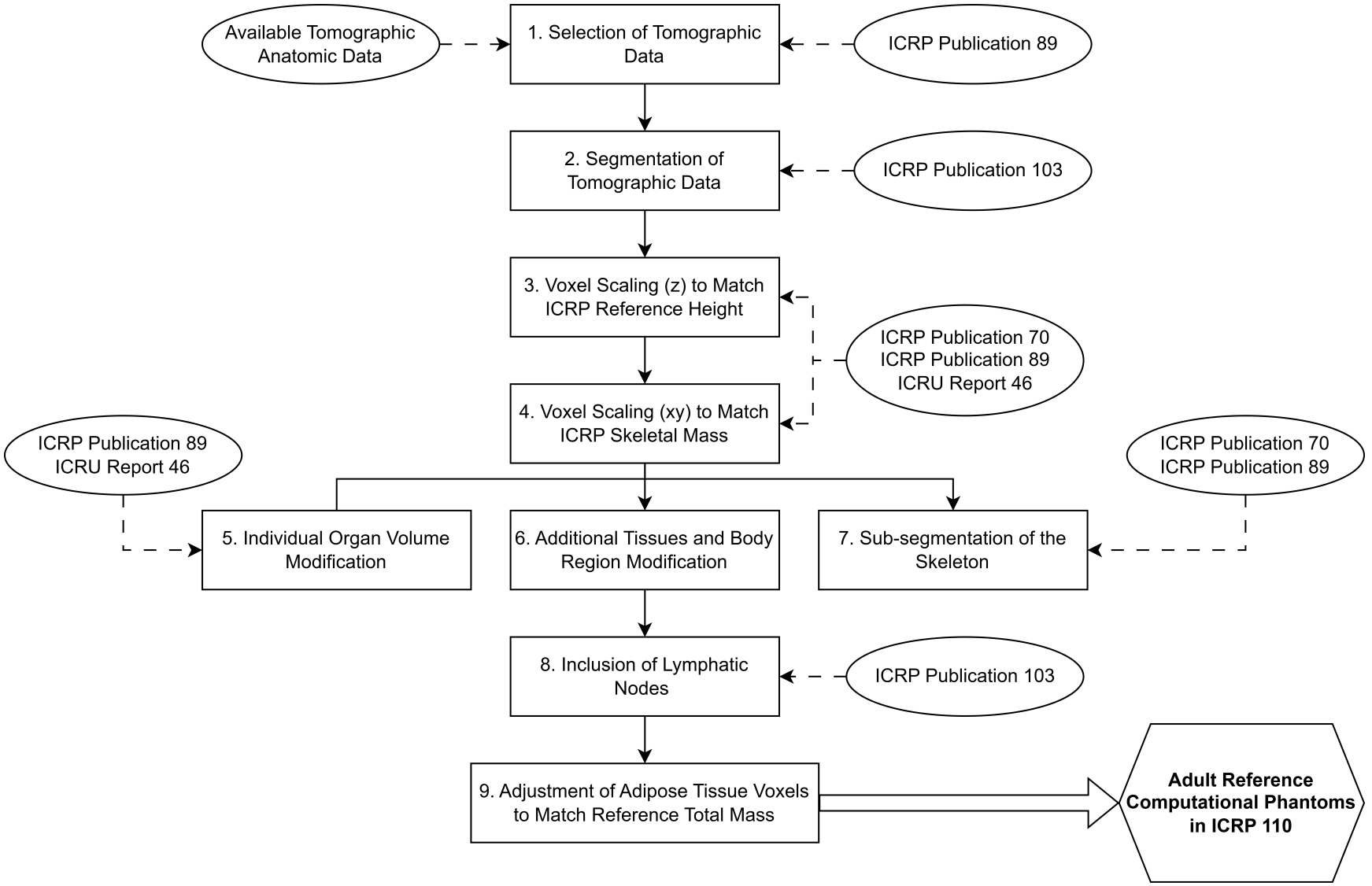

Figure 1.1: Schematic for constructing voxel computational phantoms representing the adult Reference Male and Female.[5]

ICRP Publication 110[5], developed in conjunction with the International Commission on Radiation Units and Measurements (ICRU), established a new benchmark for radiation protection dosimetry. The publication introduced a set of highly detailed, anatomically realistic human phantoms, which the ICRP uses to calculate its reference dose coefficients. This foundational work directly influences international and national regulatory bodies. The International Atomic Energy Agency (IAEA), for example, bases its safety standards on ICRP recommendations and cites numerous studies utilizing Publication 110[8]. Similarly, the United States Nuclear Regulatory Commission (US NRC) had initiated plans to update its federal regulations (10 CFR Part 20) to align with the ICRP Publication 103 framework, a methodology implemented using the advanced computational phantoms detailed in ICRP Publication 110[9]. Upon its release, ICRP Publication 110 quickly became the new standard for accurately simulating radiation dose in the human body.

While ICRP Publication 110 became widely cited and utilized among the scientific community, it still had limitations. ICRP Publication 110 phantoms are made up of a three-dimensional (3D) grid of rectangular parallelepiped volume elements, or voxels. The phantom would resemble building blocks stacked on top of each other to build a human person. This leads to a major disadvantage within the voxel phantoms: the stair step effect. Human anatomy has curved and fine structures which are now represented by blocky voxel edges, causing the resolution and visibility of the organs to be poor. Because of the lack of resolution, small and complex organs could not be modeled within the phantom. Yet, even with these limitations, use of the voxel phantom was considered to be the best practice at that time for human dosimetry.

To overcome the limitations of voxel-based models and provide a single, full-scale anatomical computational phantom to serve as a unified ICRP standard, avoiding the need for various external models, the ICRP formed Task Group 103. This group worked to develop the mesh-type reference computational phantoms (MRCPs), and in 2020, their work culminated in the release of ICRP Publication 145, "Adult Mesh-Type Computational Phantoms."[10] These advanced phantoms were derived from the ICRP Publication 110 voxel models, using a tetrahedral mesh to represent the complex geometry of human anatomy. The procedure

begins with a voxel-based organ model, characterized by a "stair-step" appearance, which is converted into a primitive polygonal-mesh (PM) model. To refine the anatomical fidelity, the number of facets is first increased to capture detail and then decreased to optimize the model, while simultaneously increasing the smoothness of the boundary. This process eliminates the blocky artifacts inherent to voxel grids, resulting in a smoother, more anatomically faithful representation. The final step involves the adjustment of the organ mass to align with specific updated ICRP reference values, ensuring the model meets standardized physiological parameters for radiation dosimetry. The mesh-based approach provides several key advantages over its voxel-based predecessor, including a continuous and more accurate skin surface, more realistic organ dimensions, the incorporation of blood mass content, and the inclusion of anatomical parts that previously could not be modeled due to the improved ability to model small and intricate structures.

The development of mesh-type computational phantoms marked a significant advancement in radiation dosimetry. By eliminating the "stair-step" artifact common to voxel grids, mesh phantoms provide smoother, more anatomically faithful representations of human organs and tissues. The ICRP first introduced this technology with the adult models in Publication 145[10] and has since expanded its library to include a series of pediatric phantoms (ICRP Publication 156[11]), with a pregnant female phantom planned for future release. Despite the large number of models available, this research will focus specifically on the ICRP Publication 110 (voxel) and ICRP Publication 145 (mesh) adult male computational phantoms.

The selection of the adult male computational phantoms from ICRP Publications 110 and 145 for this research is based on their international standing, their relevance to clinical cancer treatments, and the significant technological shift from voxel-based to mesh-based modeling. The ICRP is an independent, international organization that advances the science of radiological protection by providing global recommendations and guidance. Major governing bodies, such as the U.S. Nuclear Regulatory Commission (NRC) and the Department of Energy (DOE), rely on ICRP documentation to establish national safety regulations. Furthermore, because these phantoms provide high-fidelity representations of human anatomy,

they are of critical interest for optimizing radiation oncology and cancer treatments. Finally, the recent shift to mesh-type phantoms directly affects the Dose Coefficients published by the ICRP, which are the foundational values used by regulatory bodies to assess and limit radiation exposure.

1.2 Dose Calculation Software

The Monte Carlo method is a computational algorithm that transforms a complex problem into a probabilistic experiment, using repeated random sampling to converge on a numerical result. This method is utilized within radiation transport to model the random interactions of particles within matter. The main components of Monte Carlo codes include the physics models, the cross section data as functions of energy and material, and the geometry. A multitude of computational monte carlo codes have been created to simulate radiation transport, this includes MCNP[12], GEANT4[13], or PHITS[14]. Throughout this research, the Monte Carlo code Particle and Heavy Ion Transport code System (PHITS) is used to simulate radiation transport. PHITS utilizes several nuclear reaction models and nuclear data libraries such as Japanese Evaluated Nuclear Data Library (JENDL) which is maintained by the Japanese Atomic Energy Agency.[14]

While Monte Carlo codes like PHITS provide highly accurate dosimetric simulations, they are computationally intensive due to the nature of tracking millions of particles across a complex geometry. To achieve high statistical accuracy in a shortened time frame, this research utilized Beocat,[15] the high performance computing (HPC) system at Kansas State University. Beocat is a heterogeneous system comprised of five different classes of computing nodes, each with varying properties such as processor architecture, core counts, and random access memory (RAM). This diversity allows for flexible resource allocation, ensuring that computationally demanding tasks have access to high-performance hardware. For this study, simulations were primarily executed on the Wizard and Dwarves node classes to maximize the efficiency of the OpenMP parallelization. The Wizard nodes are equipped with high-performance Intel Xeon Gold 6130 processors, offering between 32 and 64 cores per node and

substantial memory capacities ranging from 96 GB up to 1.5 TB. Complementing these, the Dwarves nodes utilize Intel Xeon E5-2683 v4 processors, consistently providing 32 cores per node with up to 512 GB of RAM.[15] Unlike distributed-memory models (MPI)[16] that span multiple nodes, the OpenMP[17] model employed here utilizes a shared-memory architecture. By dispatching a single simulation instance to one of these high-density nodes, the code could spread across roughly 32 concurrent threads—keeping all memory access local to the node. This approach eliminated internode latency and drastically minimized the wall-clock time required for convergence.[18]

Another key optimization process in Monte Carlo simulations is the use of variance reduction techniques, which reduce the number of particles required for simulation while maintaining low statistical uncertainty and reducing total computation time. PHITS can accommodate a technique known as weight windows[19], which assigns a weight range, defined by a lower bound (W_L) and an upper bound (W_U), to specific cells and energy groups. Particles are managed based on how their statistical weight compares to these bounds; if a particle's weight is within the window, it is transported normally; if it exceeds W_U, the particle is split into multiple particles with reduced weights to increase sampling density; and if it falls below W_L, it undergoes "Russian roulette" to determine if it survives with an increased weight or is terminated. By controlling the statistical weight in this manner, the simulation remains balanced and efficient across all regions. To simplify this setup, PHITS includes a Weight Window Generator (WWG) that automatically calculates optimized window settings for a user-defined geometry. The ultimate goal of the WWG is to distribute the particle fluence as uniformly as possible across all defined regions, replacing steep uncertainty gradients with a more uniform statistical uncertainty.

Monte Carlo (MC) codes are considered the gold standard for radiation transport simulation in health physics, spanning applications from cosmic radiation[20] exposure to clinical medical physics[21]. However, in the realm of medical radiotherapy, alternative dose calculation models are frequently employed to satisfy both the rigorous accuracy requirements and the practical time constraints of clinical workflows. Within the Varian Eclipse Treatment Planning System, dose distributions are calculated based on a selected algorithm such as the

Anisotropic Analytical Algorithm (AAA)[22] or the Acuros XB (AXB)[23] models.

The AAA is a 3D convolution-superposition algorithm that divides the incident beam into small beamlets and utilizes pre-calculated dose kernels derived from radiation transport in water. To account for tissue heterogeneity, the algorithm applies a "radiological scaling" method to warp these water-equivalent kernels based on electron densities derived from CT Hounsfield Units (HU)[24]. While efficient, this approach is an approximation that often fails to account for dramatic changes in particle behavior as photons and electrons enter low-density media. This leads to a systematic physics failure known as Lateral Electronic Disequilibrium, where the AAA fails to accurately model complex lateral scatter. Specifically, secondary electrons that should scatter back into high-density regions, such as a gross tumor volume (GTV), are miscalculated as the AAA does not track individual particle paths, but rather scales a pre-defined kernel based on local density. This limitation often fails to capture local dose build-up, producing a calculated dose that is lower than the dose physically delivered to the target[25].

The second model, AXB, utilizes a Linear Boltzmann Transport Equation (LBTE) solver to determine dose to organs of interest and optimize patient treatment plans[26]. Unlike the analytical approximations of AAA, the LBTE is a deterministic approach that solves for the angular and energy-dependent flow of both photons and the secondary electrons they set in motion across each voxel. This allows Acuros XB to explicitly model complex physical interactions, including Compton scattering, the photoelectric effect, and pair production, even in challenging geometries with high-density gradients. This makes it particularly effective at interfaces between the lungs and soft tissue or surrounding bony structures. While computationally intensive, the LBTE process provides a near-Monte Carlo accurate alternative for clinical dose calculation. Due to the specific availability of the AAA model at Kansas State, it was utilized as the primary clinical dose calculation engine for this research instead of the AXB algorithm.

Outside of the clinical setting, Monte Carlo codes have been utilized with computational human phantoms to determine organ dose. Phantoms like the mesh and voxel phantoms from the ICRP have been used in a multitude of research, especially within the ICRP. For

example, ICRP publications provide dose or conversion coefficients that have been calculated using the ICRP Publication 110 phantom.[27;28] However, a Monte Carlo simulation is only as accurate as the geometry that is employed. Therefore, it is imperative that phantoms provide anatomical accuracy so the data calculated utilizing the phantoms are correct.

1.3 Radiotherapy

Radiotherapy, or radiation therapy, is a type of cancer treatment that delivers ionizing radiation to kill cancerous cells within the patient. The goal is to deliver a therapeutic dose to a target while minimizing dose to healthy organs surrounding the target. While there are multiple types of radiotherapy, external beam photon therapy is addressed in this research. External beam photon therapy was selected for this study not only because external beam therapy is the primary treatment for lung cancer, but also due to the accessibility of the machine for experimental validation. Photon beam therapy specifically can target tumors deep within the body with little scatter outside the intended area.[29] This treatment is done using a medical linear accelerator (LINAC), which generates high-energy x-rays or electrons that match a tumor's shape using collimation. It destroys cancer cells while preserving the healthy tissue around it. The radiation therapy process involves an extensive treatment planning process that aims to optimize the dose toward the intended target using the models described in section 1.2. The treatment planning process used in this thesis was three-dimensional conformal radiation therapy (3-D CRT), where the radiation treatment is dependent on 3D anatomical data that have been acquired from a computed tomography (CT) image. The treatment planning process used in this research will be discussed extensively in section 2.2.2, but the basic outline includes taking a CT of the phantom, segmentation of the CT image (defining the organs at risk (OARs) and the gross tumor volume (GTV)) and optimizing various components that affect the dose to the GTV.

The principles of radiobiology, the study of how ionizing radiation affects living organisms, are fundamental in radiotherapy. The strategy for killing cancerous cells during radiotherapy is guided by the four R's of radiobiology: repair, reassortment or redistribution, reoxygena-

tion, and repopulation. When radiation is delivered to a cell, the primary biological effect is damage to its deoxyribonucleic acid (DNA). Following this damage, cells attempt to repair sublethal damage. The next principle, reassortment, relates to the cell cycle. Cells have fluctuating sensitivity to radiation; they are most vulnerable in the M and G2 phases and most resistant in the late S phase. The time between radiation doses allows surviving resistant cells to move, or reassort, into more sensitive phases, increasing the effectiveness of the next treatment. Concurrently, reoxygenation occurs, which is a key focus in radiotherapy due to the "oxygen effect." This effect, highly prevalent with low linear energy transfer (LET) radiation like X-rays, makes cells more radiosensitive in the presence of oxygen. Oxygen reacts with radiation-induced free radicals to form peroxides that make DNA damage permanent. Since many tumors have hypoxic (low-oxygen) and thus radioresistant regions, killing the outer oxygenated cells allows oxygen to reach these areas, making them more vulnerable to subsequent doses. Finally, repopulation refers to the regrowth of cells between treatment fractions. The ultimate goal of fractionated radiotherapy is to leverage these processes to optimize the killing of cancerous cells while sparing healthy ones. By dividing the total dose into smaller fractions over several days or weeks, normal tissue is spared due to its capacity for repair and repopulation. At the same time, damage to the tumor is enhanced through the processes of reoxygenation and reassortment of cancer cells into more sensitive states.[30]

While this fractionation strategy is optimized to spare healthy tissues near the target, the protection is not absolute for the entire body. There is a growing concern that low-dose radiation exposure outside the primary treatment volume can lead to the induction of secondary cancers in patients and lymphopenia, which may affect the therapeutic outcome.[31;32] This out-of-field dose, resulting from scatter and leakage radiation, necessitates accurate quantification across the whole body, justifying the use of anatomically realistic, whole-body computational phantoms combined with detailed accelerator models. Previous phantom-based LINAC studies, often utilizing the ICRP Publication 110 reference phantoms, have been conducted to calculate these non-target organ doses for various treatments, such as radiotherapy for prostate and cervical cancer. For instance, one study found that using the realistic anatomy of the ICRP Publication 110 phantom resulted in dose calculation dif-

ferences of over 200% for some organs compared to older, simplified phantoms.[33] However, the voxel-based geometry of the ICRP Publication 110 phantoms presented limitations in accurately representing small or thin tissues, a shortcoming that led to the development of the more advanced ICRP 145 mesh-type phantoms.

Comparative analyses between ICRP Publication 110 and both computational and physical phantoms are well-established in the literature, however, investigations involving ICRP Publication 145 remain limited. Current research has primarily focused on validating these newer mesh models against previous computational standards; for example, studies have concluded that ICRP Publication 145 phantoms reproduce the dose conversion coefficients of older voxel-based models within a 10% margin.[34] However, these validation scenarios often utilize environmental or simplified point-source geometries rather than the complex delivery of a medical radiotherapy setting. Consequently, the direct comparison of ICRP Publication 145 phantoms with experimental data in a clinical context is an emerging area of research. This study bridges that gap by providing an experimental validation of ICRP Publication 145 within the high-precision of a radiotherapy beam.

1.4 Thermoluminescent Dosimetry

The most commonly used personnel dose monitoring system are thermoluminescent dosimeters (TLDs). TLDs are a type of passive radiation detection device that measures the dose from exciting radiation and stores that information until heated. Different thermoluminescent materials such as Lithium Fluoride (LiF) or Calcium Fluoride (CaF_2) are used as dosimeters; for this research, LiF was utilized because of its greater tissue equivalence as opposed to CaF_2. Among LiF TLDs, different dopants can be used to change the properties of the dosimeter. For example, Magnesium, Copper, and Phosphorus are dopants used to create TLD-100H, which is used as the experimental dosimeter in this research. The properties of the material and dopants can change factors such as the linear range, the range that the dose can be accurately measured by the TLD; fading time, the time period the dosimeters lose their ability to accurately measure the dose, due to temperature or light

exposure causing trapped electrons to release prematurely; or sensitivity of the dosimeter.

The operational theory of TLDs (shown in Figure 1.2) is as follows: ionizing radiation excites electrons from the valence band (E_v) to the conduction band (E_c), leaving corresponding holes behind. As these electrons diffuse through the crystal lattice, they may either undergo recombination or become sequestered in metastable traps within the band gap. Unstable shallow traps will release the electron at room temperature as part of the fading process, while stable traps will hold the electron charge. Once the dosimeter is heated, the electrons release from the traps and recombine into the holes that were once left releasing visible light that will be read out in a TLD reader. The reader produces a glow curve, which is a plot of the light intensity versus temperature as seen in Figure 1.3.

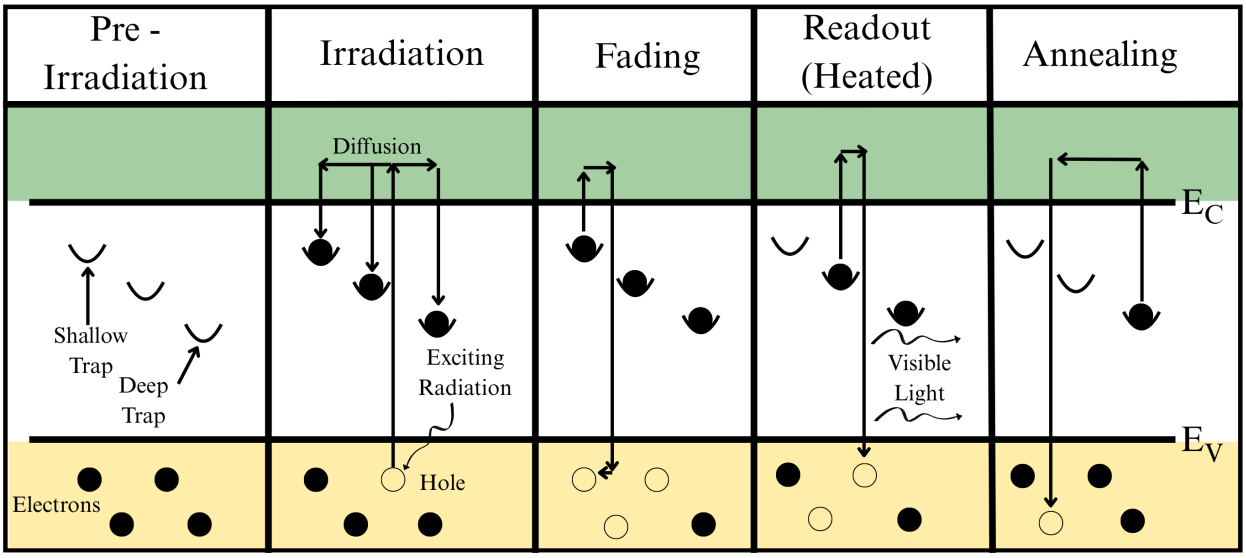

Figure 1.2: TLD Theory Schematic

Each peak on the glow curve correspond to a trap depth in the band gap. The highest peak of visible light intensity on the glow curve is correlated to the dose that the dosimeter received. Because of its high thermal stability, this peak is the primary feature used for dose calculation. Electrons in very deep traps may not be excited and recombine during the reading process; therefore, an annealing process is used to return the TLDs to their pre-irradiated state. Because the readout happens after exciting radiation is incident on the dosimeter, it is considered passive dosimetry, i.e., the dose is not actively read during the

irradiation. TLDs may be used multiple times because of the electron-hole recombination that allows for the process to be repeated.[35]

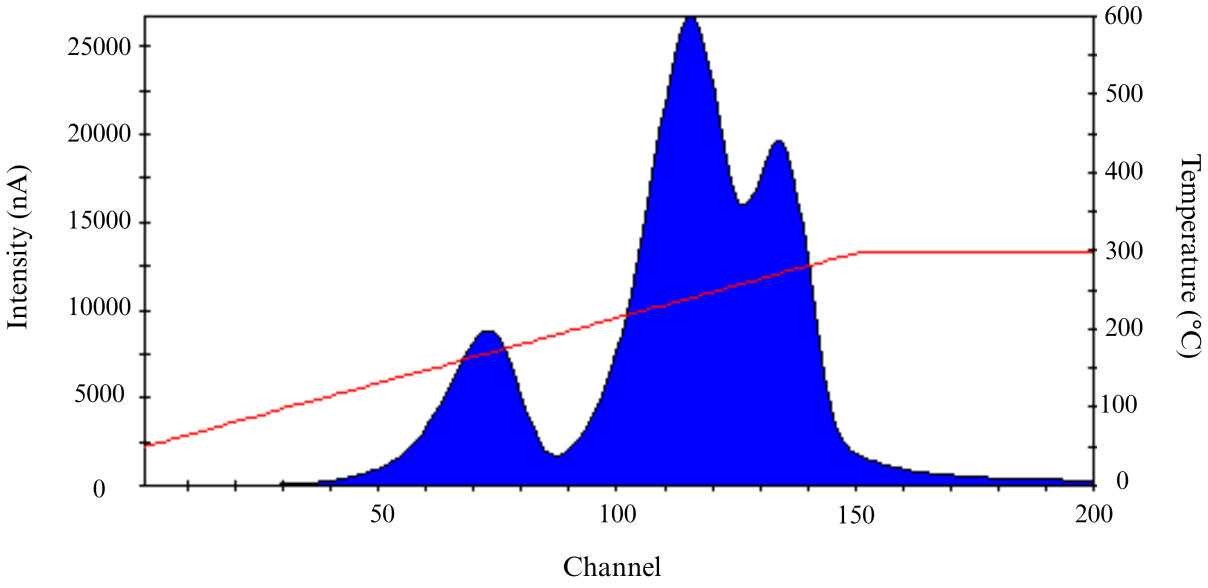

Figure 1.3: Example TLD Glow Curve[36]

A TLD reader is utilized to read the dose output. It uses a linear, programmable heating system to heat the dosimeters to the appropriate temperature for measurement. The reader then measures the thermoluminescent light output using a nitrogen-cooled photomultiplier tube and associated electronics. The WinREMS Software, which runs on a separate computer, provides the user interface, reader control, and applications software. The dosimeters are calibrated along with the reader to ensure the accuracy of the measuring system, this process is outlined in section 2.2.1. The results from the TLDs give benchmark measurements which are used to validate the Monte Carlo simulation.

1.5 Objectives

While advanced computational phantoms, such as those introduced in ICRP Publication 145, offer higher anatomical fidelity, their complexity leads to computationally intensive simulations. This complexity is particularly significant given that these phantoms help establish

ICRP dose coefficients and international safety regulations, forming the computational basis for subsequent ICRP publications. This presents a substantial barrier to their widespread adoption and raises a critical question: do these advanced models provide more accurate dose results than simpler models, or is the increased computational burden futile? Currently, there is a lack of direct, experimental benchmarks to validate whether the dosimetric accuracy of these complex models justifies their computational expense. The Monte Carlo dose comparisons of voxel and mesh phantoms using mono-energetic, broad parallel beams have been published conclude that while the dose calculations for most organs and penetrating radiation remain largely consistent, the mesh phantoms offer significantly improved accuracy for small and thin tissues and for weakly penetrating radiation[37]. However, the mono-energetic board parallel beams do not represent the source in most medical radiotherapy situations, nor do they include benchmark experimental data within the studies.

To address this gap, this research seeks to answer the following questions:

- How do dose distributions from modern mesh-type phantoms compare to traditional voxel phantoms, specifically during radiotherapy treatments?
- What is the quantitative trade-off between computational efficiency and dosimetric accuracy?
- Which computational model demonstrates dosimetric agreement with physical phantom measurements while preserving high-fidelity anatomical representation?

To assess the accuracy of these phantoms, benchmark calculations are performed and compared directly to experimental measurements.

As summarized in Table 1.1, this study utilizes a combination of experimental measurements and computational simulations across three distinct phantom types. The primary goal of this study is to benchmark the dosimetric accuracy of mesh-type and voxel-type phantoms against experimental measurements and clinical algorithms within a medical LINAC environment. To achieve this, the research is structured around three core objectives: experimental validation of the ATP simulations, cross-model accuracy assessment of the ATP and

ICRP phantoms, and a direct comparison between voxel and mesh geometries. To achieve this, the study will first develop a high-fidelity Monte Carlo model of a 6 MV Varian Clinac 2100C accelerator using the Particle and Heavy Ion Transport code System (PHITS). This model will be modified to represent the accelerator at the Kansas State University College of Veterinary Medicine (KSU Vet Med), including its 120-leaf multileaf collimator (MLC).

Table 1.1: Classification of Research Methodologies

		Simulated	
Phantom	**Experimental**	**Monte Carlo**	**Varian Eclipse**
ATP	X	X	X
Voxel		X	
Mesh		X	

The model used in this study was derived from a previously established Varian Clinac linear accelerator model, which was designed to accurately simulate radiation doses received outside the intended treatment area, a key factor in radiation-induced second cancers[31]. The in-field components of the model were validated using percent depth dose (PDD) and lateral dose profiles that matched the manufacturer's "gold standard" data. Furthermore, the out-of-field regions were validated against experimental data to accurately quantify scatter and leakage radiation. Through a comparison of Intensity-Modulated Radiation Therapy (IMRT) and 3D Conformal Radiation Therapy (3D-CRT), this research demonstrated that IMRT results in higher peripheral organ doses. This increase is attributed to greater leakage radiation, providing essential data for optimizing clinical treatment planning to mitigate secondary cancer risks This work also established benchmark organ dose data for an adult male using ICRP reference anatomy and for pregnant patients undergoing radiotherapy.

To replicate a clinical situation, radiotherapy will be planned using a DataSpectrum Anthropomorphic Torso Phantom (ATP) containing a simulated lung mass. The treatment plan will be created from the ATP CT scan and optimized to resemble a clinical plan using the Varian Eclipse software with the AAA model. Next, the absorbed dose will be experimentally measured at specific locations within the physical phantom using thermo-

luminescent dosimeters (TLDs) during the radiotherapy treatment. The dose distributions will also be calculated for the ATP, mesh, and voxel phantoms within the PHITS simulation using the same treatment plan. While the ICRP mesh and voxel models are standardized computational phantoms, the ATP will be segmented from CT imagery and converted into a PHITS-compatible simulation geometry to enable a direct comparison between all three models.

By analyzing this comprehensive dataset, the simulated dose distributions from all phantom types will be quantitatively compared to the experimental TLD results. This benchmark analysis will be specifically delimited to the PHITS simulation platform, a single accelerator energy and model, and one type of anthropomorphic torso phantom. The final objective is to evaluate the trade-off between accuracy and computational time for each phantom. The data obtained through this research will provide clear, evidence-based guidance for scientists on selecting a computational phantom that effectively balances the need for dosimetric accuracy with the practical demand for computational efficiency.

Chapter 2

Materials and Experimental Methodology

2.1 Experimental Dosimetry Equipment

2.1.1 Anthropomorphic Torso Phantom and Tumor Model

To represent human anatomy, an anthropomorphic torso phantom (ATP)[38] was utilized. This phantom simulates the upper torso of an average-to-large adult male/female (380 × 260 mm). To achieve realistic tissue densities, the cavities corresponding to the liver, heart, and general soft tissue were filled with deionized water.

The lungs were filled with polystyrene beads to simulate the low density of air-filled lung tissue in (Figure 2.1 on the left). Acrylonitrile butadiene styrene (ABS) pellets, commonly known as BBs, were used as surrogate dosimeters and placed at various locations within the phantom. Figure 2.2 shows the model of the ATP, where the small spheres are the dosimeters. To avoid biasing the radiotherapy treatment plan, these dosimeters were intentionally not placed in or near the defined tumor volume.

For more realistic dosimeter placement within the lungs, a bronchial tree was 3D-printed from a standard .stl file representing an average male anatomy[39;40] shown in Figure 2.1 on

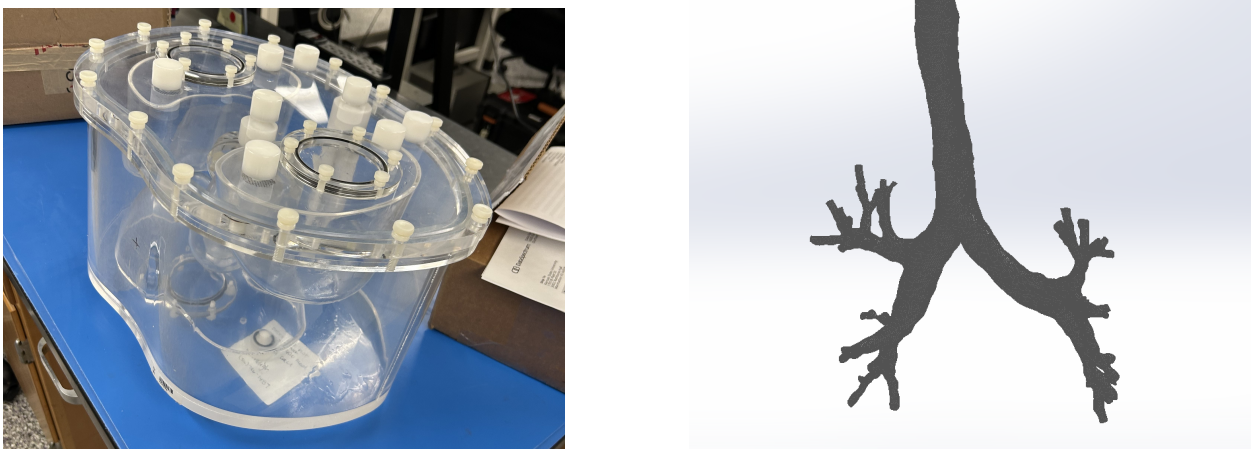

(a) Empty ATP phantom.

(b) SolidWorks bronchial tree.

Figure 2.1: Image of empty Anthropomorphic Torso Phantom (left) and the SolidWorks model of the bronchial tree (right).

the right. The tree was fabricated using thermoplastic polyurethane (TPU) with a low infill percentage to closely match the density of a human bronchial tree, which was approximated as the density of water for this simulation. This addition allowed for the placement of dosimeters along the bronchial branches, providing measurement points deep within the lung volume and not just on the organ's periphery.

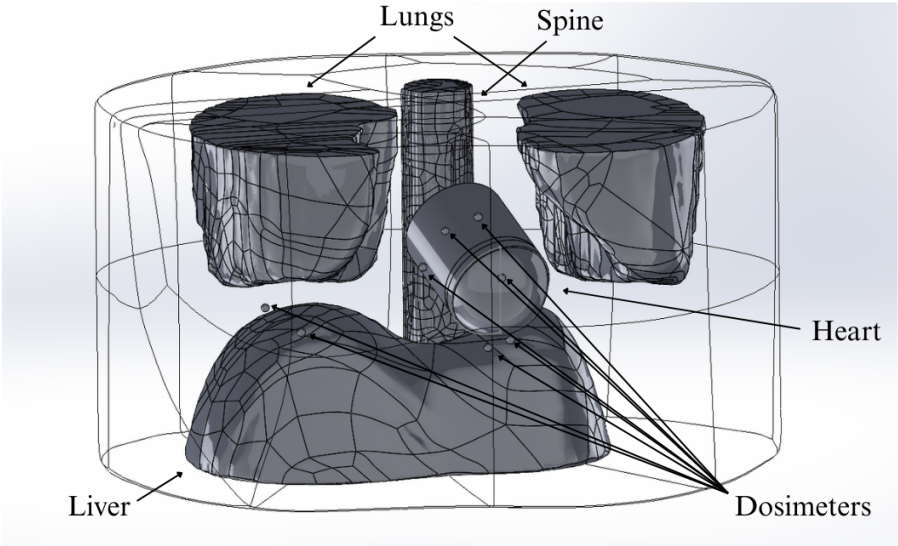

Figure 2.2: Solidworks model of ATP

Another addition to the phantom is a rubber ball representing the tumor. The tumor is spherical, 2.3 cm in diameter, and was placed on the bottom of the right lung. It is denser than the polystyrene beads, so it was able to show up clearly on the CT scan. This mass represents a pseudo-squamous cell lung cancer, a common type of non-small cell lung cancer. Although the rubber ball is representative of the tumor, the simulated tumor will have a density of 1 g cm^{-3} and closely match the elemental composition of tumor tissue.

2.1.2 Thermoluminescent Dosimeter (TLD) Properties

The dosimeters used for the experimentation were the Thermo Fisher Scientific High Sensitivity LIF: Mg, Cu, P Thermoluminescent Dosimetry Materials[41], more commonly called TLD-100H. The size of the chips were 3.2 x 3.2 x 0.89 mm, with a resulting volume of about $9.1 \times 10^{-3}\,cm^3$. The TLDs were used in conjunction with Thermo Fisher Scientific Model 3500 TLD Reader[36] for TLD readout. TLD-100H was utilized because of the linear range from 1 µGy to 10 Gy, which will allow for the higher dose received during radiotherapy treatments.

2.1.3 The Medical Linear Accelerator (LINAC)

The radiation source for all experiments was the 6MV Varian Clinac 2100C, located at KSU Vet Med (Figure 2.3). This LINAC's component configuration is identical to the one described in Section 3.1.2. This machine was used for all experimental irradiations, including TLD calibration (Section 2.2.1) and the final treatment delivery (Section 2.2.3). Delivering a prescribed dose requires a treatment planning process to determine the necessary monitor units (MU) for the exposure. A monitor unit (MU) is a machine-specific measure of accelerator output, quantifying the radiation produced. While MU is directly proportional to the absorbed dose delivered to the patient, it is not a dose quantity. The calculation of MU for a specific plan depends on multiple parameters, including source-to-surface distance (SSD), field size, and the properties of the attenuating medium. The KSU Vet Med LINAC was operated at a nominal dose rate of 300 MU per minute for all experimental procedures,

aligning with the established clinical protocols utilized by the KSU Vet Med for routine treatments.

Figure 2.3: KSU Vet Med Medicine 6MV Varian Clinac 2100C

2.2 Experimental and Computational Procedures

2.2.1 TLD Calibration with a 6MV Photon Beam

To mitigate measurement error and ensure a uniform response, a calibration procedure was performed for the TLD-100H dosimeters[36]. A 10×10 cm^2 field size was selected, as this matches the field used for the KSU LINAC clinical calibration. For the procedure, 40 TLD-100H dosimeters were arranged at the isocenter, which is the intersection point of the LINAC axis of gantry rotation and the central axis of the radiation beam. A 1.5-cm thick tissue-equivalent bolus was placed on top of the dosimeters. This bolus served two functions: it provided the necessary build-up to establish charged particle equilibrium (CPE) at the

dosimeter depth, as shown in the PDD curve in Figure 2.4, a depth of 1.5 cm corresponds to d_{max} (100% dose) for this beam energy, and maintained a scatter factor of unity.

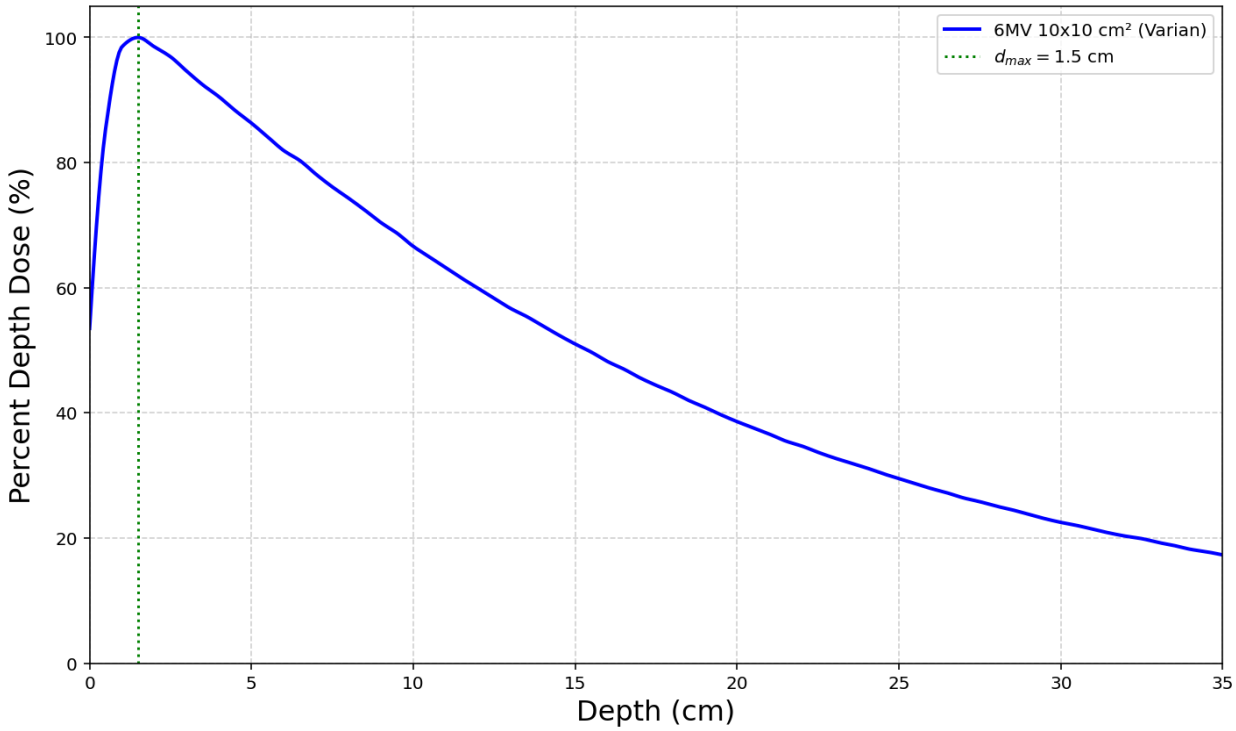

Figure 2.4: Percent Depth Dose Curve of 6MV Varian LINAC for 10 × 10 cm^2

This setup resulted in a source-to-surface distance (SSD) of 98.5 cm (to the bolus surface), while the TLDs remained at the 100 cm source-to-axis distance (SAD). Each dosimeter was sealed in a 0.05 mm thick polythene bag. This protected the TLDs from direct contact with the bolus material and, importantly, replicated the experimental conditions in the torso phantom, where the same bags were used to waterproof the dosimeters. The calibration exposure consisted of a single, anterior-posterior (AP) field (0° gantry angle) delivering 97 MU utilizing the clinical calculations provided by KSU Vet Med to achieve a target dose of 1 Gy while maintaining a scatter factor of 1.0.

The calibration procedure was done over multiple days to establish an element correction coefficient (ECC) and reader calibration factor (RCF). The ECC is established because of the TLD material and mass variations that could account for up to 15% (based on 1 sigma) error. The RCF is established to maintain a consistent output from the reader over a period

of time. Both the ECC and RCF are used to calculate the exposure for each TLD using the following formula:

$$Exposure = \frac{ECC \times Charge}{RCF}. \tag{2.1}$$

The procedure for the calibration is demonstrated in Figure 2.5. In each step of the calibration, the dosimeters were prepared by annealing 3 hours pre-irradiation, exposure, then readout for calibration purposes 2 hours post irradiation. The TLD-100H dosimeters were annealed at 240 °C for 10 minutes (per the material instructions) with an approximately 10 °C min^{-1} rise time and a 10 minute cool time in room temperature. While TLD-100H dosimeters have a negligible fade up to 3 months, the time between irradiation and readout was kept consistent.

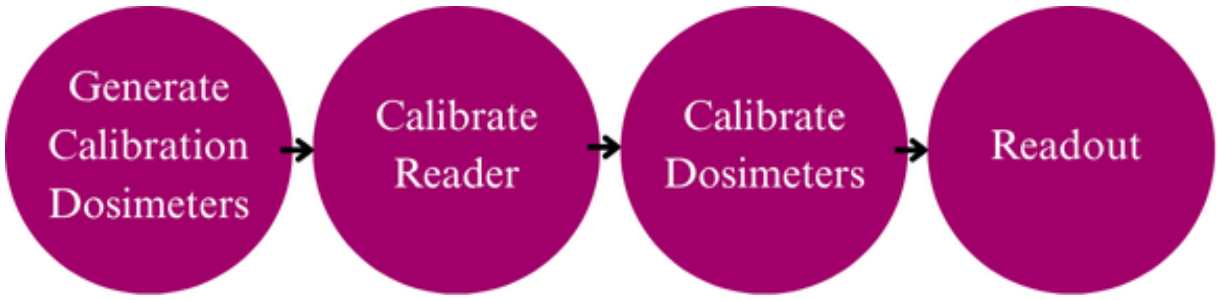

Figure 2.5: Calibration Procedure for TLDs[36]

In the "Generate Calibration Dosimeters" step, an ECC for each dosimeter is established without reference to a reader: 40 dosimeters were prepped, irradiated, and read. During the Generate calibration dosimeters step 31 out of 36 dosimeters were accepted with a 4.905% deviation (the computer faulted at 37, so 37-40 were disregarded). Then, during the calibrate reader step, the calibration dosimeters were used to define a singular RCF for the reader. This step accepted 30/30 dosimeters tested with a 1.789% deviation. Finally, for the calibrate dosimeters step, the previous ECCs are wiped clean to establish new field dosimeter ECCs that will be used along with the RCF. The new set had 38 dosimeters prepped and irradiated: 32 of 38 dosimeters were accepted with a 4.916% deviation, establishing the final ECCs for readout. The initial 5% deviation observed during the Generate Calibration Dosimeters and Calibrate Dosimeters stages is considered acceptable, as the ECC effectively accounts for

the inherent sensitivity variations caused by elemental impurities in each crystal. Once the entire calibration procedure was completed, the combined application of the RCF and ECC reduced the total dosimeter error to 2%.

2.2.2 CT Scanning and Treatment Planning

To help develop a treatment plan for the tumor, a preliminary CT scan was performed with the pseudo dosimeters (BBs) and the fill materials in the phantom. The CT scan was conducted at KSU Vet Med and was used to identify the tumor target location and other organs at risk (OARs), a process called segmenting, or contouring, shown in Figure 2.6.

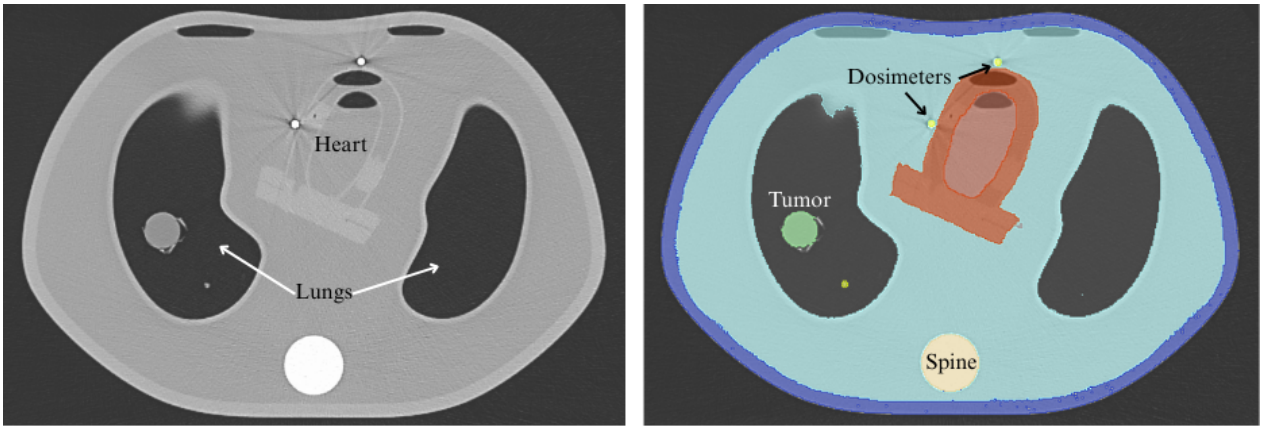

Figure 2.6: Segmentation of CT slice

The OARs identified include the body, lungs, heart, and spine due to their proximity to the tumor and their inherent radiosensitivity. Segmenting of these organs is essential to ensure that the treatment plan delivers the proper dose to the tumor while keeping the surrounding healthy tissue doses below safety thresholds. This concept is described as the therapeutic ratio: the comparison between the probability of damaging healthy organs versus the probability of killing the cancerous tumor.[42] In clinical practice, the objective is to maximize the therapeutic ratio, thereby widening the window between tumor destruction and the radiological effects in normal tissues.

Through contouring the oncologist will define the gross tumor volume (GTV) which is the visible extent of the tumor. To account for microscopic diseases around the GTV, the

clinical target volume (CTV) is defined. On the outer layer of the GTV and CTV is the planning target volume (PTV), which is the margin for uncertainties and movements that happen during treatment. Each specific volume makes up the entire tumor target and is demonstrated in Figure 2.7.

After segmenting, the majority of the treatment planning takes place: plan design and optimization. Radiation beams are set to deliver a prescribed dose to the PTV while minimizing the dose to the OARs. To guide treatment planning, KSU Vet Med's radiation oncologist employs the software program Varian Eclipse[43] using the AAA calculation model described in Section 1.2. The oncologist works to provide optimal dose to the tumor, optimizing fraction weights, beam numbers, angles of entry, and beam shaping (field size and MLC configuration). Of the available tools, a dose volume histogram (DVH), shown in Figure 2.9, is used to compare doses from different OARs and the GTV to aid in planning. To complement the data of the DVH, a spatial dose map is utilized to visualize the dose distribution throughout the anatomy, as illustrated in Figure 2.8.

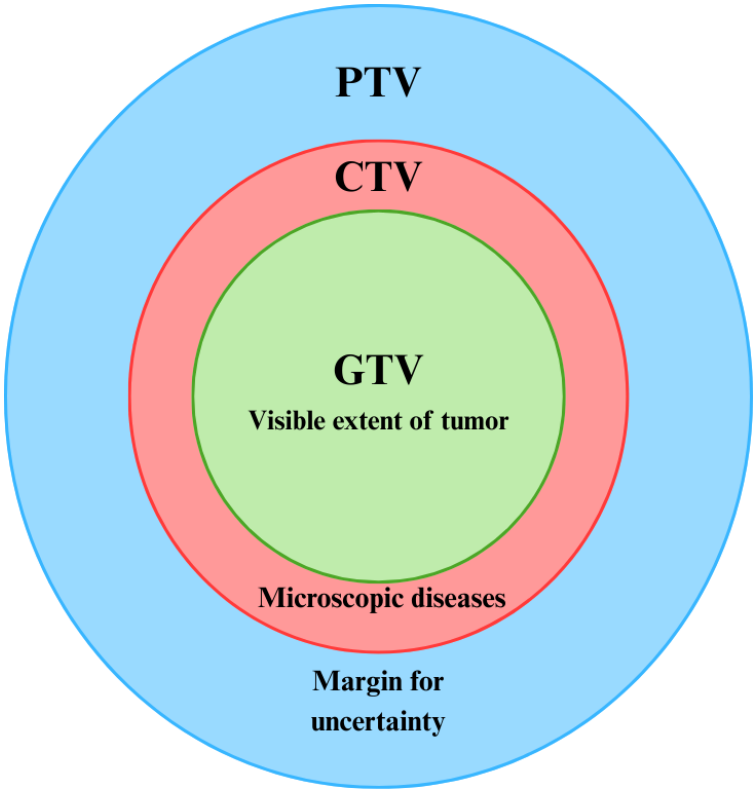

Figure 2.7: Representative GTV, CTV, and PTV

To simulate a representative treatment, a treatment plan was created for the ATP based off of the CT scan. While real treatment would take place over multiple fractions, only a singular fraction of 2 Gy was used in this work. The fraction is separated into four fields, each 90 degrees from the last. The field values can be found in table 2.1 and the MLC dimensions of each field can be found in Appendix A.

To see the representative dose distribution, a "beam's eye" view gives a image of the

fields in Figure 2.10. This shows the four fields, where field 1 is at 0° going from the anterior to the posterior, the opposing field is field 3 at 180°, field 2 is at 90° going from the left to right side, and that opposing field is field 4 at 270°. While the MLC changes slightly going from field to field, the general shape is a circle that encompasses the PTV.

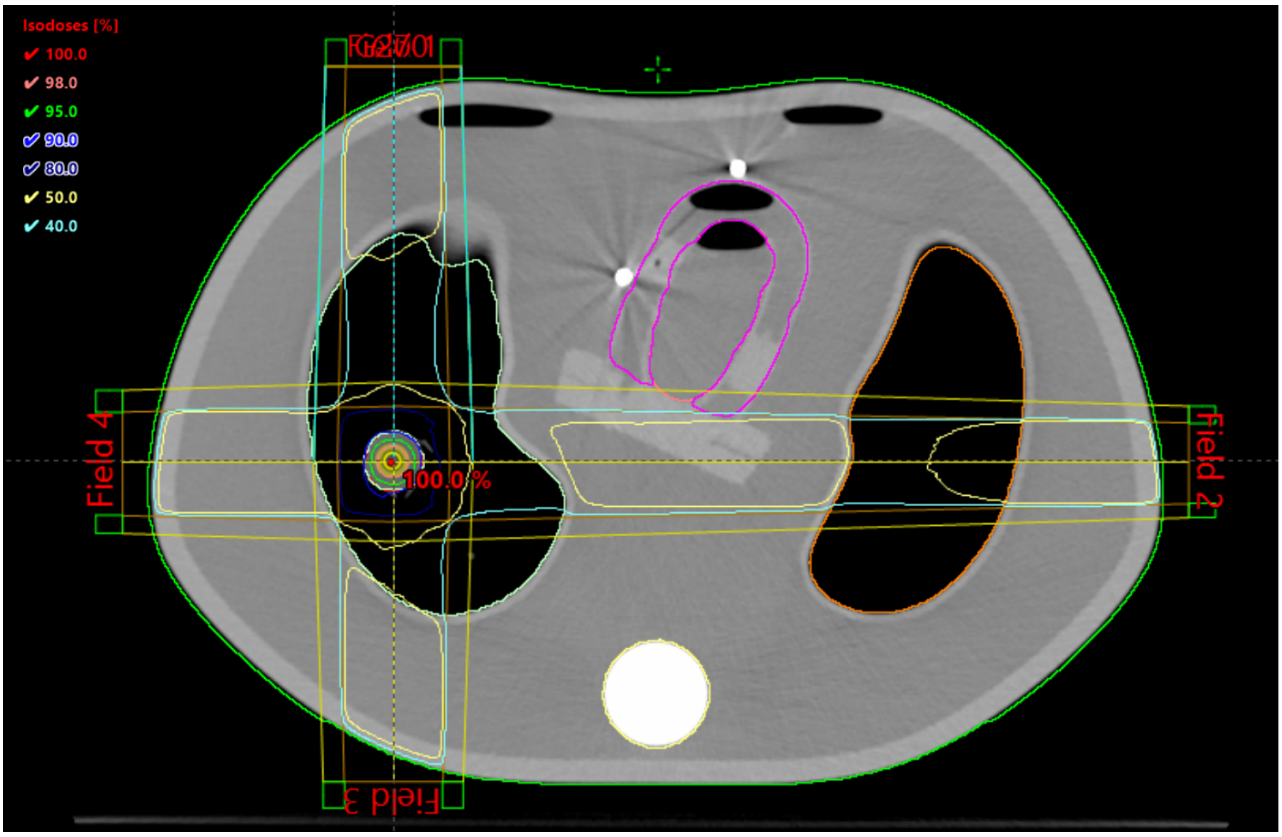

Figure 2.8: AAA Calculated Dose Map

Table 2.1: Treatment Plan Report

ID	Machine	Energy	Scale	Weight	Size (cm)	Gantry	Calculated SSD (cm)	MU
G0	2100C	6X	Varian IEC	0.000	6.0 × 6.0 (Asym)	0.0 deg	86.1	Setup field
G270	2100C	6X	Varian IEC	0.000	6.0 × 6.0 (Asym)	0.0 deg	86.1	Setup field
Field 1	2100C	6X	Varian IEC	0.250	6.0 × 6.0 (Asym)	0.0 deg	86.1	72
Field 2	2100C	6X	Varian IEC	0.150	6.0 × 6.0 (Asym)	90.0 deg	71.0	71
Field 3	2100C	6X	Varian IEC	0.250	6.0 × 6.0 (Asym)	180.0 deg	89.0	69
Field 4	2100C	6X	Varian IEC	0.350	6.0 × 6.0 (Asym)	270.0 deg	90.8	95

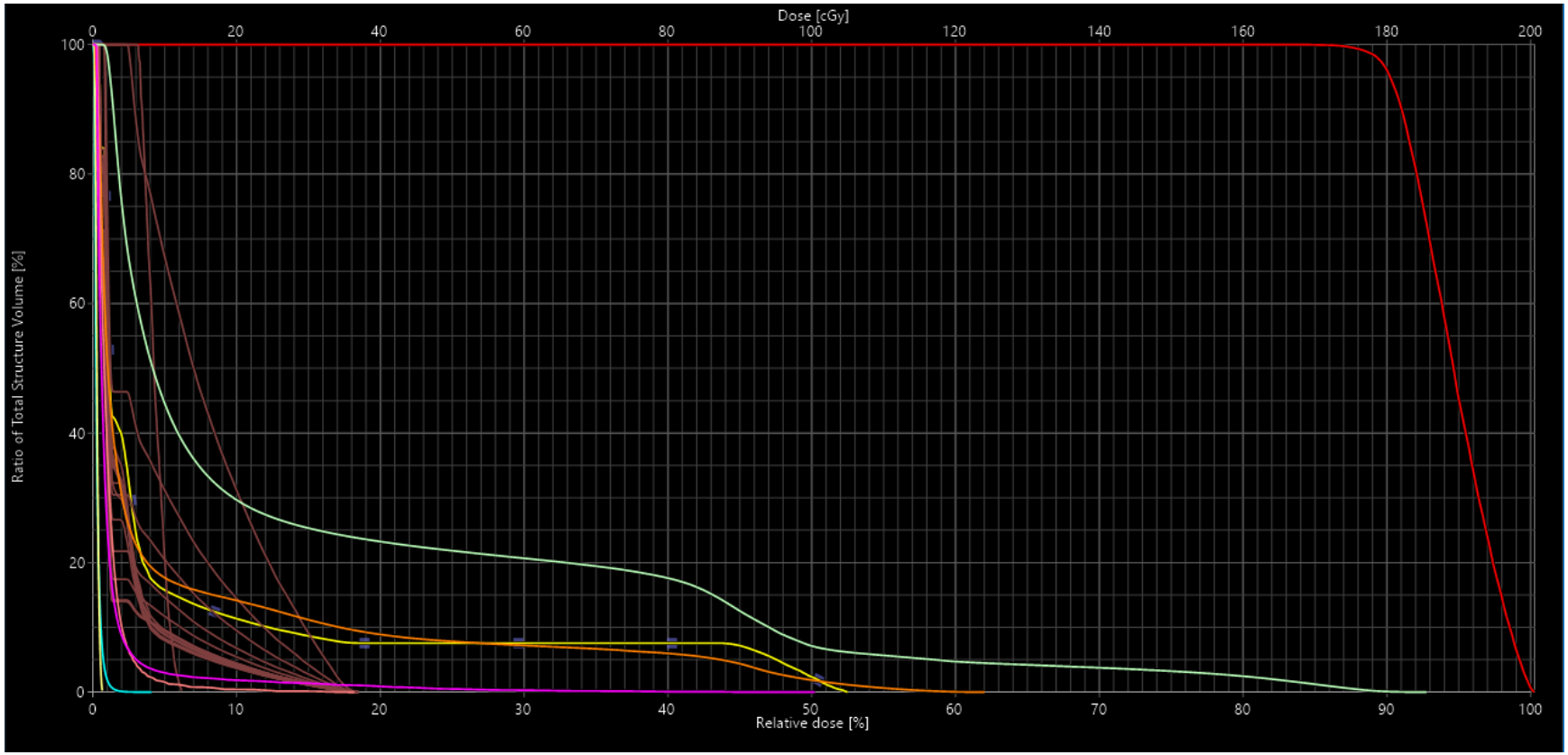

Figure 2.9: DVH

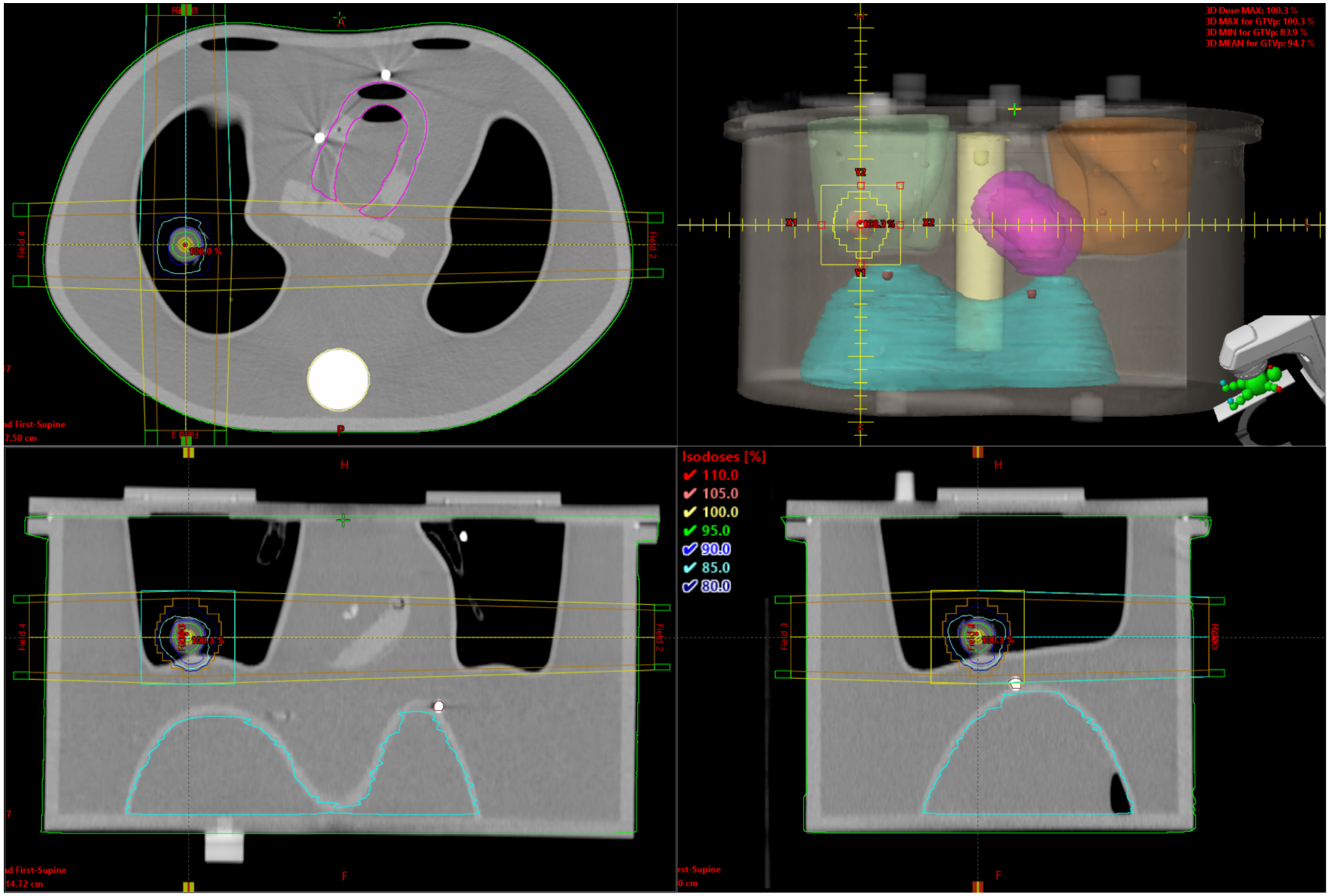

Figure 2.10: Isodose views of ATP from Treatment Plan

2.2.3 Four-Field Treatment Delivery and TLD Location

Following TLD calibration and treatment planning for the ATP, the treatment is ready to commence. A total of 30 TLDs were used throughout the body with five on the liver, five within the right lung, five within the left lung, five on the outer heart, five on the tumor, and the last five placed in line with the beam. For data collection purposes, dosimeters have been classified into three different categories. The first is in the target, where dosimeters are located at the intersections of the four field beams and encompass the PTV. The next is partially in target, where the dosimeter is located in line with one of the beams and includes the tissue the beam goes through to get to the target. The final section is out of target, which the dosimeters correspond to the OARs and other normal tissue outside of any beam.

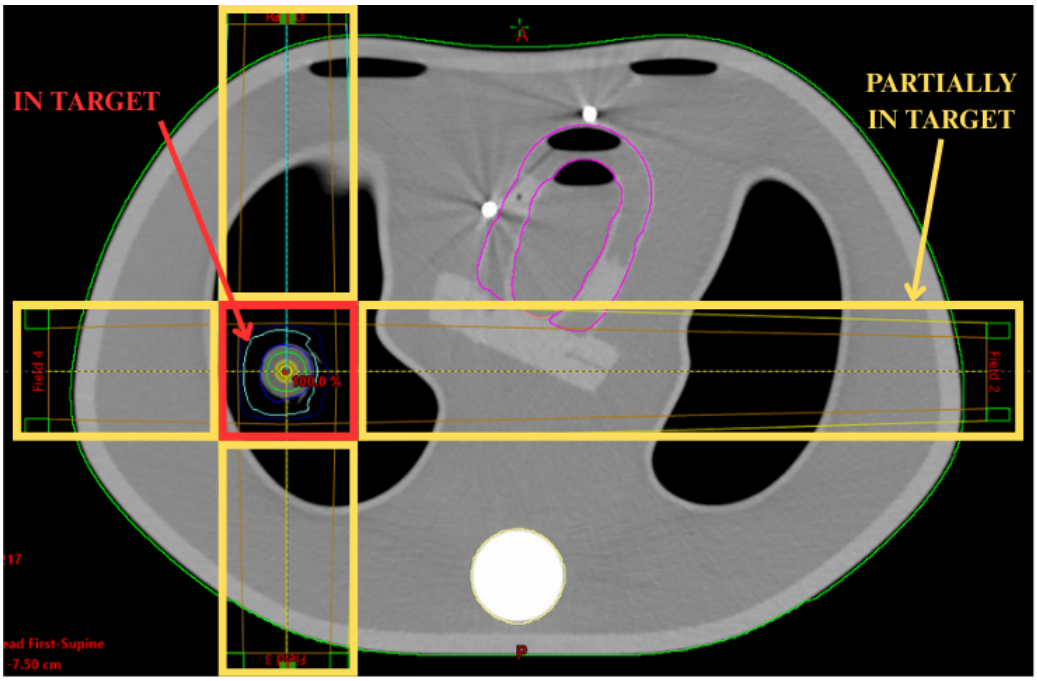

Figure 2.11: Dosimeter location nomenclature

To ensure consistency with the calibration (Section 2.2.1), all TLD handling procedures were kept identical, including the TLD annealing process and maintaining consistent time intervals between annealing, irradiation, and readout. Precise phantom alignment was achieved using an external reference point (a small BB). This marker was used to position the phantom on the treatment table, which was then adjusted to align the beam's central axis with

the target tumor location. During treatment, the LINAC gantry rotated around the phantom to deliver each field in the plan. The resulting dose measurements from the dosimeters are presented in Section 3.2 in conjunction with the simulated results.

Chapter 3

Development and Validation of the Monte Carlo ATP Model

3.1 Monte Carlo Simulation Framework

3.1.1 Monte Carlo Modeling and Transport Parameters

For the simulation of radiation transport within the LINAC model, this research employs the PHITS Monte Carlo code. The simulation is structured using specific input blocks known as cards, which are standardized command sets used to define the geometry, physics, and output parameters of the Monte Carlo environment. The parameters card is used to define the number of particles simulated, physics models used, a minimum energy cutoff, and a function to restart the calculation from the previous batch. The model used for this research was Electron-Gamma Shower version 5 (EGS5), which is used for transport of electrons and photons. For low energy deposition electrons, this uses the continuous slowing down approximation for computational simplicity, and for photons, interactions such as the Photoelectric Effect, Compton Scattering, and Pair Production are modeled. The cross section library for the EGS4 model was the Evaluated Electron/Photon Data Library (EEDL/EPDL). This library presents cross-sections and interaction probabilities for atoms

of different atomic numbers. The restart function is used when the number of particles simulated initially fails to produce acceptable uncertainties (less than 5%). The energy cutoff used for photons was 1 keV and 10 keV for electrons. These values were chosen for simulation time optimization while maintaining high tally accuracy.

Although most of these sections are consistent across each input file, there are a few variations that will be outlined for each input. The most notable differences are in the surface, cell and transform definitions. This includes the three phantoms used throughout the simulations, and the set up for the TLD calibration process. The source did not change throughout any of the cell cards because all files were modeling the medical LINAC used during experimentation. The source card portrays an electron beam with a lateral width defined by a FWHM of 0.3061 cm in both the x and y directions directed along the z-axis with a gaussian energy and spatial profile to represent the electrons that are incident on the target. After the electrons hit the tungsten target, a forward beam of x rays become incident on the phantom.

The materials remain fairly consistent across each input, with material definitions of the voxel and mesh phantoms being taken from the ICRP data set and simple materials were used to define the cell cards for the ATP and calibration. The surface card defines the boundaries of each cell, and the cell card defines the volume inside those surfaces. The cell includes the type of material, the density of the material, and which surfaces define the boundaries. The volume card is used to define the volume for each cell explicitly. The tally cards are used to not only calculate the dose to each cell using T-deposit, but also track particle length with T-track. Finally, transform cards were used to define how certain cells were to be rotated or moved. The transforms are able to rotate the phantoms, MLC, and TLDs. The tally card is also used to visualize a 2D slice of the geometry created when the calculation mode is changed in the parameters.

3.1.2 Simulation Geometry and Exposure Scenarios

A 6MV Varian Clinac 2100C linear accelerator PHITS model was adapted from a previous LINAC model developed for the calculation of Monte Carlo doses from radiation therapy treatment[31]. While the fundamental components were preserved, significant modifications were made to the multileaf collimator (MLC) to accurately represent the Varian Millennium 120-leaf MLC available at the KSU Vet Med. This change involved modeling 40 inner leaf pairs (80 leaves total) with a 0.5-cm resolution and 20 outer leaf pairs (40 leaves total) with a 1.0-cm resolution. This higher definition allows for greater precision when treating small, intricate tumors. Another key modification was an increase in the leaf tip's radius of curvature to 16 cm. This larger radius creates a gentler curve that better approximates the beam's divergent path, enhancing precision for high-dose radiosurgery. Figure 3.1 shows the open view of the MLC. Each leaf comes together in a tongue-and-groove effect, highlighted in Figure 3.2, to ensure a proper dose distribution. This design prevents interleaf radiation leakage that could bias the dose to the patient.

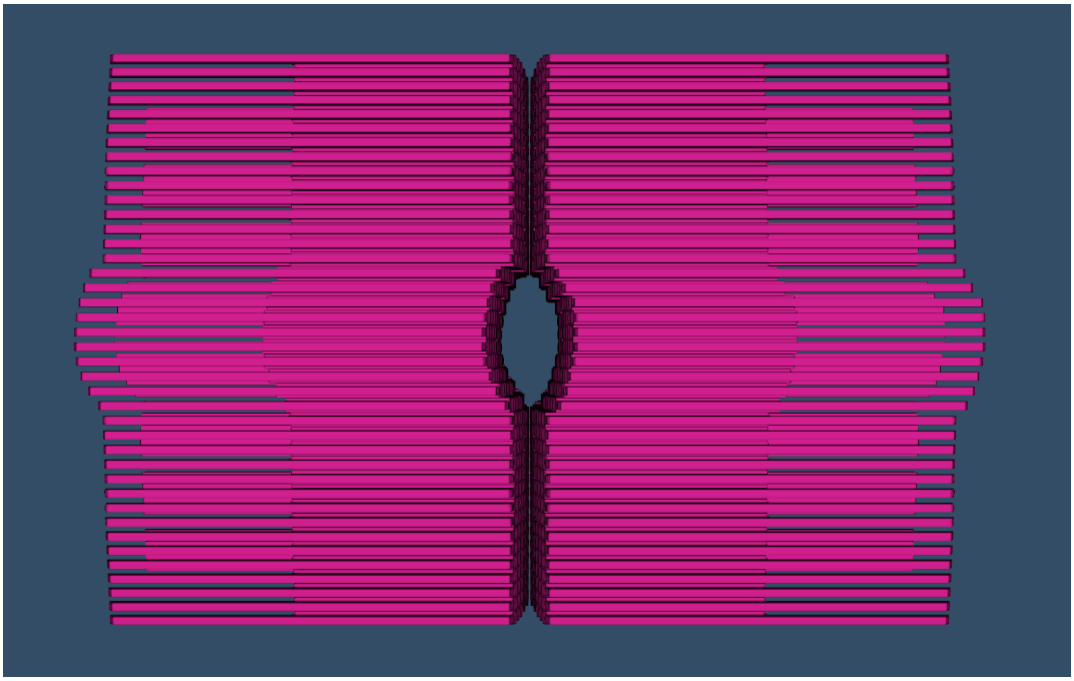

Figure 3.1: Open MLC for field 1 of treatment

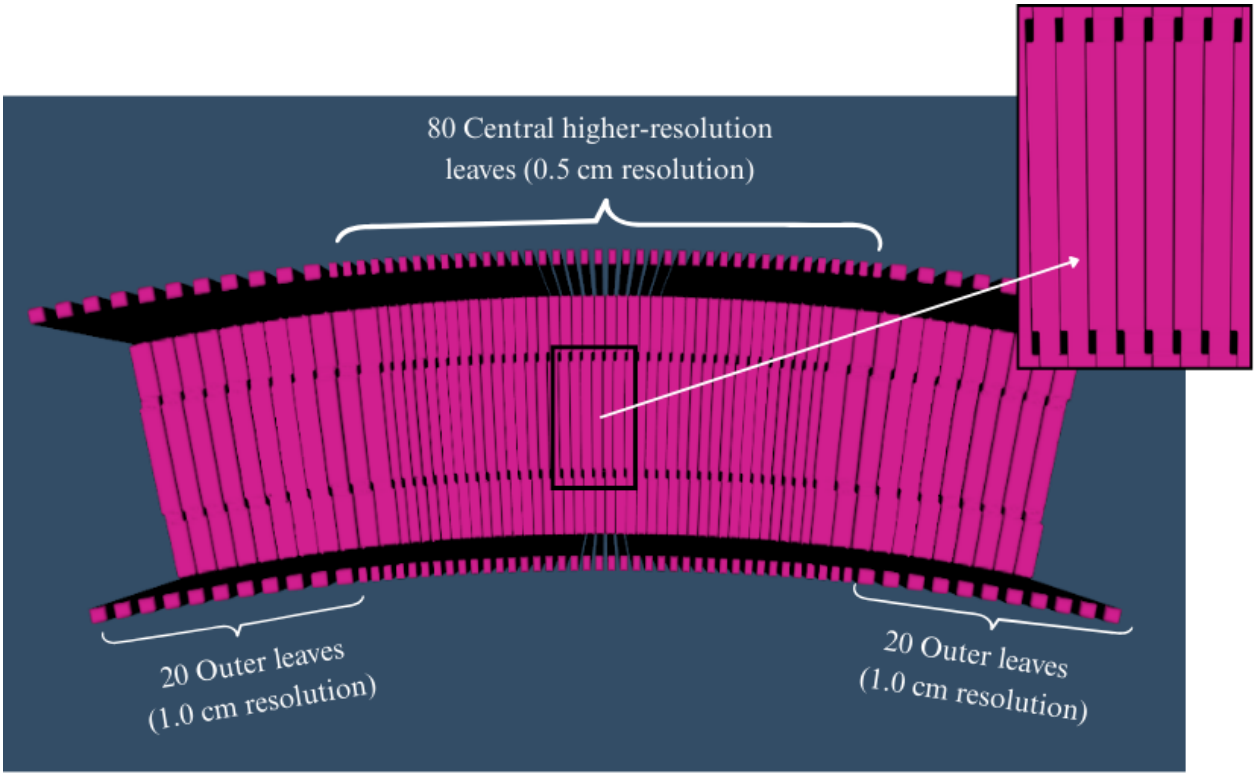

Figure 3.2: Side view of MLC with tongue-and-groove effect

The modeled accelerator head shown in Figure 3.3 is composed of two main assemblies: the beam-line components, which produce and shape the therapeutic beam, and the surrounding shielding components, which absorb stray radiation. The beam's journey begins at the tungsten target and its copper backing, where the X-rays are generated. From there, the beam receives its initial shaping from the primary collimator, after which an entirely copper flattening filter ensures the beam has a uniform intensity across the treatment field. The beam then passes through a monitor chamber to measure the radiation output before being further defined by the secondary collimators (jaws) and the multileaf collimator (MLC). Completing the structure of the accelerator head are the various shielding components. These encase all of the beamline assemblies, mitigating leakage by absorbing scattered radiation.

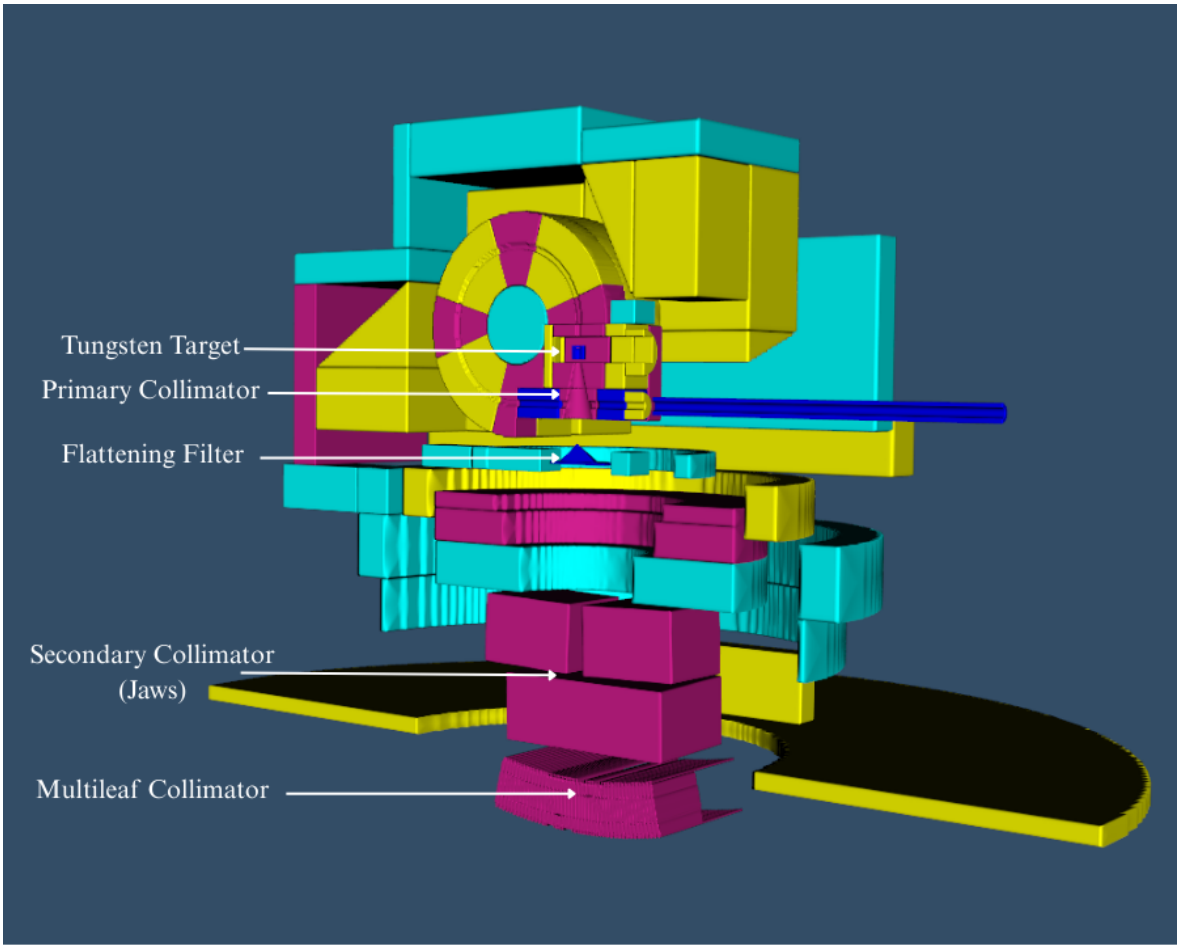

Figure 3.3: Modeled LINAC head with beam-line components defined

In the PHITS simulation, the trcl (transform) function was used to position both the secondary collimator jaws and the MLC leaves. To define a specific a cm $\times$ b cm field size, the jaw angles were calculated relative to the 100 cm source-to-axis distance (SAD) using the following equations:

$$\theta_a = \tan^{-1}\left(\frac{a/2}{100\text{ cm}}\right) \tag{3.1}$$

$$\theta_b = \tan^{-1}\left(\frac{b/2}{100\text{ cm}}\right). \tag{3.2}$$

This 100 cm SAD value was chosen to match the constant source-to-axis distance used during radiotherapy treatments at KSU Vet Med. For the MLCs, the trcl function was applied to define the curved leaf-end geometry and to simulate the independent movement of each leaf in the x-direction, accurately replicating the capabilities of the physical MLC.

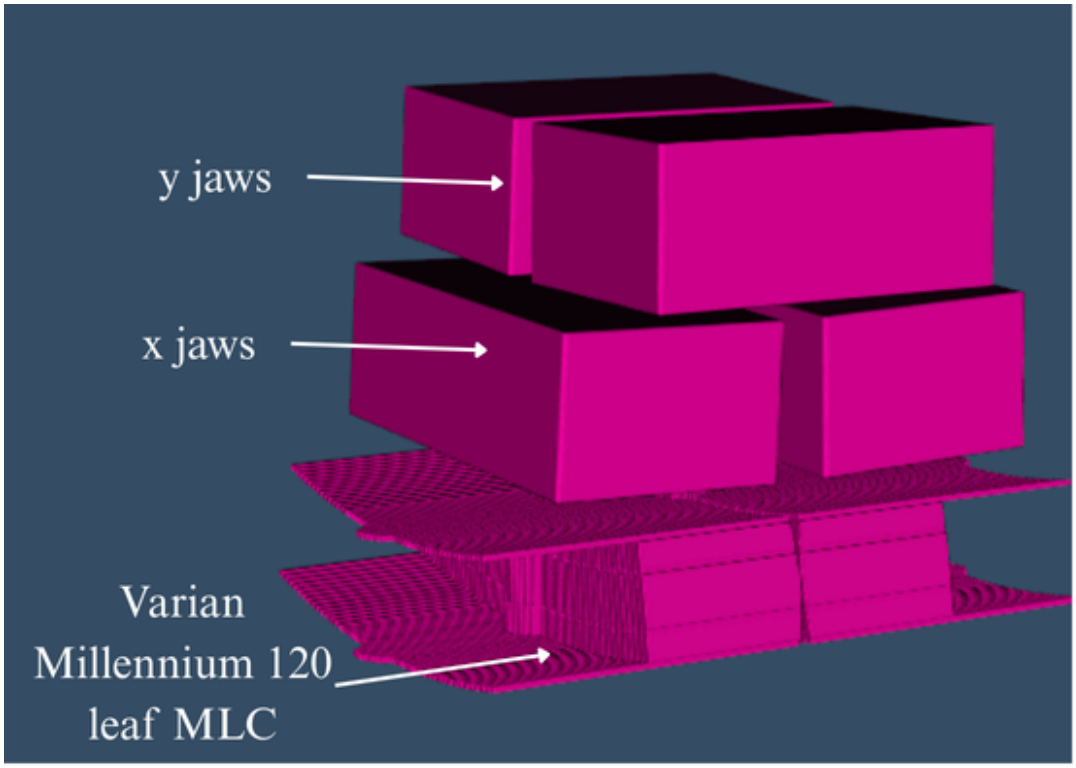

Figure 3.4: Model of the secondary collimator jaw and MLC

3.1.3 Computational Modeling of the LINAC and ATP

To simulate the treatment plan, the ATP was converted into a format that could be read by the PHITS code, and the LINAC model was edited to match the actual treatment. Beginning with the source definition of the simulated treatment, this process involved simulating the calibration process discussed in Section 2.2.1 to obtain the normalization factor for the source. The geometry of the simulation only changed at the field where the TLDs were simulated. The TLD-100H material composition and density were given by the Thermo Fisher Scientific via email[44] and shown in Table 3.1. Like the experimental calibration,

Table 3.1: Composition and Density of TLD-100H

Material	**^{7}LiF** (%)	**^{6}LiF** (%)	**Mg** (ppm)	**Cu** (ppm)	**P** (ppm)	**Density** ($g\,cm^{-3}$)
TLD-100H (^{Nat}LiF: Mg,Cu,P)	~92.14	~7.36	~2000	≤40	~3000	2.48

the simulated calibration used a 10 x 10 cm field where the MLC was opened up to its

maximum extent. The simulated calibration geometry is shown from a bottom-up view in Figure 3.5. The 40 TLD-100Hs were placed in field with a plastic covering (light green), followed by a bolus (dark green) to replicate the physical calibration. While the experimental calibration involved three separate 1 Gy exposures, the simulation was run a single time. This simulation source normalization was set to 1, which means its raw output is in units of Gy/source. Based on the medical LINAC, which delivers a dose of 1 Gy (with a 2% uncertainty) for 97 MU, the clinical dose rate can be found. This clinical normalization factor is: 1 Gy/97 MU $\approx$ 0.0103 Gy/MU with a SAD of 100 cm.

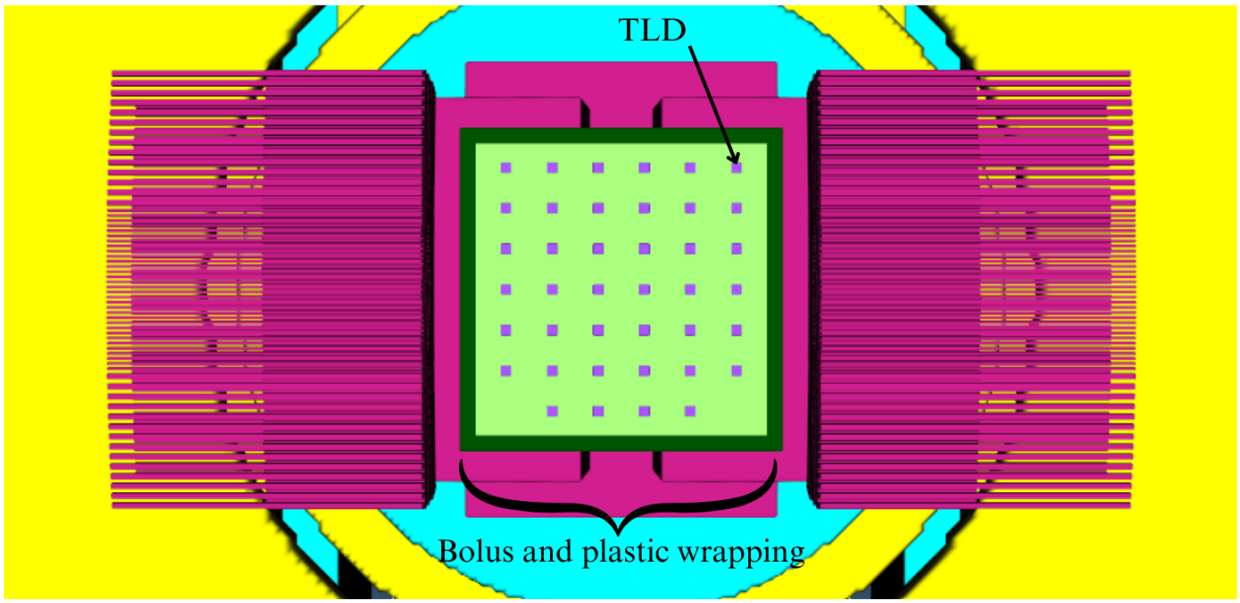

Figure 3.5: Model of calibration, bottom up view

A final normalization factor (NF) is required to bridge the clinical MU with the simulation's Gy/source output. This NF, with units of Source/MU, was found using Equation (3.3). In this equation, the 1 Gy is the LINAC calibration dose, the 97 MU is from the LINAC calibration MU, and the 1.2297×10^{-16} is the raw Gy/source output from the PHITS calibration simulation.

$$\frac{1 \text{ Gy}}{97 \text{ MU} \times 1.2297 \times 10^{-16} \frac{\text{Gy}}{\text{Source}}} \approx 8.38 \times 10^{13} \frac{\text{Source}}{\text{MU}} \tag{3.3}$$

Then, in Equation (3.4), the process to obtain the final dose for any treatment simulation is shown. The final result is the product of this NF (8.38×10^{13} Source/MU), the new

simulation's raw output (Result in Gy/Source), and the prescribed MU for that specific field.

$$8.38 \times 10^{13} \frac{\text{Source}}{\text{MU}} \times \text{Result in } \frac{\text{Gy}}{\text{Source}} \times \text{Field MU} = \text{Final Result in Gy} \tag{3.4}$$

To simulate the treatment, the experimental ATP was translated into a computational model compatible within the PHITS code. While direct import of the CT scan into PHITS was initially considered, it proved infeasible for distinguishing between organs with similar Hounsfield units. This was problematic for the ATP because the internal structure, excluding the lungs, was filled with deionized water. Therefore, a manual segmentation process was adopted, as outlined in Section 2.2.2. KSU Vet Med segmented each anatomical region of interest and exported them as an .stl file, which allowed for smoothing and refinement within Meshmixer, a 3D modeling software[45]. These individual parts were then combined into a single CAD assembly in SolidWorks[46]. This assembly was subsequently processed using Gmsh[47] to generate the final tetrahedral mesh.

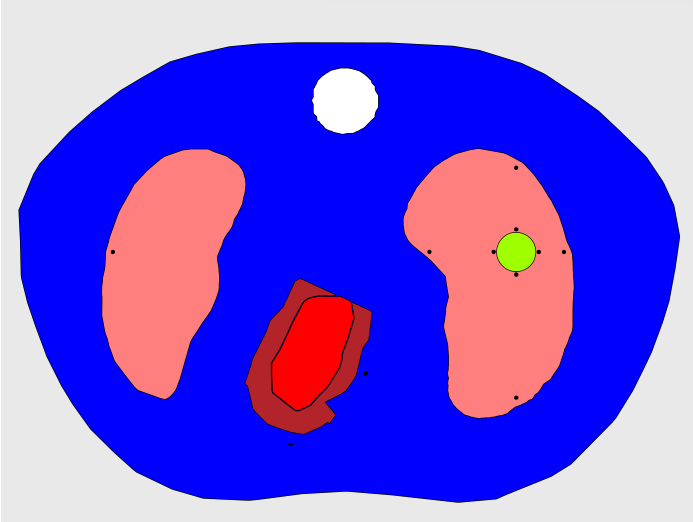

Figure 3.6: Cross-section of PHITS ATP model at tumor location

The procedure in Gmsh involved several steps. First, geometric coherence was enforced to ensure all parts were flush and did not overlap. Next, 29 different regions were defined, including the lungs, tumor, spine, liver, inner and outer heart, the main body, and the dosimeters. Finally, the assembly was converted into a 3D mesh and exported as a NAS-

TRAN (.bdf) file. This mesh file was then imported into the simulation using the nfile function in PHITS. A scaling factor was applied with the TSFAC function to correct for size discrepancies from the multi-software workflow, and the final model measurements were validated against the physical phantom.

To streamline the computational model, the heterogeneous physical medium of polystyrene beads was approximated as a homogeneous polystyrene medium within the PHITS environment. While this transition introduces a geometric discrepancy due to microscopic air pockets between the beads, the resulting error is considered negligible due to the mass conservation achieved during phantom assembly. By manually compressing the beads into the lung cavity to reach a maximum packing fraction, the experimental mass closely approximated the simulated model, ensuring that the bulk density (ρ_{bulk}) remained effectively identical. Since the linear attenuation coefficient (μ) for a 6MV photon beam is directly proportional to the electron density of the medium, the ratio of experimental to simulated attenuation (μ_{exp}/μ_{sim}) is approximately 1.02. Consequently, this minimal 2% variance is insignificant compared to the overall dose trends observed, confirming that the homogeneous model remains an appropriate representative of the physical bead-filled environment.

After the phantom was implemented into PHITS, it must be translated and rotated to comply with the rotation of the treatment and the 100 cm SAD. This was achieved using the Transform section within PHITS. Each transform number (n) is associated with a gantry angle for the treatment. M is the mode in which the coordinate transformation occurs. When $M = \pm 1$, components of a rotation matrix can be directly given by $B_i (i = 1, \cdots, 9)$. The coordinates before and after the transformation are defined as (x, y, z) and (x', y', z'), respectively. The mathematical definition in the case of $M = 1$ is given as,

$$\begin{pmatrix} x' \\ y' \\ z' \end{pmatrix} = \begin{pmatrix} B_1 & B_4 & B_7 \\ B_2 & B_5 & B_8 \\ B_3 & B_6 & B_9 \end{pmatrix} \begin{pmatrix} x \\ y \\ z \end{pmatrix} + \begin{pmatrix} X_0 \\ Y_0 \\ Z_0 \end{pmatrix} \tag{20}$$

where $X_0, Y_0,$ and Z_0 represent the x, y, and z origin point.

The translation section is used to ensure the tumor is precisely located at the (0, 0, 100) isocenter, in line with the beam and at the 100 cm source-to-axis distance (SAD) to match the experimental setup. The rotation section is then applied to simulate the various treatment gantry angles. It is important to note that this simulation methodology rotates the phantom itself relative to a fixed beam source. This is the inverse of the physical experiment, where the LINAC gantry rotates around a stationary phantom. This is a standard and valid simulation technique, as it perfectly preserves the relative geometry between the beam source and the target. The critical 100 cm SAD is maintained in either reference frame, ensuring the simulation accurately replicates the treatment fields. The specific transform values for the phantoms are found in Table 3.2 and Table 3.3. Due to the ATP being imported from an external source and representing only a fraction of the full body, its translation values differ from the ICRP phantoms to achieve the same tumor-at-isocenter alignment.

Table 3.2: ICRP Phantom Transforms with Gantry Angles

Beam Setup		**Translation (cm)**			**Rotation Matrix Components**									**Mode**
n	**Gantry Angle**	X_0	Y_0	Z_0	B_1	B_2	B_3	B_4	B_5	B_6	B_7	B_8	B_9	***M***
1	0°	9.75	45	98.76953	0	90	270	90	90	0	90	180	90	1
2	90°	-1.23047	45	90.25	90	90	180	0	90	90	90	180	90	1
3	180°	-9.75	45	101.23047	180	90	90	90	90	180	90	180	90	1
4	270°	1.23047	45	109.75	270	90	0	180	90	270	90	180	90	1

Table 3.3: ATP Phantom Transforms with Gantry Angles

Beam Setup		**Translation (cm)**			**Rotation Matrix Components**									**Mode**
n	**Gantry Angle**	X_0	Y_0	Z_0	B_1	B_2	B_3	B_4	B_5	B_6	B_7	B_8	B_9	***M***
1	0°	9.75	-14.9	120.35	0	90	270	90	90	0	90	180	90	1
2	90°	20.35	-14.9	90.25	90	90	180	0	90	90	90	180	90	1
3	180°	-9.75	-14.9	79.65	180	90	90	90	90	180	90	180	90	1
4	270°	-20.35	-14.9	109.75	270	90	0	180	90	270	90	180	90	1

To have the correct field size for each beam location, the MLC is moved to specific locations. As seen in Table 2.1, the field size stays consistent at 6.0 x 6.0 cm. To open the collimator to this location in PHITS, the transform section was used. The degree to which the MLC was opened was calculated from equations 3.1 and 3.2. The results of the 6 x 6 cm

Table 3.4: X and Y Jaw Movements for a 6 x 6 Field

Beam Setup	**Translation (cm)**			**Rotation Matrix Components**									**Mode**
$\boldsymbol{n}$	X_0	Y_0	Z_0	B_1	B_2	B_3	B_4	B_5	B_6	B_7	B_8	B_9	$\boldsymbol{M}$
1	0	0	0	0	90	90	90	1.718358	88.28164	90	91.71836	1.718358	1
2	0	0	0	0	90	90	90	1.718358	91.71836	90	88.28164	1.718358	1
3	0	0	0	1.718358	90	88.28164	90	0	90	91.71836	90	1.718358	1
4	0	0	0	1.718358	90	91.71836	90	0	90	88.28164	90	1.718358	1

field transform is seen in table 3.4. The physical position of each MLC leaf in the simulation was calculated using the principle of similar triangles. This method projects the desired field edge x at the isocenter (100 cm SAD), as defined in Appendix A, back to the physical plane of the MLC. Given the 50.3 cm source-to-MLC distance, the required leaf position, x_{leaf}, was calculated for each field using the relationship shown in Equation (3.5):

$$x_{\text{leaf}} = x \times \left(\frac{50.3 \text{ cm}}{100 \text{ cm}} \right). \tag{3.5}$$

3.2 Simulated and Experimental Results

With the completion of the experimental measurements and the corresponding ATP simulations, the first objective is achieved in validating the computational model with experimentation. The resulting data and a detailed discussion of these findings are presented in the following two sections.

3.2.1 PHITS-Simulated ATP Model and Particle Tracks

The geometry of the ATP, including the medical LINAC, was modeled in PHITS as shown in Figure 3.7. This model was used to calculate the dose at the TLD locations for direct comparison with the experiment. To visualize the radiation dose through the validated ATP model, a heat map of the dose distribution was generated in Figure 3.8. This figure demonstrates the dose distribution across the four-field treatment plan, showing the high-dose region localized within the target volume and the subsequent dose attenuation as the gradient transitions into the surrounding lung and tissue. As the beam passes into the lung,

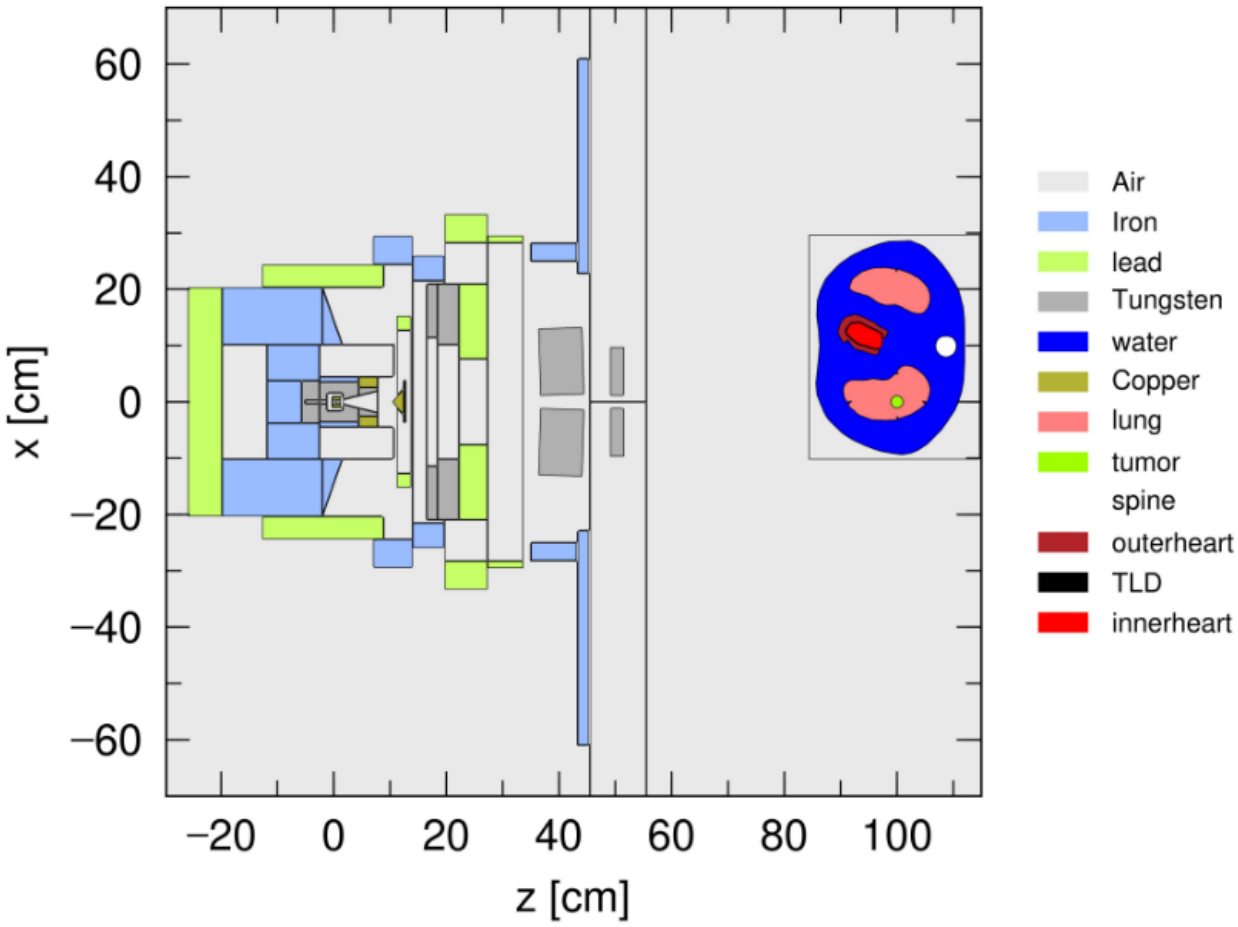

Figure 3.7: The computational geometry of the ATP track for field 1, used for simulating TLD dose

the dose decreases; this is a result of secondary electron transport within the low-density lung tissue. In this environment, electrons travel further away from the primary beam, which reduces the localized absorbed dose. This Monte Carlo-modeled dose decrease at the interface between tissue (water) and lung is consistent with previous findings in literature. Specifically, with fine field sizes, the dose exhibits a significant 'dip' upon entering the lung region due to the increased secondary electron range in low-density media[48]. Once the beam reaches the tumor, the more interaction sites cause the dose to increase as energy is deposited more effectively within the mass.

To ensure the reliability of the computational results, the statistical uncertainty of the Monte Carlo simulations was carefully controlled. By simulating a sufficient number of pri-

mary particle histories in PHITS, the target statistical uncertainty for all dose calculations within the primary regions of interest, specifically the TLD locations and the Planning Target Volume (PTV), was less than 5%. This level of precision ensures that observed discrepancies between simulated results and experimental TLD measurements exceed the margin of computational noise, representing genuine dosimetric differences at a 95% confidence level.

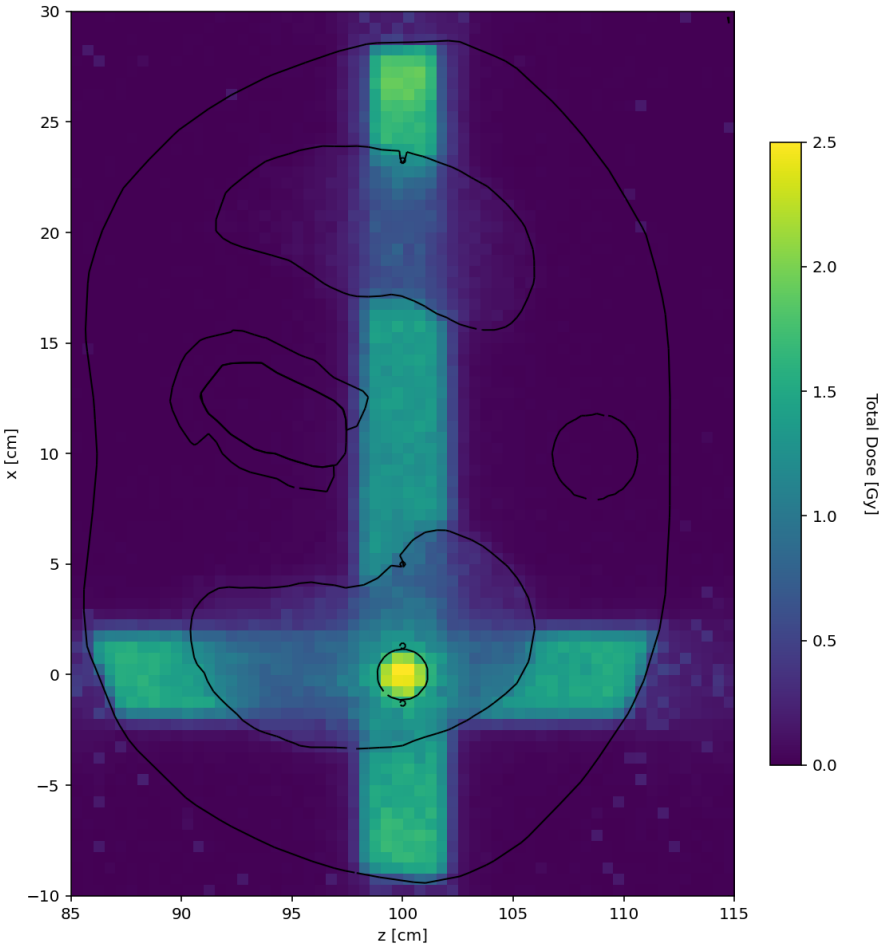

Figure 3.8: Dose distribution in the ATP four field simulation

3.2.2 Experimental Results and Simulation Validation

After irradiation, TLDs were read using the Harshaw TLD reader 2 hours post-treatment. The resulting TLD values represent the cumulative absorbed dose from all four fields, corresponding to a planned total tumor dose of 2 Gy.

These experimental measurements were used to validate the calculated Varian Eclipse AAA values and the PHITS ATP simulation. Figure 3.9 plots the experimentally measured TLD dose against the dose calculated at the same discrete points in the PHITS simulation and the AAA calculated values. Table 3.5 indexed each ID number to their respective organ or dosimeter location. A discussion of the plotted results is found in Section 3.3.

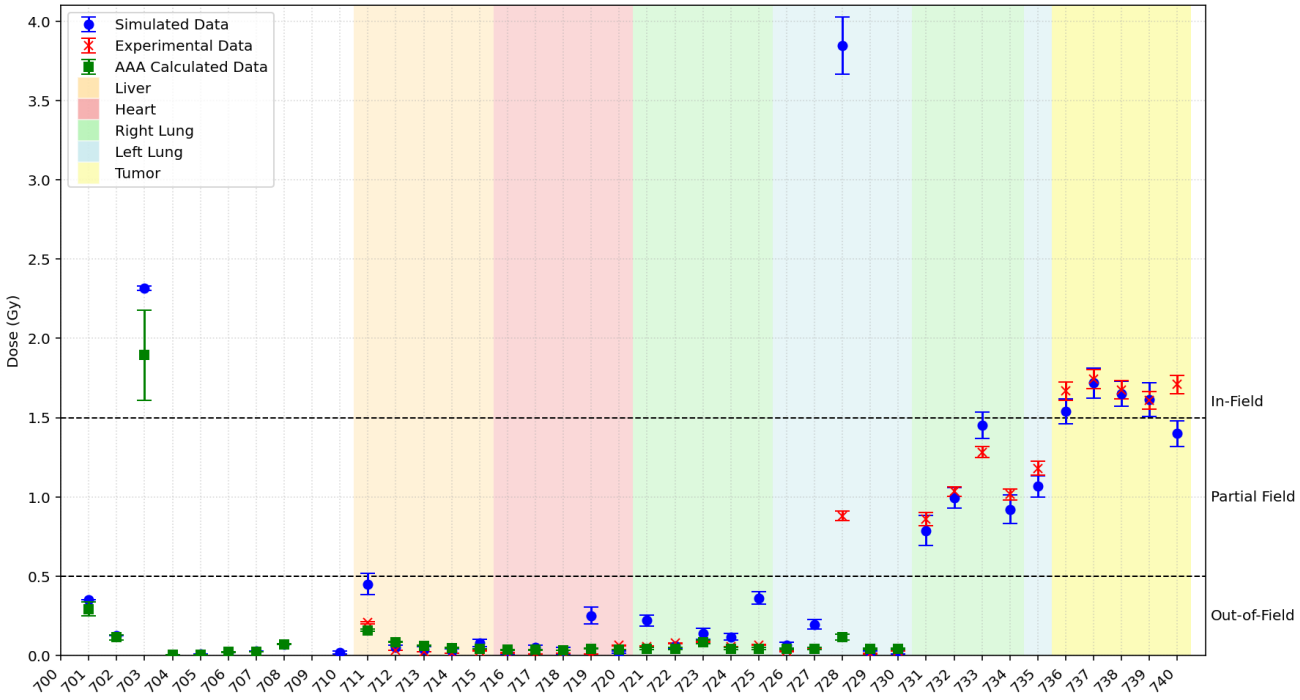

Figure 3.9: Comparison of experimentally measured dose from TLDs versus the simulated dose calculated at the same points in the ATP model.

The total experimental uncertainty for the TLD measurements was calculated by combining the dominant Type A (statistical) and Type B (systematic) uncertainties in quadrature. The overall combined uncertainty for this experiment was determined to be 3.5 %.

This value was calculated by propagating the three primary sources of uncertainty identified during the analysis:

- **TLD-100H Repeatability:** The statistical uncertainty from the TLDs' own repeatability, estimated at 2 %.
- **Detector Sensitivity:** The uncertainty stemming from the inhomogeneity of the Harshaw 5800 detector's sensitivity, estimated at 2 %.

- **Beam Calibration:** The systematic uncertainty from the beam calibration, estimated at 2 %.

Table 3.5: Mapping of ID Numbers to Anatomical Locations and Placement

ID Number	Location / Classification
701	Right Lung
702	Left Lung
703	Tumor
704	Spine
705	Liver
706	Inner Heart
707	Outer Heart
708	Body
710	Marker
711–730	Distributed Dosimeters
731–740	Targeted Dosimeters

Note: ID numbers include both anatomical markers and dosimeter locations. Distributed dosimeters were randomly placed for out-of-field characterization, while targeted dosimeters were strategically positioned in high-dose areas.

Other potential uncertainty sources, such as photonic linearity, energy dependence, and signal fading, were determined to be negligible. This was due to the use of a localized 6 MV calibration, operation within a confirmed linear range (1 mGy to 10 Gy), and a consistent, timed readout process.

The total combined uncertainty ($k = 1$) was calculated as the root-sum-square (RSS) of these three main contributions:

$$U_c = \sqrt{(0.02)^2 + (0.02)^2 + (0.02)^2} \approx 0.035$$

This results in a final experimental uncertainty of 3.5 %, which was applied to all experimental data.

The magnitude of the AAA error fluctuates depending on the density and composition of the medium through which the beam passes. In regions of relative homogeneity or water-

equivalent density, such as the heart, the AAA maintains high accuracy with discrepancies often limited to approximately 3%[24]. However, as the beam traverses more complex, low-density regions like the lungs, the reliability of the analytical scaling decreases. In these "questionable" areas, the all-encompassing error has been observed to increase to as much as 15%, a deviation primarily driven by the algorithm's simplified handling of electron transport[49].

The uncertainty inherent in the AAA method is categorized as systematic, stemming from the deterministic nature of its mathematical approximations. Because AAA uses pre-calculated kernels and density-scaling to predict dose, its errors are reproducible and built-in to the algorithm whenever it encounters heterogeneous interfaces. In contrast, the Monte Carlo simulations involve both stochastic and systematic uncertainties. The stochastic component is random, arising from the statistical nature of sampling individual particle histories. Meanwhile, the systematic uncertainty in Monte Carlo is tied to the phantom geometry and the accuracy of the underlying cross-sectional data. Thus, while Monte Carlo errors can be reduced by increasing the number of simulated particles to improve precision, the AAA error represents a fundamental limitation in accuracy when modeling heterogeneous material.

To determine the total absorbed dose from a composite radiation treatment plan, raw dose data from four independent PHITS field simulations (e.g., Field 1 through Field 4) were combined and normalized. Each simulation initially generated an output in units of Gy/source, which was subsequently scaled by field-specific multiplication factors derived from the source particle counts and MU to convert the values into a clinically relevant dose. The internal statistical error for each independent PHITS calculation was determined within the code by dividing the total simulation into multiple batches, defined by the maxcas and maxbch parameters, and analyzing the variance of the tally results. To ensure a statistically reliable estimation of this uncertainty, it is recommended to simulate at least 10 batches so that the error decreases proportionally to the square root of the total histories. Because these four field simulations are statistically independent, the cumulative uncertainty was calculated using the Root-Sum-Square (RSS) method. This approach ensures that the total absolute error, representing the standard deviation of the combined dose, is accurately

reported without the overestimation that would result from a simple linear summation of uncertainties.

3.2.3 TLD Experimental vs PHITS-Simulated

To validate the accuracy of the PHITS simulation against experimental results minimizing positional uncertainty, TLDs were strategically positioned within the ATP. These dosimeters were aligned specifically within the beam paths to ensure a direct comparison between the measured and simulated dose distributions.

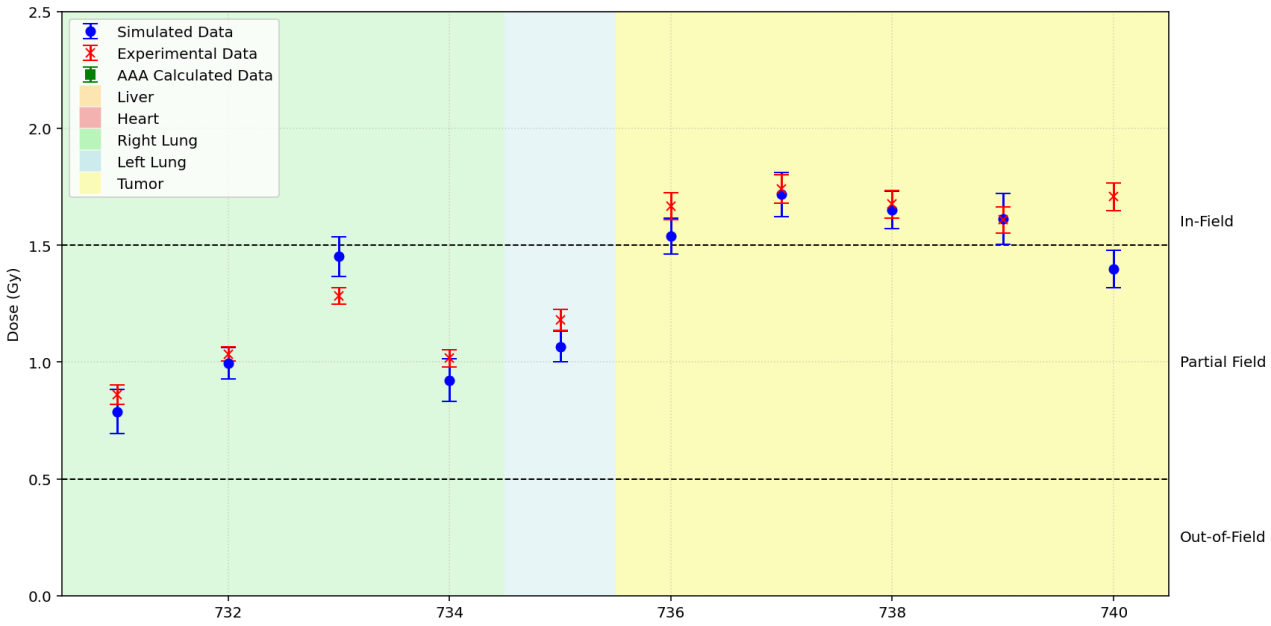

Figure 3.10: Measured dose from TLDs compared against simulated dose values at corresponding coordinates within the ATP model for selected TLD locations.

3.2.4 Organ Doses from PHITS Simulation and AAA Calculation

Following the successful validation against TLD measurements, the ATP simulation was used to calculate the mean absorbed dose for the primary organs. These values, presented in Table 3.6, show the relative error between the PHITS simulated ATP dose and the AAA calculated dose.

Table 3.6: Mean organ doses (Gy) comparing PHITS Monte Carlo simulation (ATP) with Varian Eclipse (AAA) calculation for the Anthropomorphic Torso Phantom with standard error (SE) with precision reflecting the output of each respective calculation method.

Organ	ATP Dose (SE)	AAA Dose (SE)	Rel Error
PTV	2.3180 (0.0143)	1.89 (0.28)	18.3%
Right Lung	0.35075 (0.00103)	0.294 (0.044)	16.2%
Left Lung	0.12398 (0.00067)	0.114 (0.017)	8.05%
Heart	0.047269 (0.0003)	0.046 (0.001)	2.68%
Liver	0.0096765 (3.49e-5)	0.006 (0.003)	38.0%
Spine	0.0068495 (5.35e-5)	0.006 (0.003)	12.4%
Body	0.069310 (4.0e-5)	0.072 (0.002)	-3.88%

3.3 Correlation Between Experimental Measurements and Simulations of ATP

3.3.1 Simulated AAA vs Monte Carlo

The observed discrepancies between the AAA-calculated dose in Varian Eclipse and the PHITS Monte Carlo simulation (seen in section 3.2.2, Figure 3.9) stem from inherent limitations within the AAA model. As described in Section 1.2, the AAA was the primary model available for this research, despite its known inaccuracies in heterogeneous environments.

This discrepancy is most pronounced within the gross tumor volume (GTV). The significant difference between the AAA result and the simulated dose can be attributed to the drastic density fluctuations encountered across the four fields of the treatment plan. Each beam follows a "tissue–lung–tumor–lung–tissue" density rotation. In such a setup, multiple physics failures arise within the AAA model. In the low-density polystyrene medium, secondary electrons travel much farther laterally than in water-equivalent tissue. Because the dense tumor is essentially an "island" surrounded by this low-density lung-equivalent medium in the AAA calculation model, high-energy electrons scatter out of the tumor and are not replaced by a sufficient amount of back-scatter from the surrounding air and polystyrene.

These failures are documented in independent physics literature. For instance, the Gamma Agreement Index (GAI) serves as a point-by-point comparison between a treat-

ment plan dose map and a Monte Carlo reference. In "light lung" materials with densities lower than 0.035 g/cm^3—similar to the polystyrene used here—the GAI for AAA has been reported as low as 6.3% for small 6MV fields. This indicates that over 93% of the dose voxels in a volume like the GTV failed to match the Monte Carlo truth within a standard 3%/3mm tolerance[50]. Other studies have confirmed similar systematic underdosing of the target volume, identifying discrepancies of 13% or greater when comparing AAA to AXB or Monte Carlo methods in small, heterogeneous lung targets[49;51]. These published findings reinforce the conclusion that the 18.3% underestimation observed in this study is a result of the AAA's inability to model electron transport in extreme heterogeneity.

3.3.2 Experimental vs Monte Carlo

The observed discrepancies between the experimental dosimeter measurements and the PHITS simulated dose distributions, detailed in Figure 3.9 and Table 3.6, are categorized by the positional uncertainties affecting the localized dosimeter readings.

These discrepancies, particularly those concerning the individual dosimeter readings in regions 711-740, are fundamentally driven by cumulative positional uncertainty. This issue is magnified by the high-definition beam delivered by the LINAC, which creates extremely steep dose gradients at the field edges. Consequently, even a small shift in a dosimeter's position can move it from a high-dose region to a low-dose region, causing a large difference between the measured and simulated values. Consider figure 2.11, in-target results in the largest dose because it is the convergence of all 4 beams. Partially in target still gives a significant dose because it is in line with the beam. However, once you move out into the out of target region, there is a steep dose fall off. The errors originate from two distinct phases: experimental setup and computational modeling.

The first major source of error is the Experimental Setup Error, or physical shift. This arises from the protocol of manually substituting initial BB markers—used for CT imaging—with the actual small dosimeters for the treatment delivery. This substitution introduces unavoidable human error and setup variability. Given the sharp beam field, a shift

of just a few millimeters out of target, let alone the potential 2 cm margin mentioned, can drastically alter the dose recorded by the dosimeter. This vulnerability is highly pronounced for dosimeters in non-rigid structures, such as the one in Region 728, which was located in the flexible TPU bronchial tree. This flexibility allows the dosimeter to be easily displaced, moving it from the simulated position directly in line with the beam to an actual position on the outskirts of the beam during the experiment, thus accounting for the observed large dose drop.

The second major source is Computational Modeling and Translation Error. This error is inherent in the multi-step process of converting the physical CT image into the digital geometry required by PHITS (Section 3.1.3). The process involves segmentation, exporting to STL, smoothing, and meshing. Each conversion and interpolation step introduces an element of error, slightly misrepresenting the boundaries and position of the digital structures. Because the dosimeters are small (millimeter-scale), this small margin of error in the model's geometry translates into a significant relative positional error for the dosimeter's sensitive volume within the simulation. Therefore, the calculated dose is based on a simulated dosimeter position that is slightly displaced from the true physical location, contributing to the final dose discrepancy.

The effect of these cumulative errors is most clearly demonstrated by Dosimeter 728, which was placed within the flexible bronchial tree inside the left lung. This location combines two critical factors that maximize the impact of positional uncertainty. First, the bronchial trees in the Anthropomorphic Training Phantom (ATP) are made of flexible TPU material and can be easily moved or deformed by common handling during the setup process, significantly magnifying the human setup error (physical shift). Secondly, the dosimeter's location was out of target with the transverse beams during experimentation, positioning it on the high-dose plateau of the treatment field in the simulation. However, the physical shift from the experimental setup, compounded by the computational error in the model's geometric representation, caused the dosimeter to be effectively moved partially in target for simulation. This translational shift pushed the sensitive volume into the steep-falling penumbra region.

The large observed discrepancy for region 728 is a direct result of this shift in a high-gradient environment. A small displacement in a region where the dose changes rapidly leads to a massive difference between the high dose intended by the ideal simulation and the much lower dose actually measured experimentally. This case study confirms that for high-precision radiation delivery, the cumulative positional uncertainty arising from both manual setup and modeling inaccuracies is the dominant cause for localized measurement errors.

The Experimental vs PHITS simulation in section 3.2.3 demonstrates the strong agreement between the experimental and simulation data in figure 3.10 with the highest error being around 15% for dosimeter 740 and the average of the rest are within 5%. Because these specific dosimeters were strategically placed partially in target, the probability for human setup and computational conversion error is low. This strong agreement implies that the simulated experiment matches up with the measured values.

Chapter 4

Comparative Analysis of Voxel and Mesh-Type ICRP Phantoms

4.1 ICRP Phantom Comparison

With the benchmark doses established, the ICRP voxel and mesh phantoms were incorporated into the validated simulation environment to assess their geometric and dosimetric accuracy. These next sections address the remaining research goals: assessing the ICRP models against the validated ATP benchmark and performing a direct comparison between the ICRP voxel and mesh phantoms.

4.1.1 ICRP Reference Phantom Models

This research focuses on two sets of ICRP computational phantoms: the voxel-based phantom from ICRP Publication 110 and the mesh-based phantom from ICRP Publication 145. The voxel-based phantom is composed of rectangular parallelepipeds creating block anatomy decreasing the resolution of the phantom. To model the intricate human anatomy, the mesh-based phantom utilizes tetrahedrons where complex shapes may be modeled. Visualizations of a diagonal cut of both phantoms can be seen in Figure 4.1, where the voxel phantom is shown on the left and the mesh phantom is on the right. The bright green circle in both

images is the representative tumor that is used for this research. The tumor was placed within the computational phantoms based on its coordinates in the ATP. For the lateral (left-right) and anteroposterior dimensions, CT measurements provided exact offsets from the isocenter. However, because the ATP is a segmented representation of the human body, the superior-inferior (top-to-bottom) position was established through anatomical landmarks within the voxel phantom and replicated in the mesh phantom to maintain consistency.

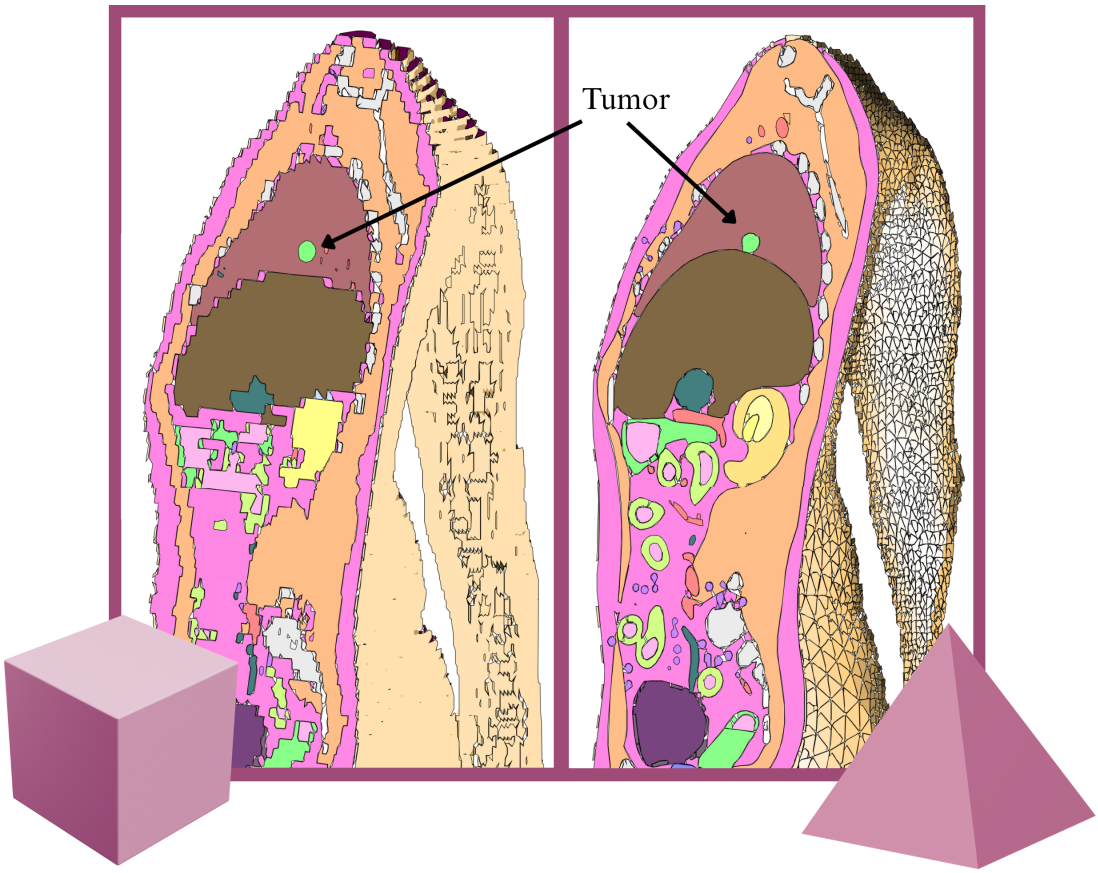

Figure 4.1: 3D cross-section of voxel made of rectangular parallelepipeds (left) and mesh made of tetrahedrons (right) ICRP computational phantoms

The sample input files for these phantoms in PHITS were developed under the supervision of Dr. Akira Endo of JAEA (voxel) and Dr. Chan Hyeong Kim with Mr. Bangho Shin of Hanyang University (mesh), and they are distributed with ICRP's approval.[14] The voxel phantom uses a lattice structure where each organ is a separate "universe," and the entire body is enclosed within a single bounding box. This design greatly simplifies geometric manipulations. For example, moving or rotating the body only requires transforming this

single box. This approach is powerful when used with the PHITS NOT operator (#) for modeling foreign objects within the phantom. To exclude the phantom from a larger volume (like a room filled with air), one only needs to subtract the box. Conversely, to add a new object inside the body, its shape is simply subtracted from the box's cell definition, avoiding the complex task of modifying every organ it intersects. The mesh phantom uses a similar container-box method, which also allows the entire body to be easily excluded. The only difference is the cell numbering and the non lattice format. PHITS uses interconnected tetrahedral elements to create the structure of the mesh.

4.1.2 Geometric Accuracy and Computational Performance

When observing the two computational phantoms in Figure 4.2, it is clear that the voxel phantom (left) does not provide the anatomical accuracy of the mesh phantom (right). This is specifically seen with the kidneys, where the voxel kidney does not distinguish between the cortex, pelvis, and medulla. The higher resolution of the mesh phantom makes it an optimal phantom to utilize when calculating dose to complex anatomical structures or anatomy provided in the mesh that is not in the voxel, such as the multiple components of the kidney.

This difference in geometric detail is also evident in the phantom cross-section, as shown in Figure 4.3. The curvatures in the voxel phantom (left) are defined by the rigid, block-like geometry, while the mesh phantom (right) contains smoothly-curved, higher-fidelity organ boundaries.

Both phantoms have a certain complexity affecting the computational time. Due to the mesh phantom anatomical complexity and resolution, the increased computational weight extends simulation runtimes compared to traditional voxel-based models. When simulating the phantoms within PHITS using the LINAC model, the computational time per batch is approximately 3% greater for the mesh phantom than for the voxel phantom; however, this discrepancy accounts only for dose calculations in specific regions of interest. Generating a full-field visualization for the mesh phantom would incur a significantly higher computational penalty due to its intricate geometries.

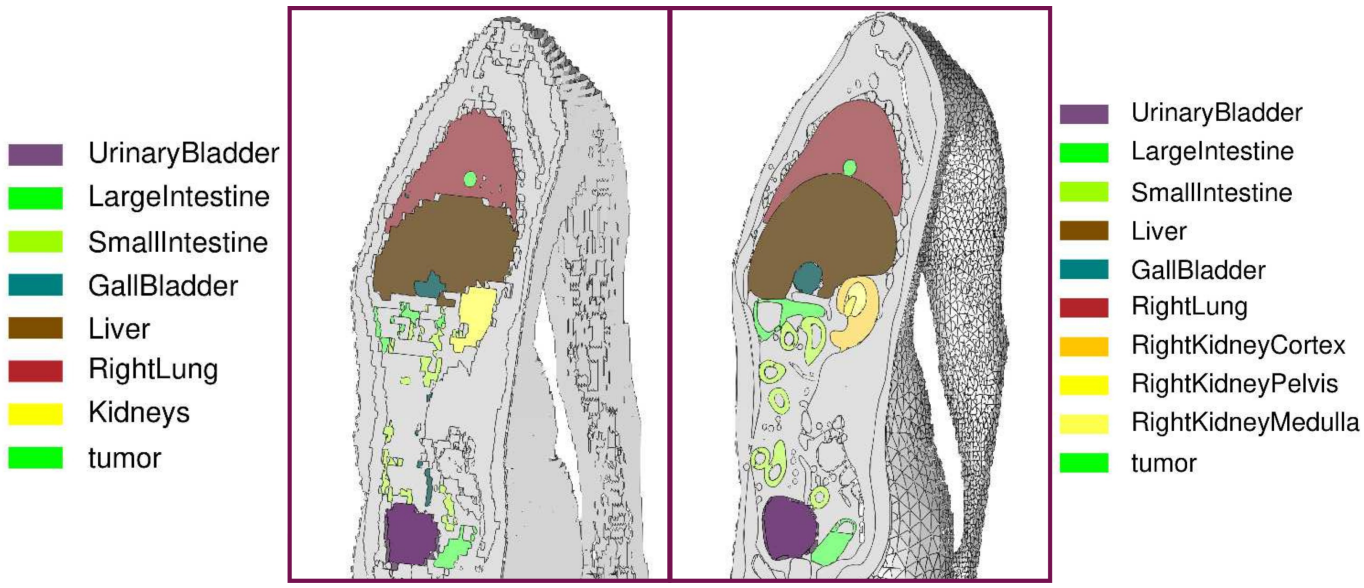

Figure 4.2: Side-by-side comparison of the ICRP voxel phantom (left) and ICRP mesh phantom (right) within the PHITS environment.

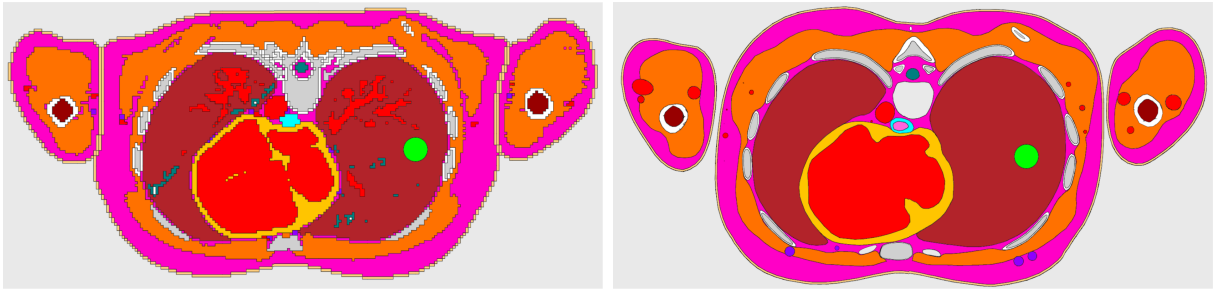

Figure 4.3: Representative cross-sections for the ICRP voxel phantom (left) and the ICRP mesh phantom (right).

To formalize this analysis, the Figure of Merit (FOM) was calculated. The FOM, defined as $1/(\epsilon^2 T)$ where ϵ is the relative error and T is the computation time, assesses the efficiency for a given statistical uncertainty. As described in table 4.1, the voxel phantom achieved a FOM of 0.87 min^{-1}, while the mesh phantom's FOM was 0.85 min^{-1}. This indicates that the voxel phantom is more computationally efficient for achieving a simple dose estimate, but the mesh phantom is only a difference of 0.02 min^{-1}. However, this metric only accounts for the calculation phase.

A significant gap exists in the initialization overhead: the file read time for the mesh phantom is nearly five times that of the voxel phantom. Furthermore, while the FOMs are

similar for integral quantities (organ dose), the geometric complexity of the mesh phantom implies that for tasks requiring high-resolution field visualization, the mesh FOM would likely decrease significantly compared to the voxel model.

Finally, the data reveals a substantial drop in efficiency for the ATP model compared to both the voxel and mesh phantoms. This is driven by a high relative error (ϵ) stemming from mesh quality rather than geometry type. Although the ICRP mesh phantom also utilizes tetrahedral geometry, it has been rigorously optimized. In contrast, the ATP model relies on an automated STL-to-mesh conversion (via Gmsh), which can generate low-quality elements. These "sliver" tetrahedra—often needle-shaped or pancake-shaped—result in high variance in particle track lengths, directly inflating the statistical error and reducing the overall FOM.

Table 4.1: Comparison of computational performance for the three phantom simulations on same Beocat node. The Figure of Merit (FOM) is calculated using the relative error (R) within the tumor and the steady-state time for 10 batches of 1 million particles (T = Batch Time $\times$ 10), where T is in minutes.

Simulation	**Relative Error (R)**	**Read Time (min)**	**Avg. Batch Time (min)**	**FOM (min^{-1})**
Voxel Phantom	0.1333	2.00	6.47	0.87
Mesh Phantom	0.1328	9.68	6.65	0.85
ATP	0.1830	0.65	6.32	0.47

4.1.3 Comparison of Simulated Organ Doses with Male Phantoms

The primary goal was to compare the dosimetric accuracy of the phantoms. Table 4.2 presents the mean absorbed dose for key organs calculated in all three models: the PHITS simulated ATP, the ICRP voxel phantom, and the ICRP mesh phantom. The ATP serves as the benchmark for this research because it was the physical phantom used during the experimental phase. The ICRP voxel and mesh simulations are compared against the ATP results to determine which computational model best replicates the measured experimental data. It is important to note a key difference in this comparison: the ATP is a partial-body (torso) phantom, while the ICRP phantoms are whole-body models. However, given that the treatment plan utilized a highly collimated beam directed only at the torso, it is assumed that any resulting scatter dose to regions outside the torso (such as the head, arms, or lower

legs) is negligible. Therefore, the dose calculated for the torso organs within the ICRP phantoms is considered representative of the total organ dose and can be validly compared to the benchmark ATP results.

Table 4.2: Mean Organ Doses (Gy) of Male ICRP phantoms given to 3 significant figures with Standard Error (SE) in parentheses and Relative Error (%) compared to the PHITS simulated ATP. Voxel doses for Lungs (tissue and blood), Heart (wall and contents), and Spine (thoracic spongiosa and cortical) are mass-weight-averaged. Mesh doses for the Spine are similarly mass-weight-averaged across thoracic components.

Organ / Structure	**ATP**	**ICRP Male Voxel**		**ICRP Male Mesh**	
	Dose (SE)	**Dose (SE)**	**Rel Err**	**Dose (SE)**	**Rel Err**
PTV (Tumor)	2.32 (0.01)	2.35 (0.02)	1.48%	2.38 (0.02)	2.61%
Right Lung	0.351 (0.001)	0.275 (0.001)	-21.5%	0.274 (0.001)	-22.0%
Left Lung	0.124 (0.001)	0.0772 (0.0004)	-37.8%	0.0852 (0.0005)	-31.3%
Heart	0.0473 (0.0002)	0.246 (0.001)	421%	0.250 (0.001)	428%
Liver	0.00968 (3.5e-5)	0.0223 (1.2e-4)	130%	0.0434 (1.7e-4)	348%
Thoracic Spine	0.00685 (5.4e-5)	0.0116 (1.2e-4)	71.0%	0.0110 (1.1e-4)	60.2%

Both the voxel and mesh phantom contain a tumor dose within 3% of the torso phantom providing excellent agreement. Proving that the mesh and voxel are both reliable phantoms for high precision LINAC treatment. The heart and liver bring about the most drastic difference from the ATP simulation. Not only does this discrepancy arise from natural scatter to out of field organs being much lower adding errors, but also the high difference in geometric complexity. The shape and location of the liver and heart is different for each phantom. In particular, the ATP and Voxel liver have similar gaps from the liver to the in-field location, but the mesh phantom's liver crosses in line with the beam and therefore increases the dose to the liver. Both the voxel and mesh phantoms overestimated the tumor, heart, liver, and spine, and underestimated the lungs.

4.1.4 Comparison of Simulated Organ Doses with Female Phantoms

While the previous sections focused on standard male reference models, the ATP serves as a representative average-to-large anatomy suitable for comparison across both sexes. To

evaluate the dosimetric consistency for female representations, Table 4.3 presents the mean absorbed doses and relative errors for the ICRP female mesh phantom relative to the PHITS-simulated ATP. Given that the male voxel and mesh phantoms demonstrated similar FOM, the female mesh phantom was prioritized for simulation to leverage its improved anatomical accuracy for this comparison.

Table 4.3: Mean Organ Doses (Gy) of ICRP Female Mesh given to 3 significant figures with Standard Error (SE) in parentheses and Relative Error (%) compared to the PHITS simulated ATP. Mesh doses for the Spine are mass-weight-averaged across thoracic components.

Organ / Structure	**ATP**	**ICRP Female Mesh**	
	Dose (SE)	**Dose (SE)**	**Rel Err**
PTV (Tumor)	2.32 (0.01)	2.55 (0.02)	9.79%
Right Lung	0.351 (0.001)	0.299 (0.001)	-14.7%
Left Lung	0.124 (0.001)	0.105 (0.001)	-15.2%
Heart	0.0473 (0.0002)	0.311 (0.001)	557%
Liver	0.00968 (3.5e-5)	0.0104 (6.7e-5)	7.39%
Thoracic Spine	0.00685 (5.4e-5)	0.0119 (1.2e-4)	74.2%

While the ICRP Male Mesh phantom maintains the tumor dose within 3% (as shown in Table 4.2), the female tumor dose shows a larger discrepancy of approximately 10%. This is likely due to the significant size difference between the two reference phantoms; while the ATP is designed to represent an average-to-large male or female, its dimensions align more closely with the larger male models. Consequently, the smaller female phantom receives a higher dose to the target volume. Conversely, the right and left lungs show a lower discrepancy than seen in the male comparison, suggesting that the smaller volumes and shapes of the female lungs are a better match for the ATP's anatomy. The most notable improvement is the Liver dose, where the discrepancy is minimal because the organ remains almost entirely out of the primary field in the female mesh, mirroring the positioning in the ATP.

4.1.5 ICRP Male Phantom Dose Comparison (Voxel vs. Mesh)

Beyond comparing to the benchmark, a key advantage of the mesh phantom is its ability to model fine anatomical structures that are not defined in the voxel phantom. To investigate the dosimetric impact of this higher fidelity, Table 4.4 provides a direct comparison of mean absorbed doses between the ICRP voxel and mesh phantoms with a threshold cutoff of 0.02 Gy to highlight significant region dose.

This analysis highlights the dose discrepancies that arise from the different anatomical representations. For example, the voxel phantom provides a single average dose for the entire bronchi, whereas the mesh phantom can resolve the dose difference between different layers of the bronchi and calculate the dose at certain sensitive regions such as the secretory or basal cells. For this reason, single voxel values are compared against multiple mesh values for different sensitive regions seen in the bronchi, oesophagus wall, and the skin on arms. Organs such as the lungs are separated out into two parts in the voxel (tissue and blood), as opposed to the total singular dose in the mesh. Therefore, the tissue, blood, and mass-weighted-average of the lungs are compared against the singular mesh value.

4.1.6 ICRP Mesh Male and Female Phantom Dose Comparison

While the previous section examined the differences between voxel and mesh representations, it is equally critical to consider sexual differences in radiation dosimetry. The ICRP mesh phantoms provide sex-specific anatomical models, the dose quantities for which are summarized in Table 4.5. This comparison utilizes the same 0.02 Gy dose threshold as the previous analysis and focuses on the subset of organs highlighted in Table 4.4. By evaluating these identical structures across both the male and female mesh phantoms, the specific impact of sex-dependent anatomical variations on mean organ dose can be evaluated.

4.2 Significance of ICRP Phantom Discrepancies

The transition from ICRP Publication 110 to ICRP Publication 145 was primarily driven by the need to resolve dose in thin, sensitive tissue layers that are critical for radiation protection but too small for a standard voxel grid. In this study, the Bronchi (BB1), Oesophagus Wall, and Skin comparisons utilize the specific sensitive depth layers defined in the Mesh phantom as the point of comparison for the Voxel's whole-organ averages.

For the Bronchi, ICRP Publication 110 reports a single average dose across the entire bronchial wall. In contrast, ICRP Publication 145 differentiates between the sensitive basal and secretory nuclei at specific micron-level depths. The data shows that the voxel model significantly overestimates the dose to these regions (approx. 80%), whereas the Mesh model accurately depicts the attenuation of dose through the physical layers of the bronchi. Similarly, the Oesophagus Wall shows a 14.3% discrepancy. ICRP 145 notes that the "stair-step" artifacts of 2–8 mm voxels can artificially inflate or deflate doses in thin-walled structures. The smooth mesh surfaces provide a more physically accurate boundary, allowing for a precise tally at the sensitive mucosal layer rather than a volume-averaged approximation.

Regarding the Skin, the ICRP 110 model averages the dose over a 2 mm thickness, which includes significant amounts of non-sensitive dermal tissue. By specifically targeting the basal layer at the nominal 50 μm depth, ICRP 145 provides a more accurate estimate of the equivalent dose required for skin cancer risk assessment. Generally, the Voxel model tends to misrepresent dose in these small surface regions because it lacks the geometric smoothing required to model the interface between tissue and air or surrounding structures accurately.

For large, non-surface organs, the discrepancy between the two phantoms is significantly reduced when correct mass-weighting is applied. In the Lungs, the Mesh phantom integrates tissue and blood into a single Alveolar-Interstitial (AI) region to better represent gas-exchange areas. The mass-weighted average for the Right Lung shows a near-perfect match (-0.6%), proving that the two phantoms are physically equivalent for large-organ dosimetry when separate Voxel components (blood and tissue) are combined correctly.

However, the Left Lung exhibits a much larger discrepancy, driven primarily by an 81%

difference in the blood content comparison. The left lung is inherently more sensitive to voxelization artifacts due to its proximity to the heart. While the right lung has a relatively simple geometry with three lobes and broad boundaries, the left lung is smaller, has only two lobes, and contains the complex cardiac notch. The smooth mesh representation of this notch significantly alters the volume and boundary of the lung blood compared to the jagged voxel representation, leading to the observed divergence.

The discrepancies observed in the skeletal and solid organs highlight the Mesh phantom's superior ability to resolve thin, high-density structures. For example, the Cortical ribs showed a -34.8% difference, reflecting the fact that thin cortical shells are often poorly resolved or "smeared" in a 2 mm voxel grid. ICRP 145 maintains the physical shell thickness, ensuring the dose gradient between bone and marrow is correctly captured.

The most extreme outlier in this study was the Liver (94.6%). This discrepancy suggests a significant geometrical shift or partial-volume effect within the field setup. As noted in ICRP 145, solid organs may show large differences if their smooth boundaries intersect with high-gradient dose areas differently than the voxelized boundaries. In this specific treatment, where the beam was focused on the right lung, the liver is located immediately below the target area. Visual inspection of the phantom alignment (Fig. 4.2) confirms that the liver extends higher toward the target tumor in the Mesh model than in the Voxel model. This anatomical shift accounts for the higher dose in the Mesh phantom, as more of the liver volume is placed directly in the path of the beam.

When comparing the ICRP Mesh male and female phantoms, the larger tumor dose discrepancy in the female is primarily due to the smaller stature. The reduced volume of surrounding tissue provides less beam attenuation before the radiation reaches the target. This results in a higher dose concentration within the primary field. Another significant discrepancy occurs in the breast tissue, where the female volume is considerably larger and extends further laterally into "low-dose" regions far from the target. Consequently, when the dose is averaged over this volume, the Mean Organ Dose for the female decreases significantly relative to the male, whose smaller, more localized breast tissue sits closer to the high-dose thoracic region.

Table 4.4: Direct Comparison of Mean Organ Doses (Gy) given to 5 significant figures Between Male ICRP Voxel and Mesh Phantoms with Standard Error (SE) in parentheses.

Organ / Structure	**Voxel (SE)**	**Mesh (SE)**	**Diff. (%)**
Tumor	2.3524 (0.0231)	2.3786 (0.0221)	1.11%
Bronchi (Voxel vs Mesh BB):			
BB1 $10 \sim 35\,\mu$m	1.2210E-01 (1.20E-03)	2.3252E-02 (4.14E-03)	-80.96%
BB1 $40 \sim 50\,\mu$m	1.2210E-01 (1.20E-03)	2.5657E-02 (4.70E-03)	-78.99%
Humeri upper medullary cavity	2.3659E-02 (6.46E-04)	3.1589E-02 (9.41E-04)	33.52%
Ribs:			
Ribs Cortical	1.1443E-01 (4.12E-04)	7.4554E-02 (3.28E-04)	-34.85%
Ribs Spongiosa	6.6194E-02 (3.77E-04)	8.3374E-02 (5.00E-04)	25.95%
Scapulae:			
Scapulae Cortical	3.6971E-02 (3.22E-04)	3.9828E-02 (3.47E-04)	7.73%
Scapulae Spongiosa	2.8117E-02 (2.36E-04)	3.6587E-02 (3.73E-04)	30.12%
Breast Right:			
Adipose Tissue	8.2804E-01 (7.70E-03)	6.1374E-01 (6.69E-03)	-25.88%
Glandular Tissue	9.5147E-01 (1.14E-02)	7.5697E-01 (1.24E-02)	-20.44%
Heart:			
Heart Wall	1.8569E-01 (9.84E-04)	1.7016E-01 (9.36E-04)	-8.36%
Heart Contents (Blood)	2.8563E-01 (1.23E-03)	3.0972E-01 (1.24E-03)	8.43%
Mass-weighted average	2.4637E-01 (8.40E-04)	2.4961E-01 (8.12E-04)	1.32%
Liver	2.2276E-02 (1.16E-04)	4.3355E-02 (1.73E-04)	94.63%
Lungs:			
Left:			
Lung Blood (Voxel) vs Mesh	4.7017E-02 (8.46E-04)	8.5165E-02 (4.85E-04)	81.14%
Lung Tissue (Voxel) vs Mesh	8.2146E-02 (5.01E-04)	8.5165E-02 (4.85E-04)	3.68%
Mass-weighted average (Voxel) vs Mesh	7.7161E-02 (4.46E-04)	8.5165E-02 (4.85E-04)	10.37%
Right:			
Lung Blood (Voxel) vs Mesh	2.3588E-01 (1.77E-03)	2.7367E-01 (7.39E-04)	16.02%
Lung Tissue (Voxel) vs Mesh	2.8017E-01 (6.72E-04)	2.7367E-01 (7.39E-04)	-2.32%
Mass-weighted average (Voxel) vs Mesh	2.7531E-01 (6.29E-04)	2.7367E-01 (7.39E-04)	-0.59%
Lymphatic Nodes:			
Thoracic	4.5998E-02 (2.20E-03)	1.0088E-02 (6.48E-04)	-78.07%
Trunk	1.9376E-02 (4.11E-04)	2.4932E-02 (3.19E-04)	28.67%
Arm Muscle	2.3751E-02 (1.28E-04)	1.9364E-02 (8.91E-05)	-18.47%
Oesophagus Wall:			
Voxel vs Wall $190 \sim 200\,\mu$m	5.6795E-02 (1.15E-03)	4.8649E-02 (4.71E-03)	-14.34%
RST Arms	3.9820E-02 (1.95E-04)	4.6531E-02 (1.86E-04)	16.85%
Skin Arms:			
Sensitive $50 \sim 100\,\mu$m	2.9022E-02 (1.71E-04)	2.0779E-02 (3.43E-04)	-28.40%

Note: "Diff. (%)" is calculated as (Mesh - Voxel) / Voxel. A single Voxel structure corresponds to multiple Mesh sub-regions (e.g., Bronchi, Oesophagus, Skin), the Voxel mean dose is applied to each sensitive Mesh component for comparison.

Table 4.5: Direct Comparison of Mean Organ Doses (Gy) Between ICRP Mesh Male and Female Phantoms with Standard Error (SE) in parentheses.

Organ / Structure	**Male Mesh (SE)**	**Female Mesh (SE)**	**Diff. (%)**
Tumor	2.38E+00 (2.22E-02)	2.55E+00 (2.41E-02)	7.11%
Bronchi (BB):			
BB1 $10 \sim 35\,\mu$m	2.33E-02 (4.14E-03)	2.12E-02 (4.83E-03)	-8.86%
BB1 $40 \sim 50\,\mu$m	2.57E-02 (4.70E-03)	4.31E-02 (1.63E-02)	67.81%
Humeri upper medullary cavity	3.16E-02 (9.40E-04)	3.14E-02 (1.01E-03)	-0.47%
Ribs:			
Ribs Cortical	7.46E-02 (3.30E-04)	1.02E-01 (5.63E-04)	36.49%
Ribs Spongiosa	8.34E-02 (4.98E-04)	1.16E-01 (6.39E-04)	38.74%
Breast Right:			
Adipose Tissue	6.14E-01 (6.66E-03)	1.15E-01 (8.33E-04)	-81.32%
Glandular Tissue	7.57E-01 (1.24E-02)	4.70E-01 (2.94E-03)	-37.89%
Heart:			
Heart Wall	1.70E-01 (9.28E-04)	2.09E-01 (1.28E-03)	22.80%
Blood in Heart	3.10E-01 (1.25E-03)	3.91E-01 (1.89E-03)	26.14%
Liver	4.3355E-02 (1.73E-04)	1.0392E-02 (6.67E-05)	-76.03%
Lungs:			
Left Lung	8.52E-02 (4.82E-04)	1.05E-01 (5.59E-04)	23.44%
Right Lung	2.74E-01 (7.37E-04)	2.99E-01 (1.09E-03)	9.30%
Oesophagus Wall:			
Wall $190 \sim 200\,\mu$m	4.86E-02 (4.71E-03)	2.88E-02 (2.81E-03)	-40.81%
RST Arms	4.65E-02 (1.87E-04)	3.90E-02 (1.48E-04)	-16.13%
Skin Arms:			
Sensitive $50 \sim 100\,\mu$m	2.08E-02 (3.44E-04)	2.66E-02 (4.62E-04)	28.14%

Note: "Diff. (%)" is calculated as (Female - Male) / Male. Standard Error (SE) is derived from the absolute error column provided in the source data.

Chapter 5

Conclusion

The primary objective of this research was to observe the discrepancies between the ICRP voxel and mesh computational phantoms. The voxel phantom became the computational phantom used throughout a multitude of research, then, released in 2020, the mesh phantom became the standard because of its increased geometric and anatomical accuracy at the expense of increased complexity and computational cost. This research aimed to discuss these differences and compare to an experimental model as a benchmark.

A benchmark experiment was conducted using an Anthropomorphic Torso Phantom (ATP) and TLD-100H dosimeters to validate a Monte Carlo LINAC model against a clinical treatment plan. The simulation was compared to experimental data to evaluate the accuracy of the Varian Eclipse Treatment Planning System and Monte Carlo simulations using PHITS. Results indicated significant discrepancies in the Anisotropic Analytical Algorithm (AAA) used by Varian Eclipse at tissue-lung interfaces, where the model fails to accurately account for the drastic density transition between the water-equivalent phantom material and the low-density polystyrene lung inserts.

Following the experimental measurements, the PHITS simulated ATP values demonstrated strong agreement with the measured ATP data, validating the PHITS simulation as a reliable method for dose calculation as opposed to the AAA calculation. These simulated results were used as the benchmark for comparison with the ICRP voxel and mesh models.

The benchmark analysis revealed that the torso phantom provided an accurate estimate for the tumor target, with dose agreement within 3% for both the male voxel and mesh phantoms. However, the results also highlighted significant discrepancies in out-of-target organ doses, largely driven by differences in organ positioning and anatomical complexity between the phantom types.

Beyond the male phantoms, the results for the female mesh phantom showed how the different body size and shape affect radiation dose. While the male models maintained target dose agreement within 3%, the female tumor dose discrepancy was approximately 10%. This variation is primarily attributed to the smaller stature and reduced volume of surrounding tissue in the female phantom, which provides less beam attenuation before radiation reaches the target. Furthermore, sexual differences in anatomy significantly impacted out-of-field organs, most notably in the breast tissue. The female breast tissue, being considerably larger and extending further laterally into low-dose regions, resulted in a significantly lower mean organ dose compared to the male's more localized breast tissue situated closer to the high-dose thoracic region. These results further validate the necessity of using sex-specific mesh phantoms to capture anatomical differences that may be lost in simplified representations.

Among the three models, the ICRP voxel and mesh phantoms exhibited superior Figures of Merit (FOM) compared to the ATP. The lower FOM for the ATP was due to a high relative error (RE), attributed primarily to the sub-optimal mesh generated by the digitization process. While the voxel and mesh phantoms provided comparable FOMs, the voxel model offered shorter batch times at the cost of higher RE. In contrast, the refined geometric discretization of the mesh phantom allows the analysis of fine anatomical structures beyond the resolution limits of the voxelized geometry.

A comparison of ICRP phantom dose distributions revealed that the tumor volume received a difference in dose of approximately 1%, likely due to the varying attenuation of the surrounding organs. In contrast, the liver showed the most significant discrepancy at 95%, attributed to substantial differences in mass and spatial orientation between phantoms; as illustrated in Figure 4.2, the mesh liver extends more cranially toward the tumor than its voxel counterpart. Furthermore, the mass-weighted average for the right lung demonstrated

10% better agreement between phantoms than the left lung. Although mass variations between the left and right lungs were minimal in both phantoms, the increased anatomical complexity of the left lung introduces a greater discretization error when transitioning from the voxel to the mesh geometry.

The study identifies several major areas of error, with the most significant discrepancies arising from cumulative positional shifts when transitioning between experimental and simulation environments. This issue was magnified by the use of small thermoluminescent dosimeters (TLDs) and high-definition beams with steep dose gradients; a shift of just a few millimeters—within a potential 2 cm physical setup margin—could move a dosimeter from a high-dose to a low-dose region. These errors were driven by manual setup variability during the substitution of markers for TLDs and by computational modeling inaccuracies introduced during the multi-step conversion of CT images into digital geometry. Additionally, the Anisotropic Analytical Algorithm (AAA) exhibited a systematic 18.3% underestimation of the tumor dose because it could not accurately model lateral electronic disequilibrium (LED) within the heterogeneous environment of the lungs. During the ATP segmentation, the plastic thickness between organs was ignored, potentially introducing errors into the PHITS simulation. Measurement uncertainty was also present, with a combined 3.5% experimental uncertainty attributed to TLD repeatability, detector sensitivity, and beam calibration. Finally, statistical uncertainty in the Monte Carlo simulations was controlled by converging dose calculations to less than 5% in primary regions of interest.

While the ATP, voxel, and mesh phantoms all provide strong agreement in-target, the mesh phantom provides insights into anatomically sensitive regions that the ATP and voxel lack. Considering the low FOM from the ATP and similar FOM from the voxel phantom, the mesh phantom is an optimal model for future phantom-related research. This study highlights the limitations of the AAA calculation model when applied to heterogeneous media, such as lung tissue. Furthermore, by comparing the ATP, voxel, and mesh phantoms, this research demonstrates that the mesh phantom is computationally superior. Ultimately, the mesh phantom is validated as the most effective model because it simultaneously maintains experimental target accuracy and high-fidelity anatomical representation. This research rep-

resents a significant contribution to the field of health physics by providing the first empirical validation for the ICRP Publication 145 mesh-type phantoms in a complex clinical scenario. While these phantoms have been characterized through computational benchmarks, this study offers the necessary experimental measurements.

Future work will involve shifting the dosimeters currently positioned at the beam periphery to more precisely observe dose discrepancies as they move in and out of the beamline. Additionally, the scope of this research will be expanded by utilizing other published mesh phantoms, including pediatric and pregnant patient models, and by incorporating the female voxel phantom into the comparison. Finally, while this study characterized the limitations of the AAA algorithm, future investigations will compare these results against AcurosXB calculation models to evaluate potential dosimetric improvements and identify possible discrepancies in heterogeneous media.

Bibliography

[1] W. S. Snyder, M. R. Ford, G. G. Warner, and H. L. Fisher. Estimates of absorbed fractions for monoenergetic photon sources uniformly distributed in various organs of a heterogeneous phantom. *Journal of Nuclear Medicine*, 10(Supplement 3):5–52, 1969. MIRD Pamphlet No. 5.

[2] International Commission on Radiological Protection. *Report of the Task Group on Reference Man*. ICRP Publication 23. Pergamon Press, Oxford, 1975. Adopted by the Commission in October 1974.

[3] International Commission on Radiological Protection. Basic anatomical and physiological data for use in radiological protection: Reference values. *Annals of the ICRP*, 32 (3-4):1–277, 2002. ICRP Publication 89.

[4] International Commission on Radiological Protection. The 2007 recommendations of the international commission on radiological protection. *Annals of the ICRP*, 37(2-4): 1–332, 2007. ICRP Publication 103.

[5] ICRP. *Adult Reference Computational Phantoms. ICRP Publication 110*, volume 39(2). Ann. ICRP, 2009.

[6] International Commission on Radiological Protection. Basic anatomical and physiological data for use in radiological protection: The skeleton. *Annals of the ICRP*, 25(2): 1–80, 1995. ICRP Publication 70.

[7] International Commission on Radiation Units and Measurements. Photon, electron, proton and neutron interaction data for body tissues. ICRU Report 46, ICRU, Bethesda, MD, 1992.

[8] International Atomic Energy Agency. Commenting on behalf of the organisation: ICRP Draft Recommendations. https://www.icrp.org/consultations/recommendations. Submitted by Trevor Boal. Accessed: October 3, 2025.

[9] Nuclear Regulatory Commission. Radiation Protection. Federal Register, jul 2014. Proposed Rule. 79 FR 43284.

[10] ICRP. *Adult mesh-type reference computational phantoms. ICRP Publication 145*, volume 49(3). Ann. ICRP, 2020.

[11] International Commission on Radiological Protection. Dose coefficients for external exposures to mesh-type reference computational phantoms. *Annals of the ICRP*, 53(3), 2024. ICRP Publication 156.

[12] C. J. Werner, J. S. Bull, C. J. Solomon, F. B. Brown, G. W. McKinney, M. E. Rising, D. A. Dixon, R. L. Martz, H. G. Hughes, L. J. Cox, A. J. Zukaitis, J. C. Armstrong, R. A. Forster, and L. Casswell. MCNP6 user's manual code version 6.2. Technical Report LA-UR-17-29981, Los Alamos National Laboratory, Los Alamos, NM, 2017.

[13] S. Agostinelli et al. Geant4—a simulation toolkit. *Nuclear Instruments and Methods in Physics Research Section A: Accelerators, Spectrometers, Detectors and Associated Equipment*, 506(3):250–303, 2003.

[14] The PHITS Development Team. PHITS: Particle and heavy ion transport code system, version 3.35. https://phits.jaea.go.jp/, 2023.

[15] Kansas State University. Beocat Research Computing Cluster Support Documentation. https://support.beocat.ksu.edu/BeocatDocs/. Accessed: December 10, 2025.

[16] Message Passing Interface Forum. *MPI: A Message-Passing Interface Standard Version 4.0*, June 2021. URL https://www.mpi-forum.org/docs/mpi-4.0/mpi40-report.pdf.

[17] Rohit Chandra, Leo Dagum, David Kohr, Ramesh Menon, Dror Maydan, and Jeff McDonald. *Parallel programming in OpenMP*. Morgan kaufmann, 2001.

[18] Barbara Chapman, Gabriele Jost, and Ruud van der Pas. *Using OpenMP: Portable Shared Memory Parallel Programming*. The MIT Press, Cambridge, MA, 2008.

[19] PHITS Development Team. *PHITS User's Manual, Version 3.33*. Japan Atomic Energy Agency, 2023. URL https://phits.jaea.go.jp/manual/manualE-phits.pdf. Section 5.17: Weight Window.

[20] International Commission on Radiological Protection. Assessment of radiation exposure of astronauts in space. *Annals of the ICRP*, 42(4):1–339, 2013. ICRP Publication 123.

[21] Indrin J. Chetty et al. Report of the AAPM Task Group No. 105: Issues associated with clinical implementation of Monte Carlo-based photon and electron external beam programs. *Medical Physics*, 34(12):4818–4853, 2007.

[22] W. Ulmer, J. Pyykkonen, and W. Kaissl. A 3d photon superposition/convolution algorithm and its foundation on analytical beam models. *Physics in Medicine & Biology*, 50(8):1767–1790, 2005.

[23] Oleg N. Vassiliev, Todd A. Wareing, John McGhee, Greg Failla, Mohammad R. Salehpour, and Firas Mourtada. Validation of a new grid-based Boltzmann equation solver for dose calculation in radiotherapy with photon beams. *Physics in Medicine & Biology*, 55(3):581–598, 2011.

[24] Janne Sievinen, Waldemar Ulmer, and Wolfgang Kaissl. AAA photon dose calculation model in Eclipse™. White paper, Varian Medical Systems, Palo Alto, CA, 2005. URL https://www.varian.com/. Accessed: December 16, 2025.

[25] Ann Van Esch, Laura Tillikainen, Jukka Pyykkonen, Mikko Tenhunen, Hannu Helminen, Sami Siljamäki, Jyrki Alakuijala, Marta Paiusco, Mauro Iori, and Dominique P. Huyskens. Testing of the analytical anisotropic algorithm for photon dose calculation. *Medical Physics*, 33(11):4130–4148, nov 2006. doi: 10.1118/1.2358333.

[26] Varian Medical Systems. *Eclipse Photon and Electron Algorithms Reference Guide*. Varian Medical Systems, Palo Alto, CA, mar 2015.

[27] International Commission on Radiological Protection. Conversion Coefficients for Radiological Protection Quantities for External Radiation Exposures. *Annals of the ICRP*, 40(2-5), 2010. doi: 10.1016/j.icrp.2011.10.001. ICRP Publication 116.

[28] International Commission on Radiological Protection. Dose Coefficients for External Exposures to Environmental Sources. *Annals of the ICRP*, 49(2):11–145, 2020. doi: 10.1177/0146645320906277. ICRP Publication 144.

[29] National Cancer Institute. External Beam Radiation Therapy for Cancer. https://www.cancer.gov/about-cancer/treatment/types/radiation-therapy/external-beam. Accessed: August 5, 2025.

[30] Eric J. Hall and Amato J. Giaccia. *Radiobiology for the Radiologist*. Wolters Kluwer, Philadelphia, PA, 8th edition, 2019.

[31] Bryan P. Bednarz. *Detailed Varian Clinac Accelerator Modeling for Calculating Intermediate- and Low-level Non-target Organ Doses from Radiation Treatments*. Phd thesis, Rensselaer Polytechnic Institute, Troy, NY, 2006.

[32] Vladislav Sandul, Sarah Salih Al-Hamami, Jiří Kubeš, Marco Durante, and Thomas Friedrich. Radiation-induced lymphopenia: A data compilation to unveil relevant factors and mitigation strategies. *Clinical and Translational Radiation Oncology*, 56:101071, nov 2025. doi: 10.1016/j.ctro.2025.101071. eCollection January 2026.

[33] Lama Hadid, Anna Gardumi, and Aurélie Desbrée. Evaluation of absorbed and effective doses to patients from radiopharmaceuticals using the ICRP 110 reference computational phantoms and ICRP 103 formulation. *Radiation Protection Dosimetry*, 156(2): 141–159, sep 2013. doi: 10.1093/rpd/nct049.

[34] M. Hetrick, R. Leggett, M. Hiller, and K. Eckerman. Practical overview of the ICRP

publication 145 phantoms for use with MCNP. *Journal of Radiological Protection*, 43 (1):011502, 2023. doi: 10.1088/1361-6498/acb4d0.

[35] Douglas S. McGregor and J. Kenneth Shultis. *Radiation Detection: Concepts, Methods, and Devices*. CRC Press, Boca Raton, FL, 2020.

[36] Thermo Fisher Scientific. *Harshaw Model 3500 TLD Reader with WinREMS Software User Guide*. Thermo Fisher Scientific, Oakwood Village, OH, .

[37] Yeon Soo Yeom, Chansoo Choi, Haegin Han, Hanjin Lee, Bangho Shin, Thang Tat Nguyen, Min Cheol Han, Choonsik Lee, and Chan Hyeong Kim. Dose coefficients of mesh-type ICRP reference computational phantoms for idealized external exposures of photons and electrons. *Nuclear Engineering and Technology*, 51(2):597–608, apr 2019. doi: 10.1016/j.net.2018.12.010.

[38] Data Spectrum Corporation. *Anthropomorphic Torso Phantom™ User's Manual*. Data Spectrum Corporation, Hillsborough, NC. Accessed: August 1, 2025. Available at https://www.dataspectrum.com/.

[39] Ignacio Bartol, Martin Graffigna, Mauricio Tano, and Shaheen Dewji. Geometries of the lower airways of the human respiratory tract. https://doi.org/10.6084/m9.figshare.24787773, 2023.

[40] Ignacio R. Bartol, Martin S. Graffigna Palomba, Mauricio E. Tano, and Shaheen A. Dewji. Computational multiphysics modeling of radioactive aerosol deposition in diverse human respiratory tract geometries. *Communications Engineering*, 3(1), 2024. doi: 10.1038/s44172-024-00296-z.

[41] Thermo Fisher Scientific. TLD-100H (LiF:Mg,Cu,P) High-Sensitivity TLD Chips. Product Data Sheet, .

[42] Ramesh S. Bilimaga. Therapeutic ratio: An overview, past present future. Presentation slides, 2000. International Journal of Radiation Oncology Biol. Phys., Vol. 46, No. 1.

[43] Varian Medical Systems. Eclipse™ Treatment Planning System. https://www.varian.com/products/software/treatment-planning/eclipse, 2025.

[44] Harold Liepert. Mcp physical constants. Personal communication via email from Thermo Fisher Scientific, June 2025.

[45] Autodesk, Inc. *Autodesk Meshmixer*. Autodesk, Inc., San Rafael, CA, 2021. URL http://www.meshmixer.com/. Version 3.5.474. Accessed: October 1, 2025.

[46] Dassault Systèmes. SOLIDWORKS 2025. https://www.solidworks.com/, 2024. Accessed: August 20, 2025.

[47] Christophe Geuzaine and Jean-François Remacle. Gmsh: A three-dimensional finite element mesh generator with built-in pre- and post-processing facilities, Version 4.14.0. https://gmsh.info, 2025. Accessed: August 20, 2025.

[48] Fengjie Cui, Shaoxian Gu, Ningyu Wang, Chuou Yin, Shengyuan Zhang, Jinyou Hu, Yunzhu Cai, Zhangwen Wu, Chengjun Gou, and Jun Wang. Hybrid pencil beam model based on photon characteristic line algorithm for lung radiotherapy in small fields. *Open Physics*, 20(1):683–694, 2022.

[49] Song Gao, Yanzong Chi, Yi Wang, Yan Zhang, and Yi Lv. Dosimetric impact of acuros xb and aaa dose calculation algorithm on vmat treatment plans for stage i and iii lung tumors. *Radiation Oncology*, 8(1):220, 2013. doi: 10.1186/1748-717X-8-220.

[50] Antonella Fogliata, Giorgia Nicolini, Alessandro Clivio, Eugenio Vanetti, and Luca Cozzi. Dosimetric evaluation of acuros xb advanced dose calculation algorithm in heterogeneous media. *Radiation Oncology*, 6(1):82, 2011. doi: 10.1186/1748-717X-6-82.

[51] Jarkko J Ojala, Mika K Kapanen, Pasi Sipila, Tero Lahtinen, and Maunu A Pitkanen. Performance of dose calculation algorithms from three generations in lung sbrt: comparison with full monte carlo-based dose distributions. *Journal of Applied Clinical Medical Physics*, 15(2):4662, 2014. doi: 10.1120/jacmp.v15i2.4662.

Appendix A

MLC 4-field Treatment Dimensions

This appendix contains information on the MLC movement for each field of the 4-field treatment plan. This includes the leaf pair, the offset of that leaf pair, each field size and the offset of each leaf set on the center that is included in the banks.

Table A.1: Leaf Pair Offset Data (Fields 1 and 2)

Leaf Pair	Offset (mm)	Field 1			Field 2		
		Size (cm)	Bank B (cm)	Bank A (cm)	Size (cm)	Bank B (cm)	Bank A (cm)
60	195	0	-0.015	0.015	0	-0.078	0.078
59	185	0	-0.015	0.015	0	-0.078	0.078
58	175	0	-0.015	0.015	0	-0.078	0.078
57	165	0	-0.015	0.015	0	-0.078	0.078
56	155	0	-0.015	0.015	0	-0.078	0.078
55	145	0	-0.015	0.015	0	-0.078	0.078
54	135	0	-0.015	0.015	0	-0.078	0.078
53	125	0	-0.015	0.015	0	-0.078	0.078
52	115	0	-0.015	0.015	0	-0.078	0.078
51	105	0	-0.015	0.015	0	-0.078	0.078
50	97.5	0	-0.015	0.015	0	-0.078	0.078
49	92.5	0	-0.015	0.015	0	-0.078	0.078
48	87.5	0	-0.015	0.015	0	-0.078	0.078
47	82.5	0	-0.015	0.015	0	-0.078	0.078
46	77.5	0	-0.015	0.015	0	-0.078	0.078
45	72.5	0	-0.015	0.015	0	-0.078	0.078
44	67.5	0	-0.015	0.015	0	-0.078	0.078
43	62.5	0	-0.015	0.015	0	-0.078	0.078
42	57.5	0	-0.015	0.015	0	-0.078	0.078
41	52.5	0	-0.015	0.015	0	-0.078	0.078
40	47.5	0	-0.015	0.015	0	-0.078	0.078
39	42.5	0	-0.015	0.015	0	-0.078	0.078
38	37.5	0	-0.015	0.015	0	-0.078	0.078
37	32.5	0	-0.015	0.015	0	-0.078	0.078
36	27.5	0	-0.015	0.015	0	-0.078	0.078
35	22.5	1.69	0.975	0.715	1.33	0.655	0.675
34	17.5	2.74	1.48	1.26	2.68	1.28	1.4
33	12.5	3.77	1.785	1.985	3.97	1.925	2.045
32	7.5	4.119	1.985	2.134	4.333	2.077	2.256
31	2.5	4.237	2.104	2.133	4.351	2.099	2.252
30	-2.5	4.251	2.111	2.14	4.142	2.069	2.073
29	-7.5	3.928	1.975	1.953	3.925	1.945	1.98
28	-12.5	3.335	1.64	1.695	3.425	1.7	1.725
27	-17.5	2.48	1.08	1.4	2.6	1.4	1.2
26	-22.5	1.24	0.36	0.88	1.36	0.88	0.48
25	-27.5	0	-0.015	0.015	0	-0.078	0.078
24	-32.5	0	-0.015	0.015	0	-0.078	0.078
23	-37.5	0	-0.015	0.015	0	-0.078	0.078
22	-42.5	0	-0.015	0.015	0	-0.078	0.078
21	-47.5	0	-0.015	0.015	0	-0.078	0.078
20	-52.5	0	-0.015	0.015	0	-0.078	0.078
19	-57.5	0	-0.015	0.015	0	-0.078	0.078
18	-62.5	0	-0.015	0.015	0	-0.078	0.078
17	-67.5	0	-0.015	0.015	0	-0.078	0.078
16	-72.5	0	-0.015	0.015	0	-0.078	0.078
15	-77.5	0	-0.015	0.015	0	-0.078	0.078
14	-82.5	0	-0.015	0.015	0	-0.078	0.078
13	-87.5	0	-0.015	0.015	0	-0.078	0.078
12	-92.5	0	-0.015	0.015	0	-0.078	0.078
11	-97.5	0	-0.015	0.015	0	-0.078	0.078
10	-105	0	-0.015	0.015	0	-0.078	0.078
9	-115	0	-0.015	0.015	0	-0.078	0.078
8	-125	0	-0.015	0.015	0	-0.078	0.078
7	-135	0	-0.015	0.015	0	-0.078	0.078
6	-145	0	-0.015	0.015	0	-0.078	0.078
5	-155	0	-0.015	0.015	0	-0.078	0.078
4	-165	0	-0.015	0.015	0	-0.078	0.078
3	-175	0	-0.015	0.015	0	-0.078	0.078
2	-185	0	-0.015	0.015	0	-0.078	0.078
1	-195	0	-0.015	0.015	0	-0.078	0.078

Table A.2: Leaf Pair Offset Data (Fields 3 and 4)

Leaf Pair	Offset (mm)	Field 3			Field 4		
		Size (cm)	Bank B (cm)	Bank A (cm)	Size (cm)	Bank B (cm)	Bank A (cm)
60	195	0	0.009	-0.009	0	0.08	-0.08
59	185	0	0.009	-0.009	0	0.08	-0.08
58	175	0	0.009	-0.009	0	0.08	-0.08
57	165	0	0.009	-0.009	0	0.08	-0.08
56	155	0	0.009	-0.009	0	0.08	-0.08
55	145	0	0.009	-0.009	0	0.08	-0.08
54	135	0	0.009	-0.009	0	0.08	-0.08
53	125	0	0.009	-0.009	0	0.08	-0.08
52	115	0	0.009	-0.009	0	0.08	-0.08
51	105	0	0.009	-0.009	0	0.08	-0.08
50	97.5	0	0.009	-0.009	0	0.08	-0.08
49	92.5	0	0.009	-0.009	0	0.08	-0.08
48	87.5	0	0.009	-0.009	0	0.08	-0.08
47	82.5	0	0.009	-0.009	0	0.08	-0.08
46	77.5	0	0.009	-0.009	0	0.08	-0.08
45	72.5	0	0.009	-0.009	0	0.08	-0.08
44	67.5	0	0.009	-0.009	0	0.08	-0.08
43	62.5	0	0.009	-0.009	0	0.08	-0.08
42	57.5	0	0.009	-0.009	0	0.08	-0.08
41	52.5	0	0.009	-0.009	0	0.08	-0.08
40	47.5	0	0.009	-0.009	0	0.08	-0.08
39	42.5	0	0.009	-0.009	0	0.08	-0.08
38	37.5	0	0.009	-0.009	0	0.08	-0.08
37	32.5	0	0.009	-0.009	0	0.08	-0.08
36	27.5	0	0.009	-0.009	0	0.08	-0.08
35	22.5	1.69	0.715	0.975	1.31	0.675	0.635
34	17.5	2.72	1.24	1.48	2.66	1.38	1.28
33	12.5	3.76	1.975	1.785	3.95	2.035	1.915
32	7.5	4.122	2.137	1.985	4.325	2.252	2.073
31	2.5	4.234	2.128	2.106	4.343	2.252	2.091
30	-2.5	4.25	2.13	2.12	4.138	2.069	2.069
29	-7.5	3.93	1.955	1.975	3.908	1.973	1.935
28	-12.5	3.335	1.695	1.64	3.415	1.72	1.695
27	-17.5	2.48	1.4	1.08	2.6	1.2	1.4
26	-22.5	1.24	0.88	0.36	1.34	0.46	0.88
25	-27.5	0	0.009	-0.009	0	0.08	-0.08
24	-32.5	0	0.009	-0.009	0	0.08	-0.08
23	-37.5	0	0.009	-0.009	0	0.08	-0.08
22	-42.5	0	0.009	-0.009	0	0.08	-0.08
21	-47.5	0	0.009	-0.009	0	0.08	-0.08
20	-52.5	0	0.009	-0.009	0	0.08	-0.08
19	-57.5	0	0.009	-0.009	0	0.08	-0.08
18	-62.5	0	0.009	-0.009	0	0.08	-0.08
17	-67.5	0	0.009	-0.009	0	0.08	-0.08
16	-72.5	0	0.009	-0.009	0	0.08	-0.08
15	-77.5	0	0.009	-0.009	0	0.08	-0.08
14	-82.5	0	0.009	-0.009	0	0.08	-0.08
13	-87.5	0	0.009	-0.009	0	0.08	-0.08
12	-92.5	0	0.009	-0.009	0	0.08	-0.08
11	-97.5	0	0.009	-0.009	0	0.08	-0.08
10	-105	0	0.009	-0.009	0	0.08	-0.08
9	-115	0	0.009	-0.009	0	0.08	-0.08
8	-125	0	0.009	-0.009	0	0.08	-0.08
7	-135	0	0.009	-0.009	0	0.08	-0.08
6	-145	0	0.009	-0.009	0	0.08	-0.08
5	-155	0	0.009	-0.009	0	0.08	-0.08
4	-165	0	0.009	-0.009	0	0.08	-0.08
3	-175	0	0.009	-0.009	0	0.08	-0.08
2	-185	0	0.009	-0.009	0	0.08	-0.08
1	-195	0	0.009	-0.009	0	0.08	-0.08

Appendix B

PHITS Code

The simulations performed in this research utilized the PHITS Monte Carlo code (Particle and Heavy Ion Transport code System). The specific implementation, including the configuration files for the LINAC model and phantoms, is maintained in the following github repository: https://github.com/akmauler/LINACphantoms.

```
file = PHITS_input_MV_varian-ATP.inp
$ 6 MV Varian Clinac 2100C Medical Linear Accelerator Model

[ P a r a m e t e r s ]
 icntl    =           0     # (D=0) 3:ECH 5:NOR 6:SRC 7,8:GSH 11:DSH 12:DUMP
 maxcas   =        100000000    # (D=10) number of particles per one batch (do 10^8 for sim)
 maxbch   =           10    # (D=10) number of batches
 negs     =           1     # (D=0) =1 EGS photon and electron
istdev    =       -1
 emin(12) =     1.0e-2
 file(6)  = ATP.out # (D=phits.out) general output file name
$ file(1)  = c:/phits        # (D=c:/phits) PHITS install folder name
 itetvol  =         0   # (D=0) =1 Volume calculation for tetrahedrons
$ itetra = 2
 itetauto =         0   # (D=0) Automatic mode for tetrahedrons
 itgchk   = 0          # (D=0) Tetra-mesh geometry check 0: off, 1: on

[ Source ]
  totfact =     1        # (D=1.0) global factor
   s-type =     3
     proj = electron        # kind of incident particle

   e-type =     8
    ne = 61
     5.90 0.0037
       5.91 0.0060
       5.92 0.0094
       5.93 0.0147
       5.94 0.0224
       5.95 0.0337
       5.96 0.0500
       5.97 0.0728
       5.98 0.1044
       5.99 0.1474
       6.00 0.2047
       6.01 0.2798
       6.02 0.3764
       6.03 0.4983
       6.04 0.6492
       6.05 0.8322
```

```
        6.06 1.0500
        6.07 1.3036
        6.08 1.5928
        6.09 1.9152
        6.10 2.2662
        6.11 2.6390
        6.12 3.0241
        6.13 3.4104
        6.14 3.7849
        6.15 4.1337
        6.16 4.4429
        6.17 4.6992
        6.18 4.8914
        6.19 5.0104
        6.20 5.0507
        6.21 5.0104
        6.22 4.8914
        6.23 4.6992
        6.24 4.4429
        6.25 4.1337
        6.26 3.7849
        6.27 3.4104
        6.28 3.0241
        6.29 2.6390
        6.30 2.2662
        6.31 1.9152
        6.32 1.5928
        6.33 1.3036
        6.34 1.0500
        6.35 0.8322
        6.36 0.6492
        6.37 0.4983
        6.38 0.3764
        6.39 0.2798
        6.40 0.2047
        6.41 0.1474
        6.42 0.1044
        6.43 0.0728
        6.44 0.0500
        6.45 0.0337
        6.46 0.0224
```

```
       6.47 0.0147
       6.48 0.0094
       6.49 0.0060
       6.50 0.0037
       x0 =     0.00        # (D=0.0) x coordinate of Gaussian center[cm]
     x1 =     0.3061        #  FWHM in x direction[cm].
       y0 =     0.0         # (D=0.0) y coordinate of Gaussian center[cm]
     y1 =     0.3061        # FWHM in y direction[cm]
       z0 =    -0.25        # z coordinate of Gaussian center[cm]
       z1 =      0          # FWHM in z direction[cm].
       dir =      1          # z-direction of beam [isotropic]


[ Material ]
infl:{description/varian_clin_6_PHITS.mtl}
infl:{description/ATP.mtl}
$infl:{description/VOXEL-MATERIAL.mtl}
$infl:{description/MRCP-AM.material}
$ Calibration materials
$ TLD-100H (density = 2.48 g/cm3)
$MAT[ 1 ]
$       6Li   -0.0197$        7Li   -0.2465
$       F     -0.7288$        Mg    -0.0020
$       Cu    -0.0004$        P      -0.0030
$
$ --- Polyethylene, Density = 0.93 g/cm
$MAT[ 2 ]  H  4  C  2
$
$ --- Tissue, Density = 1.00 g/cm
$MAT[ 3 ]  H  -0.104472  C  -0.232190  N  -0.024880  O  -0.630238
$    Na -0.001130  Mg -0.000130  P  -0.001330  S  -0.001990$     Cl -0.001340  K $ -0.001990
      Ca -0.000230  Fe -0.000050
$    Zn -0.000030$
$ --- yoga mat, Density = 0.55 g/cm
$MAT[ 4 ]  C 2 H 3 Cl 1

[ Surface ]
infl:{description/varian_mlc_90_PHITS.geo}
infl:{description/varian_clin_6_PHITS.geo} [1 - 97]
  10  rpp   -20.0 20.0 -36.0 -5.6 -29.0 -4.5
  200  rpp   -20.1 20.1 -36.1 -5.5 -29.1 -4.4
```

```
  800  box    -1000 -1000 -1000 2000 0 0 0 2000 0 0 0 2000
  703  5 s -9.75 -20.35 -14.9 1.15
  731 5 s -4.75 -20.35 -14.9 0.129578749
  732 5 s -9.75 -15.5 -14.9 0.129578749
  733 5 s -11.75 -20.35 -14.9 0.129578749
  734 5 s -9.75 -28.75 -14.9 0.129578749
  735 5 s 13.5 -20.35 -14.9 0.129578749
  736 5 s -9.75 -21.65 -14.9 0.129578749
  737 5 s -9.75 -19.05 -14.9 0.129578749
  738 5 s -11.05 -20.35 -14.9 0.129578749
  739 5 s -8.45 -20.35 -14.9 0.129578749
  740 5 s -9.75 -20.35 -13.6 0.129578749
  666  so     1000.0
$infl:{description/VOXEL-SUR.geo}
$703 5 s -9.75 1.23047 45 1.15
$infl:{description/varian_clin_6_PHITS_mesh.geo} [1 - 97]
$10  rpp -30.8854 30.8854 -18.56301 18.56301 -98.00236 98.00236  $ Phantom box
$20  rpp -31.0854 31.0854 -18.76301 18.76301 -98.20236 98.20236
$90  box -1000 -1000 -1000 2000 0 0 0 2000 0 0 0 2000         $ World boundary
$11 SO 1000.0
$703 5 s -9.75 1.23047 45 1.15
$ Calibration Surfaces
$600 RPP -0.87 -0.55  -0.16 0.16  100.01 100.099  $ TLD100H
$601 RPP -5 5  -5 5  98.5 100  $ Bolus
$602 RPP -4.5 4.5  -4.5 4.5  100 100.109  $ plastic
$603 RPP -10 10  -10 10  100.109 102.109 $ mat that the TLDs are on

[ Cell ]
infl:{description/mlc_7_g_08_PHITS-field1.cel}
infl:{description/varian_clin_6_PHITS-ATP.cel}
infl:{description/ATP.cel}
$infl:{description/mlc_7_g_08_PHITS-field1.cel}
$infl:{description/varian_clin_6_PHITS_voxel.cel}
$infl:{description/VOXEL_CELL.cel}
$666    -1     666
$infl:{description/mlc_7_g_08_PHITS_mesh-field1.cel}
$infl:{description/varian_clin_6_PHITS_mesh.cel}
$infl:{description/MRCP-AM-varian-mesh.cell}
$999 -1 11
$ Calibration cells
$infl:{files/TLDandbolus.cell}
```

```
$999 -1 11

[ Volume ]
$infl:{description/ATP-VOL}
$infl:{description/VOXEL-VOL.txt}
$infl:{description/CAL-VOL.txt}

[ Transform ]
$                10 x 10 SAD=100 cm
$*TR1 0 0 0 0 90 90 90 2.862405 87.13759 90 92.86241 2.862405
$*TR2 0 0 0 0 90 90 90 2.862405 92.86241 90 87.13759 2.862405
$*TR3 0 0 0 2.862405 90 87.13759 90 0 90 92.86241 90 2.862405
$*TR4 0 0 0 2.862405 90 92.86241 90 0 90 87.13759 90 2.862405
$                            6 x 6
*TR1 0 0 0 0 90 90 90 1.718358 88.28164 90 91.71836 1.718358
*TR2 0 0 0 0 90 90 90 1.718358 91.71836 90 88.28164 1.718358
*TR3 0 0 0 1.718358 90 88.28164 90 0 90 91.71836 90 1.718358
*TR4 0 0 0 1.718358 90 91.71836 90 0 90 88.28164 90 1.718358
$
$ ********************************************************************************** $ phantom
     transformation
$Field 1
*tr5  9.75 -14.9 120.35  0 90 270  90 90 0  90 180 90  1
$Field 2
$*tr5  20.35 -14.9 90.25  90 90 180  0 90 90  90 180 90  1
$Field 3
$*tr5  -9.75 -14.9 79.65  180 90 90  90 90 180  90 180 90  1
$Field 4
$*tr5  -20.35 -14.9 109.75  270 90 0  180 90 270  90 180 90  1

[ T - T r a c k ] off
    title = Track in xyz mesh
     mesh =  xyz            # mesh type is xyz scoring mesh
   x-type =    2            # x-mesh is linear given by xmin, xmax and nx
     xmin =  -70.000000      # minimum value of x-mesh points
     xmax =   70.000000      # maximum value of x-mesh points
$    xmin =  -20.000000      # minimum value of x-mesh points$     xmax =   20.000000      #
     maximum value of x-mesh points
       nx =   280           # number of x-mesh points
   y-type =    2            # y-mesh is linear given by ymin, ymax and ny
     ymin =  -10      # minimum value of y-mesh points
```

```
     ymax =   12     # maximum value of y-mesh points
       ny =    10            # number of y-mesh points
   z-type =    2            # z-mesh is linear given by zmin, zmax and nz
     zmin =   -30.00000      # minimum value of z-mesh points
     zmax =   115.00000      # maximum value of z-mesh points
$    zmin =   70.00000      # minimum value of z-mesh points$     zmax =   110.00000      #
    maximum value of z-mesh points
       nz =   160            # number of z-mesh points
  2D-type =    3            # 1:Cont, 2:Clust, 3:Color, 4:xyz, 5:mat, 6:Clust+Cont, 7:Col+
      Cont
     axis =   xz            # axis of output
211  file = track-ATP.out     # file name of output for the above axis
     part = electron photon all
   e-type =    1            # e-mesh is given by the below data
       ne =    1            # number of e-mesh points
             0.0  1000.0
     unit =    1             # unit is [1/cm^2/source]
 $   resol =    15
 $   width =   0.01
   epsout =    1            # (D=0) generate eps file by ANGEL
    gshow =    1            # 0: no 1:bnd, 2:bnd+mat, 3:bnd+reg 4:bnd+lat
221
[ T - T r a c k ] off
    title = Track at phantom
     mesh =  xyz            # mesh type is xyz scoring mesh
   x-type =    2            # x-mesh is linear given by xmin, xmax and nx
     xmin =  -15      # minimum value of x-mesh points
     xmax =   15      # maximum value of x-mesh points
     nx =   120            # number of x-mesh points
   y-type =    2            # y-mesh is linear given by ymin, ymax and ny
     ymin =  -15      # minimum value of y-mesh points
231  ymax =   15      # maximum value of y-mesh points
     ny =    120            # number of y-mesh points
   z-type =    2            # z-mesh is linear given by zmin, zmax and nz
     zmin =   98.6      # minimum value of z-mesh points
     zmax =   101.4      # maximum value of z-mesh points
       nz =   25            # number of z-mesh points
  2D-type =    3            # 1:Cont, 2:Clust, 3:Color, 4:xyz, 5:mat, 6:Clust+Cont, 7:Col+
      Cont
     axis =   yx            # axis of output
     file = track-at-ATP.out       # file name of output for the above axis
```

```
     part = electron photon
   e-type =    1            # e-mesh is given by the below data
       ne =    1            # number of e-mesh points
             0.0  1000.0
     unit =    1            # unit is [1/cm^2/source]
 $   resol =     15
 $   width =   0.01
   epsout =    1            # (D=0) generate eps file by ANGEL
    gshow =    1            # 0: no 1:bnd, 2:bnd+mat, 3:bnd+reg 4:bnd+lat



[ T - deposit ] off
     mesh =    xyz            # mesh type is xyz scoring mesh
  x-type =      2            # x-mesh is linear given by xmin, xmax and nx
     xmin =    -37.8854       # minimum value of x-mesh points
     xmax =     37.8854       # maximum value of x-mesh points
       nx =     60            # number of x-mesh points
$  y-type =      1            # y-mesh is given by the below data$       ny =      1
              # number of y-mesh points
$           -24.56301  24.56301
   y-type =      2            # y-mesh is linear given by zmin, zmax and nz
     ymin =    -98.00236      # minimum value of y-mesh points
     ymax =     98.00236      # maximum value of y-mesh points
       ny =    180            # number of y-mesh points
$  z-type =      2            # z-mesh is linear given by zmin, zmax and nz$     zmin =
    -98.00236      # minimum value of z-mesh points
$    zmax =     98.00236      # maximum value of z-mesh points$       nz =    180
              # number of z-mesh points
   z-type =      1           # y-mesh is given by the below data
       nz =      1            # number of y-mesh points
           60  100
     axis =     xy            # axis of output
     file = AM_dose_ATP.dat  # file name of output for the above axis
    ginfo =      0            # (D=0) 0:no, 1:show in graph, 2:add file
    resol =     15            # (D=1) resolution of gshow or rshow
    width =   0.01            # (D=0.5) width of lines for gshow or rshow
   epsout =      1            # (D=0) generate eps file by ANGEL
   unit = 0


[ T - Gshow ] off
     mesh =    xyz            # mesh type is xyz scoring mesh
```

```
   x-type =      2            # x-mesh is linear given by xmin, xmax and nx
     xmin =    -37.8854       # minimum value of x-mesh points
     xmax =     37.8854       # maximum value of x-mesh points
       nx =     60            # number of x-mesh points
   y-type =      1            # y-mesh is given by the below data
       ny =      1            # number of y-mesh points
          -24.56301  24.56301
   z-type =      2            # z-mesh is linear given by zmin, zmax and nz
     zmin =    -98.00236      # minimum value of z-mesh points
     zmax =     98.00236      # maximum value of z-mesh points
       nz =    180            # number of z-mesh points
     axis =     xz            # axis of output
     file = ATP-AM_vis-Varian.dat  # file name of output for the above axis
   output =      2            # (D=2) 1:bnd, 2:bnd+mat, 3:bnd+num 4:bnd+mat+num
    ginfo =      0            # (D=0) 0:no, 1:show in graph, 2:add file
    resol =     15            # (D=1) resolution of gshow or rshow
    width =   0.01            # (D=0.5) width of lines for gshow or rshow
   epsout =      1            # (D=0) generate eps file by ANGEL

[t-deposit]
    title = Deposit energy in a certain region
     mesh = reg
      reg = { 701-708 } {710-740}
$ voxel region
$    reg = { 1 - 141 } 703$ mesh region
$     reg = 100 200 {300-303} {400-405} 500 501 600 700 703 {800-808} 910 1000
$             1010 1100 1110 1200
$             1210 1300 1400 1500 1600 1700 1800 1900 2000
$             2100 2200 2300 2400 2500 2600 2700 2800 2900 3000 3100 3200 3300
$             3400 3500 3600 3700 3800 3900 4100 4200 4300 4400 4500 4600 4700
$             4800 4900 5000 5100 5200 5300 5400 5500 5600 5700 5800 6100 6200
$             6300 6400 6500
$             6600 {6700-6702} 6800 6801 {6900-6902} 7000 7100 {7200-7203}
$             7300 {7400-7403} 7500 7501 {7600-7602} 7700 {7800-7802} 7900 {8000-8002}
$             8100 8200 8300 {8400-8402} 8500 8600 8700 8800 8900 9000 9100 9200 9300
$             9400 9500 9700 9900 10000 10100 10200 10300 10400 10500 10600  10700 10800
$             10900 {11000-11003} 11300 11400 11500 11600 11700 11800
$             11900 12000 12100
$             12200 12201 12300 12301 12400 12401 12500 12501 12600 12700 12800 12801
$             12900 13000 13100 13200 13300 13301 13400 13500 13600 13700 13701 13800
$             14000
```

```
$ Calibration region
$      reg  = 601 603 604 605 606 607 608 609 610 611 612 613 614 615
$     616 617 618 619 620 621 622 623 624
$     625 626 627 628 629 630 631
$     632 633 634 635 636 637 638 639 640 641
      axis = reg
 material = all
   output = dose
      file = Result_ATP-AM_VARIAN.out
      unit = 0
```

```
$ varian_clin_6_PHITS.mtl
$ MATERIAL CARDS FOR 6 MV ACCELERATOR MODEL
$ MATERIAL CARDS
$ LINAC MATERIALS

$ negative is mass ratio (weight fraction)
$ Tungsten (74)
MAT[91]
     W -1.0

$ Copper (29)
MAT[92]
     Cu -1.0

$ Iron (26)
MAT[93]
     Fe -1.0

$ Tantalum (73)
MAT[94]
     Ta -1.0

$ lead (82)
MAT[95]
     Pb -1.0

$ carbon-12 (6000), Nitrogen-14 (7014), Oxygen-16 (8016), Argon-40 (18000)
MAT[97]
     12C -0.0001
     14N -0.7553
     16O -0.2318
     40Ar -0.0128
```

```
$ ATP.mtl
$ MATERIAL CARDS FOR ANRHTOMORPHIC TORSO PHANTOM MODEL
$ negative is mass ratio (weight fraction)
$ water (density = 1.0 g/cm3)
MAT[ 1 ]    H 2  O 1

$ PMMA (density = 1.19 g/cm3)
MAT[ 2 ]    C 5 H 8 O 2

$ TLD-100H (density = 2.48 g/cm3)
MAT[ 3 ]
        6Li  -0.0197
        7Li  -0.2465
        F    -0.7288
        Mg   -0.0020
        Cu   -0.0004
        P    -0.0030

$ Tumor (density = 0.9086 g/cm3)
MAT[ 4 ]   C 5 H 8

$ Spine (density = 2.2 g/cm3)
MAT[ 5 ]
        C    -0.24
        F    -0.76

$ Polysterene beads (density = 0.02 g/cm3)
MAT[ 6 ]
        C    -0.923
        H    -0.077

$ Air (density = 0.00120479 g/cm3)
MAT[ 7 ]
        C   -0.000124
        N   -0.755267
        O   -0.231781
        Ar  -0.012827

$ water (density = 1.0 g/cm3)
MAT[ 8 ]    H 2  O 1
```

```
$ water (density = 1.0 g/cm3)
MAT[ 9 ]    H 2  O 1

$ water (density = 1.0 g/cm3)
MAT[ 10 ]    H 2  O 1

$ TLD-100H (density = 2.48 g/cm3)
MAT[ 11 ]
        6Li   -0.0197
        7Li   -0.2465
        F     -0.7288
        Mg    -0.0020
        Cu    -0.0004
        P     -0.0030
```

```
$ varian_mlc_90_PHITS.geo
$ GEOMETRY CARDS FOR MLC IN 6 MV ACCELERATOR MODEL
$
$ MLC 1 surfaces
$ 0.25 cm mlc
$ Segment # 1
201 py 0.0779
202 py -0.0779
203 pz 47.3
204 pz 47.6
$ Segment # 2
205 p 0 0 0 0 0.11855 47.6 5 0.11855 47.6
206 p 0 0 0 0 -0.11855 47.6 5 -0.11855 47.6
207 pz 48.9
$ Segment # 3
208 p 0 0 0 0 0.0581 48.9 5 0.0581 48.9
209 pz 49.1
$ Segment # 4
210 p 0 0 0 0 -0.1833 49.1 5 -0.1833 49.1
211 pz 51.6
$ 209 pz 49.1
$ Segment # 5
212 pz 51.8
$ Segment # 6
213 pz 53.1
$ Segment # 7
214 pz 53.4
218 c/y 16.0 50.3 16.0
219 px 16.7
220 px 8.67
$ MLC 2 surface
222 c/y -16.0 50.3 16.0
223 px -16.7
224 px -8.67
$ Carrier
231 py 0
232 p 0 0 0 0 -0.06 49.1 5 -0.06 49.1
233 py -70
234 py 70
235 pz 45.5
```

```
236 pz 55.5
237 px 0
238 px 70
239 px -70
240 pz 51.61
$ 0.5 cm mlc
241 py 0.1558
242 py -0.1558
245 p 0 0 0 0 0.2371 47.6 5 0.2371 47.6
246 p 0 0 0 0 -0.2371 47.6 5 -0.2371 47.6
248 p 0 0 0 0 0.1788 48.9 5 0.1788 48.9
250 p 0 0 0 0 -0.304 49.1 5 -0.304 49.1
```

```
$ varian_clin_6_PHITS.geo
$ GEOMETRY CARDS FOR 6 MV ACCELERATOR MODEL
$ 11 RPP -75.0 75.0 -75.0 75.0 -50.0 75.0
12 RPP -70.0 70.0 -70.0 70.0 -70.0 45.5
13 RCC 0.0 0.0 0.0 0.0 0.0 0.0889 0.301
14 RCC 0.0 0.0 0.0889 0.0 0.0 0.1575 0.301
15 RCC 0.0 0.0 -0.254 0.0 0.0 1.524 0.889
16 RCC 0.0 0.0 -0.254 0.0 0.0 1.524 0.301
17 RPP -4.445 4.445 -6.349 4.826 -2.54 4.445
18 RCC 0.0 -8.89 0.508 0.0 2.541 0.0 2.54
$ 19 RCC 0.0 -8.89 0.508 0.0 12.448 0.0 1.6
19 RPP -1.6 1.6 -8.89 3.558 -1.2 1.6
20 RCC 0.0 0.0 -2.54 0.0 0.0 6.984 3.557
21 RPP -4.445 4.445 -6.349 8.509 4.445 7.8
22 RCC 0.0 -8.89 6.19 0.0 2.541 0.0 1.5
23 RCC 0.0 -8.89 6.19 0.0 17.399 0.0 0.4445
24 TRC 0.0 0.0 7.8 0.0 0.0 -6.2 1.945 0.400
25 RCC 0.0 0.0 4.445 0.0 0.0 3.355 2.54
26 RCC 0.0 0.0 -2.54 0.0 0.0 1.77 0.302
27 TRC 0.0 0.0 12.446 0.0 0.0 -2.05 2.438 0.01
$ 28 TRC 0.0 0.0 12.444 0.0 0.0 -1.3335 1.3335 0.002
29 RCC 0.0 0.0 12.446 0.0 0.0 0.32 3.81
$ 30 TRC 0.0 0.0 12.882 0.0 0.0 0.67 2.39 1.427
31 RPP -7.04 -4.445 -6.349 -0.635 -2.54 7.9385
32 RPP 4.5 7.04 -6.349 -0.635 -2.54 7.9385
33 RCC -3.81 8.65 -2.54 7.62 0.0 0.0 4.445
34 RCC -3.81 8.65 -2.54 7.62 0.0 0.0 12.70
35 RCC -10.15 8.65 -2.54 20.3 0.0 0.0 12.70
36 WED -3.81 -3.3 -6.86 0.0 5.967 -16.762 0.0 11.95 4.32 7.62 0.0 0.0
37 WED -3.81 12.8 -14.55 0.0 17.02 5.881 0.0 -4.15 12.01 7.62 0.0 0.0
38 WED -3.81 20.82 1.27 0.0 -6.096 17.02 0.0 -12.17 -4.36 7.62 0.0 0.0
39 RPP -10.15 10.15 1.26 8.65 7.8 10.638
40 RPP -10.159 10.159 -15.494 -7.240 -19.812 -5.207
41 WED -10.159 -7.240 -19.812 0.0 7.239 0.0
        0.0 0.0 14.605 20.318 0.0 0.0
42 RPP -20.32 20.32 25.147 40.386 2.287 9.906
43 WED -20.32 25.146 2.287 0.0 0.0 -10.16
        0.0 15.24 0.0 40.64 0.0 0.0
44 RPP -3.81 3.81 -7.62 -4.32 -5.08 -2.55
45 RPP -20.32 -10.16 -15.494 7.366 -19.812 -2.032
```

```
46 RPP 10.16 20.32 -15.494 7.366 -19.812 -2.032
47 RPP -20.32 -10.16 7.366 25.146 -19.182 9.906
48 RPP 10.16 20.32 7.366 25.146 -19.812 9.906
49 WED 10.16 -15.494 -2.023 0.0 0.0 3.547
       10.16 0.0 0.0 0.0 22.86 0.0
50 WED -10.16 -15.494 -2.023 -10.16 0.0 0.0
       0.0 0.0 3.547 0.0 22.86 0.0
51 RPP -20.32 20.32 -15.494 0.0 -23.622 -19.820
52 RPP -20.32 20.32 0.0 25.147 -26.162 -19.820
53 RPP -20.32 20.32 25.146 27.686 -26.162 -11.67
54 RPP -20.32 20.32 25.146 44.196 -11.67 -7.873
55 RPP -20.32 20.32 40.386 44.196 -7.87 14.224
56 RPP -7.62 7.62 33.34 46.040 14.225 19.68
57 RPP -3.81 3.81 -7.112 -4.572 11.174 13.714
58 RPP -3.81 3.81 5.08 22.86 11.174 13.714
59 RCC 0.0 0.0 11.174 0.0 0.0 2.54 12.7
60 RCC 0.0 0.0 11.174 0.0 0.0 2.54 15.24
61 RCC 0.0 0.0 16.510 0.0 0.0 1.90 11.43
62 RCC 0.0 0.0 16.510 0.0 0.0 1.90 20.955
63 RCC 0.0 0.0 18.414 0.0 0.0 3.81 10.16
64 RCC 0.0 0.0 18.414 0.0 0.0 3.81 20.955
65 RCC 0.0 0.0 22.230 0.0 0.0 5.075 7.62
66 RCC 0.0 0.0 22.230 0.0 0.0 5.075 20.955
67 1 RPP -9.398 9.398 -11.938 0 28.067 35.867
68 2 RPP -9.398 9.398 0 11.938 28.067 35.867
69 3 RPP -11.938 0 -10.795 10.795 36.703 44.503
70 4 RPP 0 11.938 -10.795 10.795 36.703 44.503
71 RCC 0.0 0.0 19.68 0.0 0.0 7.625 28.26
72 RCC 0.0 0.0 19.68 0.0 0.0 7.625 33.34
73 RCC 0.0 0.0 27.31 0.0 0.0 6.35 28.26
74 RCC 0.0 0.0 27.31 0.0 0.0 6.35 29.53
75 RCC 0.0 0.0 14.0 0.0 0.0 5.68 21.5
76 RCC 0.0 0.0 14.0 0.0 0.0 5.68 25.945
77 RPP -24.394 -20.33 -25.654 32.38 -12.7 8.89
78 RPP 20.33 24.394 -25.654 32.38 -12.7 8.89
79 RPP -10.15 -4.445 -4.06 8.65 -2.54 10.638
80 RPP 4.445 10.15 -4.06 8.65 -2.54 10.638
81 RCC -0.3 8.65 -2.54 0.6 0.0 0.0 8.43
82 RCC -0.3 8.65 -2.54 0.6 0.0 0.0 9.03
83 RCC 0.0 -50.0 6.19 0.0 40.0 0.0 0.5
84 RCC 0.0 -50.0 6.19 0.0 40.0 0.0 1.0
```

```
89 RPP -24.40 24.40 28.26 33.33 14.225 19.68
90 RPP -29.49 -24.41 -25.654 44.20 6.985 14.0
91 RPP 24.41 29.49 -25.654 44.20 6.985 14.0
92 RPP -28.175 -25.0 -13.97 13.97 35.0 43.16
93 RPP 25.0 28.175 -13.97 13.97 35.0 43.16
$ 92 RPP -28.175 -25.0 -13.97 13.97 35.0 45.16
$ 93 RPP 25.0 28.175 -13.97 13.97 35.0 45.16
$ 94 RCC 0.0 0.0 45.320 0.0 0.0 1.905 22.860 $45.72
$ 95 RCC 0.0 0.0 45.320 0.0 0.0 1.905 60.960
94 CZ 22.86
95 CZ 60.96
96 PZ 43.32 $ originally 45.32
97 PZ 45.225 $ originally 47.225
$ 98 RPP -75 75
11 SO 1000.0
```

```
$ mlc_7_g_08_PHITS-field1.cel
$ MLC Cell Cards
3099 0  ((231 -234 237 -238 240 -236):
        (231 -234 237 -238 235 -209):(232 -234 237 -238 209 -240))
        #301 #302 #303 #304 #305 #306 #307 #308 #309 #310
        #311 #312 #313 #314 #315 #316 #317 #318 #319 #320
    #381 #382 #383 #384 #385 #386 #387 #383 #389 #390 #391
3100 0 ((-231 233 237 -238 235 -209) : (-232 233 237 -238 209 -240) :
       (-231 233 237 -238 240 -236))
       #321 #322 #323 #324 #325 #326 #327 #328 #329 #330
       #331 #332 #333 #334 #335 #336 #337 #338 #339 #340
     #395 #396 #397 #398 #399 #400 #401 #402 #403 #404 #405
3101 0 ((231 -234 -237 239 235 -209) : (232 -234 -237 239 209 -240) :
       (231 -234 -237 239 240 -236))
       #341 #342 #343 #344 #345 #346 #347 #348 #349 #350
       #351 #352 #353 #354 #355 #356 #357 #358 #359 #360
     #409 #410 #411 #412 #413 #414 #415 #416 #417 #418 #419
3102 0  ((-231 233 -237 239 235 -209) : (-232 233 -237 239 209 -240) :
        (-231 233 -237 239 240 -236))
        #361 #362 #363 #364 #365 #366 #367 #368 #369 #370
        #371 #372 #373 #374 #375 #376 #377 #378 #379 #380
    #423 #424 #425 #426 #427 #428 #429 #430 #431 #432 #433
301 91 -18.0   ((-201 202 -218 -219 203 -204) : (205 206 -218 -220 204 -207):
               (208 206 -218 -220 207 -209) : (208 210 -218 -220 209 -211) :
               (208 206 -218 -220 211 -212) : (205 206 -218 -220 212 -213) :
               (-201 202 -218 -219 213 -214))
               *TRCL=(0 0 0 0 90 90 90 0.1427 90.1427 90 89.8573 0.1427)
302 LIKE 301 BUT *TRCL=(0 0 0 0 90 90 90 0.4281 90.4281 90 89.5719 0.4281)
303 LIKE 301 BUT *TRCL=(0 0 0 0 90 90 90 0.7135 90.7135 90 89.2865 0.7135)
304 LIKE 301 BUT *TRCL=(0 0 0 0 90 90 90 0.9989 90.9989 90 89.0011 0.9989)
305 LIKE 301 BUT *TRCL=(0 0 0 0 90 90 90 1.2843 91.2843 90 88.7157 1.2843)
306 LIKE 301 BUT *TRCL=(0 0 0 0 90 90 90 1.5697 91.5697 90 88.4303 1.5697)
307 LIKE 301 BUT *TRCL=(0 0 0 0 90 90 90 1.8551 91.8551 90 88.1449 1.8551)
308 LIKE 301 BUT *TRCL=(0 0 0 0 90 90 90 2.1405 92.1405 90 87.8595 2.1405)
309 LIKE 301 BUT *TRCL=(0 0 0 0 90 90 90 2.4259 92.4259 90 87.5741 2.4259)
310 LIKE 301 BUT *TRCL=(0 0 0 0 90 90 90 2.7113 92.7113 90 87.2887 2.7113)
311 LIKE 301 BUT *TRCL=(0 0 0 0 90 90 90 2.9967 92.9967 90 87.0033 2.9967)
312 LIKE 301 BUT *TRCL=(0 0 0 0 90 90 90 3.2821 93.2821 90 86.7179 3.2821)
313 LIKE 301 BUT *TRCL=(0 0 0 0 90 90 90 3.5675 93.5675 90 86.4325 3.5675)
314 LIKE 301 BUT *TRCL=(0 0 0 0 90 90 90 3.8529 93.8529 90 86.1471 3.8529)
```

```
315 LIKE 301 BUT *TRCL=(0 0 0 0 90 90 90 4.1383 94.1383 90 85.8617 4.1383)
316 LIKE 301 BUT *TRCL=(0 0 0 0 90 90 90 4.4237 94.4237 90 85.5763 4.4237)
317 LIKE 301 BUT *TRCL=(0 0 0 0 90 90 90 4.7091 94.7091 90 85.2909 4.7091)
318 LIKE 301 BUT *TRCL=(0 0 0 0 90 90 90 4.9945 94.9945 90 85.0055 4.9945)
319 LIKE 301 BUT *TRCL=(0 0 0 0 90 90 90 5.2799 95.2799 90 84.7201 5.2799)
320 LIKE 301 BUT *TRCL=(0 0 0 0 90 90 90 5.5653 95.5653 90 84.4347 5.5653)
381 91 -18.0   ((-241 242 -218 -219 203 -204) : (245 246 -218 -220 204 -207):
               (248 246 -218 -220 207 -209) : (248 250 -218 -220 209 -211) :
               (248 246 -218 -220 211 -212) : (245 246 -218 -220 212 -213) :
               (-241 242 -218 -219 213 -214))
               *TRCL=(0 0 0 0 90 90 90 5.9934 95.9934 90 84.0066 5.9934)
382 LIKE 381 BUT *TRCL=(0 0 0 0 90 90 90 6.5642 96.5642 90 83.4358 6.5642)
383 LIKE 381 BUT *TRCL=(0 0 0 0 90 90 90 7.1350 97.1350 90 82.8650 7.1350)
384 LIKE 381 BUT *TRCL=(0 0 0 0 90 90 90 7.7058 97.7058 90 82.2942 7.7058)
385 LIKE 381 BUT *TRCL=(0 0 0 0 90 90 90 8.2766 98.2766 90 81.7234 8.2766)
386 LIKE 381 BUT *TRCL=(0 0 0 0 90 90 90 8.8474 98.8474 90 81.1526 8.8474)
387 LIKE 381 BUT *TRCL=(0 0 0 0 90 90 90 9.4182  99.4182 90 80.5818 9.4182)
388 LIKE 381 BUT *TRCL=(0 0 0 0 90 90 90 9.9890  99.9890 90 80.0110 9.9890)
389 LIKE 381 BUT *TRCL=(0 0 0 0 90 90 90 10.5598 100.5598 90 79.4402 10.5598)
390 LIKE 381 BUT *TRCL=(0 0 0 0 90 90 90 11.1306 101.1306 90 78.8694 11.1306)
391 LIKE 381 BUT *TRCL=(0 0 0 0 90 90 90 11.7014 101.7014 90 78.2986 11.7014)
$
321 LIKE 301 BUT *TRCL=(0 0 0 0 90 90 90 0.1427 89.8573 90 90.1427 0.1427)
322 LIKE 301 BUT *TRCL=(0 0 0 0 90 90 90 0.4281 89.5719 90 90.4281 0.4281)
323 LIKE 301 BUT *TRCL=(0 0 0 0 90 90 90 0.7135 89.2865 90 90.7135 0.7135)
324 LIKE 301 BUT *TRCL=(0 0 0 0 90 90 90 0.9989 89.0011 90 90.9989 0.9989)
325 LIKE 301 BUT *TRCL=(0 0 0 0 90 90 90 1.2843 88.7157 90 91.2843 1.2843)
326 LIKE 301 BUT *TRCL=(0 0 0 0 90 90 90 1.5697 88.4303 90 91.5697 1.5697)
327 LIKE 301 BUT *TRCL=(0 0 0 0 90 90 90 1.8551 88.1449 90 91.8551 1.8551)
328 LIKE 301 BUT *TRCL=(0 0 0 0 90 90 90 2.1405 87.8595 90 92.1405 2.1405)
329 LIKE 301 BUT *TRCL=(0 0 0 0 90 90 90 2.4259 87.5741 90 92.4259 2.4259)
330 LIKE 301 BUT *TRCL=(0 0 0 0 90 90 90 2.7113 87.2887 90 92.7113 2.7113)
331 LIKE 301 BUT *TRCL=(0 0 0 0 90 90 90 2.9967 87.0033 90 92.9967 2.9967)
332 LIKE 301 BUT *TRCL=(0 0 0 0 90 90 90 3.2821 86.7179 90 93.2821 3.2821)
333 LIKE 301 BUT *TRCL=(0 0 0 0 90 90 90 3.5675 86.4325 90 93.5675 3.5675)
334 LIKE 301 BUT *TRCL=(0 0 0 0 90 90 90 3.8529 86.1471 90 93.8529 3.8529)
335 LIKE 301 BUT *TRCL=(0 0 0 0 90 90 90 4.1383 85.8617 90 94.1383 4.1383)
336 LIKE 301 BUT *TRCL=(0 0 0 0 90 90 90 4.4237 85.5763 90 94.4237 4.4237)
337 LIKE 301 BUT *TRCL=(0 0 0 0 90 90 90 4.7091 85.2909 90 94.7091 4.7091)
338 LIKE 301 BUT *TRCL=(0 0 0 0 90 90 90 4.9945 85.0055 90 94.9945 4.9945)
339 LIKE 301 BUT *TRCL=(0 0 0 0 90 90 90 5.2799 84.7201 90 95.2799 5.2799)
```

```
340 LIKE 301 BUT *TRCL=(0 0 0 0 90 90 90 5.5653 84.4347 90 95.5653 5.5653)
$
395 LIKE 381 BUT *TRCL=(0 0 0 0 90 90 90 5.9934 84.0066 90 95.9934 5.9934)
396 LIKE 381 BUT *TRCL=(0 0 0 0 90 90 90 6.5642 83.4358 90 96.5642 6.5642)
397 LIKE 381 BUT *TRCL=(0 0 0 0 90 90 90 7.1350 82.8650 90 97.1350 7.1350)
398 LIKE 381 BUT *TRCL=(0 0 0 0 90 90 90 7.7058 82.2942 90 97.7058 7.7058)
399 LIKE 381 BUT *TRCL=(0 0 0 0 90 90 90 8.2766 81.7234 90 98.2766 8.2766)
400 LIKE 381 BUT *TRCL=(0 0 0 0 90 90 90 8.8474 81.1526 90 98.8474 8.8474)
401 LIKE 381 BUT *TRCL=(0 0 0 0 90 90 90 9.4182 80.5818 90 99.4182 9.4182)
402 LIKE 381 BUT *TRCL=(0 0 0 0 90 90 90 9.9890 80.0110 90 99.9890 9.9890)
403 LIKE 381 BUT *TRCL=(0 0 0 0 90 90 90 10.5598 79.4402 90 100.5598 10.5598)
404 LIKE 381 BUT *TRCL=(0 0 0 0 90 90 90 11.1306 78.8694 90 101.1306 11.1306)
405 LIKE 381 BUT *TRCL=(0 0 0 0 90 90 90 11.7014 78.2986 90 101.7014 11.7014)
$
341 91 -18.0  (-201 202 -222 223 203 -204) : (205 206 -222 224 204 -207):
              (208 206 -222 224 207 -209) : (208 210 -222 224 209 -211) :
              (208 206 -222 224 211 -212) : (205 206 -222 224 212 -213) :
              (-201 202 -222 223 213 -214)
              *TRCL=(0 0 0 0 90 90 90 0.1427 90.1427 90 89.8573 0.1427)
342 LIKE 341 BUT *TRCL=(0 0 0 0 90 90 90 0.4281 90.4281 90 89.5719 0.4281)
343 LIKE 341 BUT *TRCL=(0 0 0 0 90 90 90 0.7135 90.7135 90 89.2865 0.7135)
344 LIKE 341 BUT *TRCL=(0 0 0 0 90 90 90 0.9989 90.9989 90 89.0011 0.9989)
345 LIKE 341 BUT *TRCL=(0 0 0 0 90 90 90 1.2843 91.2843 90 88.7157 1.2843)
346 LIKE 341 BUT *TRCL=(0 0 0 0 90 90 90 1.5697 91.5697 90 88.4303 1.5697)
347 LIKE 341 BUT *TRCL=(0 0 0 0 90 90 90 1.8551 91.8551 90 88.1449 1.8551)
348 LIKE 341 BUT *TRCL=(0 0 0 0 90 90 90 2.1405 92.1405 90 87.8595 2.1405)
349 LIKE 341 BUT *TRCL=(0 0 0 0 90 90 90 2.4259 92.4259 90 87.5741 2.4259)
350 LIKE 341 BUT *TRCL=(0 0 0 0 90 90 90 2.7113 92.7113 90 87.2887 2.7113)
351 LIKE 341 BUT *TRCL=(0 0 0 0 90 90 90 2.9967 92.9967 90 87.0033 2.9967)
352 LIKE 341 BUT *TRCL=(0 0 0 0 90 90 90 3.2821 93.2821 90 86.7179 3.2821)
353 LIKE 341 BUT *TRCL=(0 0 0 0 90 90 90 3.5675 93.5675 90 86.4325 3.5675)
354 LIKE 341 BUT *TRCL=(0 0 0 0 90 90 90 3.8529 93.8529 90 86.1471 3.8529)
355 LIKE 341 BUT *TRCL=(0 0 0 0 90 90 90 4.1383 94.1383 90 85.8617 4.1383)
356 LIKE 341 BUT *TRCL=(0 0 0 0 90 90 90 4.4237 94.4237 90 85.5763 4.4237)
357 LIKE 341 BUT *TRCL=(0 0 0 0 90 90 90 4.7091 94.7091 90 85.2909 4.7091)
358 LIKE 341 BUT *TRCL=(0 0 0 0 90 90 90 4.9945 94.9945 90 85.0055 4.9945)
359 LIKE 341 BUT *TRCL=(0 0 0 0 90 90 90 5.2799 95.2799 90 84.7201 5.2799)
360 LIKE 341 BUT *TRCL=(0 0 0 0 90 90 90 5.5653 95.5653 90 84.4347 5.5653)
409 91 -18.0   (-241 242 -222 223 203 -204) : (245 246 -222 224 204 -207):
               (248 246 -222 224 207 -209) : (248 250 -222 224 209 -211) :
               (248 246 -222 224 211 -212) : (245 246 -222 224 212 -213) :
```

```
                (-241 242 -222 223 213 -214)
124             *TRCL=(0 0 0 0 90 90 90 5.9934 95.9934 90 84.0066 5.9934)
    410 LIKE 409 BUT *TRCL=(0 0 0 0 90 90 90 6.5642 96.5642 90 83.4358 6.5642)
    411 LIKE 409 BUT *TRCL=(0 0 0 0 90 90 90 7.1350 97.1350 90 82.8650 7.1350)
    412 LIKE 409 BUT *TRCL=(0 0 0 0 90 90 90 7.7058 97.7058 90 82.2942 7.7058)
    413 LIKE 409 BUT *TRCL=(0 0 0 0 90 90 90 8.2766 98.2766 90 81.7234 8.2766)
    414 LIKE 409 BUT *TRCL=(0 0 0 0 90 90 90 8.8474 98.8474 90 81.1526 8.8474)
    415 LIKE 409 BUT *TRCL=(0 0 0 0 90 90 90 9.4182 99.4182 90 80.5818 9.4182)
    416 LIKE 409 BUT *TRCL=(0 0 0 0 90 90 90 9.9890 99.9890 90 80.0110 9.9890)
    417 LIKE 409 BUT *TRCL=(0 0 0 0 90 90 90 10.5598 100.5598 90 79.4402 10.5598)
    418 LIKE 409 BUT *TRCL=(0 0 0 0 90 90 90 11.1306 101.1306 90 78.8694 11.1306)
134 419 LIKE 409 BUT *TRCL=(0 0 0 0 90 90 90 11.7014 101.7014 90 78.2986 11.7014)
    $
    361 LIKE 341 BUT *TRCL=(0 0 0 0 90 90 90 0.1427 89.8573 90 90.1427 0.1427)
    362 LIKE 341 BUT *TRCL=(0 0 0 0 90 90 90 0.4281 89.5719 90 90.4281 0.4281)
    363 LIKE 341 BUT *TRCL=(0 0 0 0 90 90 90 0.7135 89.2865 90 90.7135 0.7135)
    364 LIKE 341 BUT *TRCL=(0 0 0 0 90 90 90 0.9989 89.0011 90 90.9989 0.9989)
    365 LIKE 341 BUT *TRCL=(0 0 0 0 90 90 90 1.2843 88.7157 90 91.2843 1.2843)
    366 LIKE 341 BUT *TRCL=(0 0 0 0 90 90 90 1.5697 88.4303 90 91.5697 1.5697)
    367 LIKE 341 BUT *TRCL=(0 0 0 0 90 90 90 1.8551 88.1449 90 91.8551 1.8551)
    368 LIKE 341 BUT *TRCL=(0 0 0 0 90 90 90 2.1405 87.8595 90 92.1405 2.1405)
144 369 LIKE 341 BUT *TRCL=(0 0 0 0 90 90 90 2.4259 87.5741 90 92.4259 2.4259)
    370 LIKE 341 BUT *TRCL=(0 0 0 0 90 90 90 2.7113 87.2887 90 92.7113 2.7113)
    371 LIKE 341 BUT *TRCL=(0 0 0 0 90 90 90 2.9967 87.0033 90 92.9967 2.9967)
    372 LIKE 341 BUT *TRCL=(0 0 0 0 90 90 90 3.2821 86.7179 90 93.2821 3.2821)
    373 LIKE 341 BUT *TRCL=(0 0 0 0 90 90 90 3.5675 86.4325 90 93.5675 3.5675)
    374 LIKE 341 BUT *TRCL=(0 0 0 0 90 90 90 3.8529 86.1471 90 93.8529 3.8529)
    375 LIKE 341 BUT *TRCL=(0 0 0 0 90 90 90 4.1383 85.8617 90 94.1383 4.1383)
    376 LIKE 341 BUT *TRCL=(0 0 0 0 90 90 90 4.4237 85.5763 90 94.4237 4.4237)
    377 LIKE 341 BUT *TRCL=(0 0 0 0 90 90 90 4.7091 85.2909 90 94.7091 4.7091)
    378 LIKE 341 BUT *TRCL=(0 0 0 0 90 90 90 4.9945 85.0055 90 94.9945 4.9945)
154 379 LIKE 341 BUT *TRCL=(0 0 0 0 90 90 90 5.2799 84.7201 90 95.2799 5.2799)
    380 LIKE 341 BUT *TRCL=(0 0 0 0 90 90 90 5.5653 84.4347 90 95.5653 5.5653)
    $
    423 LIKE 409 BUT *TRCL=(0 0 0 0 90 90 90 5.9934 84.0066 90 95.9934 5.9934)
    424 LIKE 409 BUT *TRCL=(0 0 0 0 90 90 90 6.5642 83.4358 90 96.5642 6.5642)
    425 LIKE 409 BUT *TRCL=(0 0 0 0 90 90 90 7.1350 82.8650 90 97.1350 7.1350)
    426 LIKE 409 BUT *TRCL=(0 0 0 0 90 90 90 7.7058 82.2942 90 97.7058 7.7058)
    427 LIKE 409 BUT *TRCL=(0 0 0 0 90 90 90 8.2766 81.7234 90 98.2766 8.2766)
    428 LIKE 409 BUT *TRCL=(0 0 0 0 90 90 90 8.8474 81.1526 90 98.8474 8.8474)
    429 LIKE 409 BUT *TRCL=(0 0 0 0 90 90 90 9.4182 80.5818 90 99.4182 9.4182)
```

```
164 430 LIKE 409 BUT *TRCL=(0 0 0 0 90 90 90 9.9890 80.0110 90 99.9890 9.9890)
    431 LIKE 409 BUT *TRCL=(0 0 0 0 90 90 90 10.5598 79.4402 90 100.5598 10.5598)
    432 LIKE 409 BUT *TRCL=(0 0 0 0 90 90 90 11.1306 78.8694 90 101.1306 11.1306)
    433 LIKE 409 BUT *TRCL=(0 0 0 0 90 90 90 11.7014 78.2986 90 101.7014 11.7014)
```

```
$ varain_clin_6_PHITS-ATP.cel
$ CELL CARDS FOR 6 MV ACCELERATOR MODEL
$ SURFACE CARDS
$ 82 total cells define the Clinac and surrounding vacuum
$ Vacuum Definition
1001 0   -12 17 18 21 22 27 31 32 35 40 41 42 43 44 45 46
        47 48 49 50 51 52 53 54 55 56 58 60 89 67 68 69
        70 72 74 76 77 78 84 90 91 92 93
        #1009 #1010 #1020 #194
1002 0 -59 27 29 57 58
1003 0 -24
196 0 -26 19
1004 0 -19 15 24
1005 0 -73 67 68
1006 0 -75 62 64
1007 0 -23 24
1008 0 -16 13 14
1009 0 -79 39 #145
1010 0 -80 #146 #1020
1011 0 -82 81 21 17
1012 0 -71 66 64
1016 0 -83
1017 0 -61
1018 0 -63
1019 0 -65 #188 #189
1020 0 -39
$ Target
1022 91 -18.0 -13 $density was 19.3 20
1023 92 -8.96 -14 13
1024 92 -8.96 -15 16
$ Primary Collimator
1025 91 -18.0 -20 26 19 24
1026 91 -18.0 -25 23 24
$ Other
1027 93 -7.87 -17 20 19 24
1028 93 -7.87 -18 19
1029 93 -7.87 -22 23
$ Other
1030 92 -8.96 -21 23 25
1031 92 -8.96 -84 83
```

```
$ Flattening Filter
$ 132 4 -16.65 -28
1033 92 -8.96 -27
1034 92 -8.96 -29
$ 135 3 -7.87 -30
$ Other
1036 93 -7.87 -35 34 17 21 39 79 80
1037 93 -7.87 -36 -34 33 -81
1038 93 -7.87 -36 -34 33 82
1039 93 -7.87 -37 -34 33 -81
1040 93 -7.87 -37 -34 33 82
1041 93 -7.87 -38 -34 33 -81
1042 93 -7.87 -38 -34 33 82
$ Other
143 91 -18.0 -34 33 36 37 38 39 17 21 -81
144 91 -18.0 -34 33 36 37 38 39 17 21 82 $40
145 91 -18.0 -31
146 91 -18.0 -32
$ Other
147 95 -11.4 -33 17
148 95 -11.4 -44
$ Other
149 93 -7.87 -40
150 93 -7.87 -41
151 93 -7.87 -42
152 93 -7.87 -43
153 93 -7.87 -45
154 93 -7.87 -46
155 93 -7.87 -47
156 93 -7.87 -48
157 93 -7.87 -49
158 93 -7.87 -50
$ Other
159 95 -11.4 -51
160 95 -11.4 -52
161 95 -11.4 -53 #160
162 95 -11.4 -54
163 95 -11.4 -77
164 95 -11.4 -78 $60
$ Other
165 95 -11.4 -56
```

```
166 95 -11.4 -57
176 95 -11.4 -58 #177
177 95 -11.4 -60 59
$ Other
178 91 -18.0 -62 61
179 91 -18.0 -64 63
180 91 -18.0 -55
$ Other
181 93 -7.87 -76 75
182 93 -7.87 -90
183 93 -7.87 -91
$ Other
184 95 -11.4 -66 65 #188 #189
185 95 -11.4 -72 71
186 95 -11.4 -74 73
187 95 -11.4 -89
$ Other
188 91 -18.0 -67
189 91 -18.0 -68
190 91 -18.0 -69
191 91 -18.0 -70
$ Other
192 93 -7.87 -92
193 93 -7.87 -93 $80
194 93 -7.87 -95 94 96 -97
195 97 -0.0012 -11 12 (-233:236:234:-235:238:-239) #1 #703 #731 #732 #733 #734 #735 #736
    #737 #738 #739 #740
$195 97 -0.0012 -11 12 411 412 (-233:236:234:-235:238:-239)
```

```
$ TLDandbolus.cell
600  3 -1.00 -601
601  1 -2.48 -600
602  2 -0.93 -602 #601 #603 #604 #605 #606 #607 #608 #609 #610
  #611 #612 #613 #614 #615 #616 #617 #618 #619 #620 #621 #622
  #623 #624 #625 #626 #627 #628 #629 #630 #631 #632 #633 #634
  #635 #636 #637 #638 #639 #640 #641
603 LIKE 601 BUT *TRCL=(-1.42 0 0 0 0 0 0 0 0 0 0 0 2)
604 LIKE 601 BUT *TRCL=(-2.84 0 0 0 0 0 0 0 0 0 0 0 2)
605 LIKE 601 BUT *TRCL=(1.42 0 0 0 0 0 0 0 0 0 0 0 2)
606 LIKE 601 BUT *TRCL=(2.84 0 0 0 0 0 0 0 0 0 0 0 2)
607 LIKE 601 BUT *TRCL=(4.26 0 0 0 0 0 0 0 0 0 0 0 2)
608 LIKE 601 BUT *TRCL=(0 1.25 0 0 0 0 0 0 0 0 0 0 2)
609 LIKE 601 BUT *TRCL=(0 2.50 0 0 0 0 0 0 0 0 0 0 2)
610 LIKE 601 BUT *TRCL=(0 3.75 0 0 0 0 0 0 0 0 0 0 2)
611 LIKE 601 BUT *TRCL=(0 -1.25 0 0 0 0 0 0 0 0 0 0 2)
612 LIKE 601 BUT *TRCL=(0 -2.50 0 0 0 0 0 0 0 0 0 0 2)
613 LIKE 601 BUT *TRCL=(0 -3.75 0 0 0 0 0 0 0 0 0 0 2)
614 LIKE 601 BUT *TRCL=(-1.42 1.25 0 0 0 0 0 0 0 0 0 0 2)
615 LIKE 601 BUT *TRCL=(-1.42 2.50 0 0 0 0 0 0 0 0 0 0 2)
616 LIKE 601 BUT *TRCL=(-1.42 3.75 0 0 0 0 0 0 0 0 0 0 2)
617 LIKE 601 BUT *TRCL=(-1.42 -1.25 0 0 0 0 0 0 0 0 0 0 2)
618 LIKE 601 BUT *TRCL=(-1.42 -2.50 0 0 0 0 0 0 0 0 0 0 2)
619 LIKE 601 BUT *TRCL=(-1.42 -3.75 0 0 0 0 0 0 0 0 0 0 2)
620 LIKE 601 BUT *TRCL=(1.42 1.25 0 0 0 0 0 0 0 0 0 0 2)
621 LIKE 601 BUT *TRCL=(1.42 2.50 0 0 0 0 0 0 0 0 0 0 2)
622 LIKE 601 BUT *TRCL=(1.42 3.75 0 0 0 0 0 0 0 0 0 0 2)
623 LIKE 601 BUT *TRCL=(1.42 -1.25 0 0 0 0 0 0 0 0 0 0 2)
624 LIKE 601 BUT *TRCL=(1.42 -2.50 0 0 0 0 0 0 0 0 0 0 2)
625 LIKE 601 BUT *TRCL=(1.42 -3.75 0 0 0 0 0 0 0 0 0 0 2)
626 LIKE 601 BUT *TRCL=(-2.84 1.25 0 0 0 0 0 0 0 0 0 0 2)
627 LIKE 601 BUT *TRCL=(-2.84 2.50 0 0 0 0 0 0 0 0 0 0 2)
628 LIKE 601 BUT *TRCL=(-2.84 3.75 0 0 0 0 0 0 0 0 0 0 2)
629 LIKE 601 BUT *TRCL=(-2.84 -1.25 0 0 0 0 0 0 0 0 0 0 2)
630 LIKE 601 BUT *TRCL=(-2.84 -2.50 0 0 0 0 0 0 0 0 0 0 2)
631 LIKE 601 BUT *TRCL=(2.84 1.25 0 0 0 0 0 0 0 0 0 0 2)
632 LIKE 601 BUT *TRCL=(2.84 2.50 0 0 0 0 0 0 0 0 0 0 2)
633 LIKE 601 BUT *TRCL=(2.84 3.75 0 0 0 0 0 0 0 0 0 0 2)
634 LIKE 601 BUT *TRCL=(2.84 -1.25 0 0 0 0 0 0 0 0 0 0 2)
635 LIKE 601 BUT *TRCL=(2.84 -2.50 0 0 0 0 0 0 0 0 0 0 2)
```

```
636 LIKE 601 BUT *TRCL=(2.84 -3.75 0 0 0 0 0 0 0 0 0 0 2)
637 LIKE 601 BUT *TRCL=(4.26 1.25 0 0 0 0 0 0 0 0 0 0 2)
638 LIKE 601 BUT *TRCL=(4.26 2.50 0 0 0 0 0 0 0 0 0 0 2)
639 LIKE 601 BUT *TRCL=(4.26 3.75 0 0 0 0 0 0 0 0 0 0 2)
640 LIKE 601 BUT *TRCL=(4.26 -1.25 0 0 0 0 0 0 0 0 0 0 2)
641 LIKE 601 BUT *TRCL=(4.26 -2.50 0 0 0 0 0 0 0 0 0 0 2)
642 4 -0.4 -603
```

```
$ATP-VOL
reg   vol
701   1145
702   1007
703   6.370626303
704   208
705   1410
706   75
707   139
708   13611
710   0.0091136
711   0.0091136
712   0.0091136
713   0.0091136
714   0.0091136
715   0.0091136
716   0.0091136
717   0.0091136
718   0.0091136
719   0.0091136
720   0.0091136
721   0.0091136
722   0.0091136
723   0.0091136
724   0.0091136
725   0.0091136
726   0.0091136
727   0.0091136
728   0.0091136
729   0.0091136
730   0.0091136
731   0.0091136
732   0.0091136
733   0.0091136
734   0.0091136
735   0.0091136
736   0.0091136
737   0.0091136
738   0.0091136
739   0.0091136
```

```
740    0.0091136
```